

HI JENA

Helmholtz Institute Jena

ANNUAL REPORT 2023



FRIEDRICH-SCHILLER-
UNIVERSITÄT
JENA

HZDR
HELMHOLTZ ZENTRUM
DRESDEN ROSSENDORF



HELMHOLTZ INSTITUTE JENA

ANNUAL REPORT 2023

IMPRINT

Publisher: Helmholtz-Institut Jena, Fröbelstieg 3, 07743 Jena, Germany
(<http://www.hi-jena.de>)
@ GSI Helmholtzzentrum für Schwerionenforschung GmbH
Darmstadt, Germany (<http://www.gsi.de>)
GSI is member of the Helmholtz association of national research
centers (<http://www.helmholtz.de>).

Editors: Daniel Seipt and Arno Klenke

DOI: <http://dx.doi.org/10.15120/GSI-2024-00679>

Publication date: August 2024

The Annual Report 2023 of the Helmholtz-Institut Jena is licensed under the Creative Commons Attribution BY 4.0 (CC BY 4.0): <https://creativecommons.org/licenses/by/4.0/>

CONTENTS

FOREWORD	10
Public Outreach and Early Career Support for Young Scientists <i>R. Märtin, C. Hahn, and G. Weber</i>	12
Outreach via Stratosphere <i>V. Tympel and I. Kadner</i>	13
HIGH POWER LASER DEVELOPMENT	14
Description of optical design software LaserCAD <i>C. Anschutz, J. Hein, H. Zhuang, and M. Kaluza</i>	15
Design of a stretcher-compressor-pair for a 2400 nm CPA system <i>C. Anschutz, Z. Zhang, J. Hein, and M. Kaluza</i>	16
Update on the Active Stretcher System for the POLARIS Upgrade <i>G. A. Becker, M. Hornung, M. Hellwing, F. Schorcht, and M. C. Kaluza</i>	17
POLARIS Pulse Compressor and Beam Transport Upgrade <i>M. Hornung, M. Ostermann, M. Hellwing, F. Schorcht, and M. C. Kaluza</i>	18
Beam Transport from POLARIS and JETi200 to the new Target Area Fraunhofer (TAF) <i>M. Hornung, M. Ostermann, T. Köhler, A. Sävert, M. Zepf, and M. C. Kaluza</i>	19
Vibration Measurements and Improvement of the TAF Beam Transport System <i>M. Hornung, R. Berg-Jahnke, D. Heiland, T. Köhler, and M. C. Kaluza</i>	20
Status of the Tango Control system at JETi200 <i>D. Hollatz, A. Sävert, P. Hilz, and M. Zepf</i>	21

Dependence of transverse mode instability threshold on the modal content of the seed light in fiber amplifiers <i>Y. Tu, C. Jauregui, and J. Limpert</i>	22
High power laser sources based on a 49-core Ytterbium doped fiber <i>A. Klenke, M. Bahri, C. Jauregui, J. Nold, S. Haarlammert, T. Schreiber, and J. Limpert</i>	23
Intensity Tagging for Ultrashort High-Power Laser <i>X. Huang, A. Sävert, and M. Zepf</i>	24
Compact, folded multi-pass cell for energy scaling of post-compression <i>A. Schönberg and C. M. Heyl</i>	25
More than 100-fold pulse compression by hybrid multi-pass multi-plate spectral broadening <i>M. Seidel</i>	26
High-quality pulse compression in nonlinear multipass cells enabled by dispersion engineering <i>M. Karst, M. Benner, P. Gierschke, H. Stark, and J. Limpert</i>	27
Microscopic Ghost Imaging in the table top XUV <i>S. Oh, T. Tian, and C. Spielmann</i>	28
Enhanced Ghost Imaging with Fewer Measurements <i>T. Tian, S. Oh, and C. Spielmann</i>	29
Broadband ptychography using curved wavefront illumination <i>D. S. Penagos Molina, L. Loetgering, W. Eschen, J. Limpert, and J. Rothhardt</i>	30
Setup for the characterization of laser materials and first results <i>M. Beyer, M. Hellwing, M. Hornung, G. A. Becker, J. Hein, and M.C. Kaluza</i>	31
LASER PARTICLE ACCELERATION	32
Helmholtz Laser-Plasma Metadata Initiative (HELPMI) <i>A. Kessler, M. Schwab, M. Kaluza, H. P. Schlenvoigt, F. Pöschel, A. Debus, V. Bagnoud, U. Eisenbart, and J. Hornung</i>	33
Unified solid state-plasma kinetics modeling for ultrafast laser-solid interactions <i>Y. Azamoum, G. A. Becker, S. Keppler, G. Duchateau, S. Skupin, M. Grech, F. Catoire, S. Hell, I. Tamer, M. Hornung, M. Hellwing, A. Kessler, F. Schorcht, and M. C. Kaluza</i>	34

Development of ultrafast burst shot shadowgraphy for plasma diagnostics	
<i>Y. Zhao, X. Huang, A. Sävert, and M. C. Kaluza</i>	35
All-optical measurements of LWFA electron beam source size and emittance	
<i>F. C. Salgado, A. Kozan, D. Seipt, D. Hollatz, P. Hilz, M. Kaluza, A. Sävert, A. Seidel, D. Ullmann, Y. Zhao, and M. Zepf</i>	36
Preparations and target fabrication for investigating the peeler scheme at JETi200	
<i>I. Salaheldin, L. Reichwein, P. Hilz, and M. Zepf</i>	37
Limitations of Emittance Measurement Using Pepper Pot Method	
<i>A. Kozan, F. Salgado, D. Seipt, D. Hollatz, P. Hilz, M. Kaluza, A. Sävert, A. Seidel, D. Ullmann, Y. Zhao, and M. Zepf</i>	38
Enhanced Laser-Driven Electron and Ion Acceleration Using Near-Critical Density Plasma CNF Targets	
<i>P. Tavana, M. Gyrdymov, O.N. Rosmej, and C. Spielmann</i>	39
Nanosecond Lifetime Hot and Dense Plasmas from Relativistic Laser-Nanowire Interaction	
<i>E. Eftekhari-Zadeh, M. Gyrdymov, P. Tavana, R. Loetzsch, I. Uschmann, T. Siefke, T. Käsebier, U. Zeitner, A. Szeghalmi, D. Serebryakov, E. Nerush, I. Kostyukov, O. Rosmej, D. Kartashov, and C. Spielmann</i>	40
PHOTON AND PARTICLE SPECTROSCOPY	42
Enabling quantum technologies for the next level of precision	
<i>P. Micke</i>	43
A Binary Occulter Design for creating Ultra-High Contrast Shadow	
<i>H. Iyer, F. Salgado, D. Seipt, and M. Zepf</i>	44
Second CCC of Small and Smart Series	
<i>V. Tympel and F. Machalett</i>	45
Characterization and correction of ADC artefacts in spectral data obtained with microcalorimeter detectors	
<i>D. A. Müller, M. O. Herdrich, F. M. Kröger, B. Löher, Ph. Pfäfflein, G. Weber, and Th. Stöhlker</i>	46
Laser-driven high-flux XUV source for coincidence experiments	
<i>J. Späthe, S. Hell, B. Ying, M. Wünsche, R. Klas, J. Rothhardt, J. Limpert, G. G. Paulus, and M. Kübel</i>	47

Non-destructive depth reconstruction of Al-Al₂Cu layer structure with nanometer resolution using extreme ultraviolet coherence tomography <i>J. J. Abel, J. Apell, F. Wiesner, J. Reinhard, M. Wünsche, G. G. Paulus, S. Lippmann, and S. Fuchs</i>	48
Resonant X-ray excitation of the nuclear clock isomer ⁴⁵Sc <i>Yu. Shvyd'ko, R. Röhlberger, O. Kocharovskaya, and J. Evers</i>	49
Imaging via Correlation of X-Ray Fluorescence Photons <i>F. Trost, R. Röhlberger, H. Chapman, and J. von Zanthier</i>	50
Laboratory-based Correlative Fluorescence and Water-Window Microscopy <i>S. Kaleta, J. Reinhard, J. Abel, F. Wiesner, M. Wünsche, E. Seemann, C. Eggeling, S. Fuchs, and G. G. Paulus</i>	51
Polarization Phenomena of Compton Scattering in the Hard X-Ray Regime Revealed by Compton Polarimetry <i>T. Over, A. Gumberidze, M. O. Herdrich, T. Krings, W. Middents, Ph. Pfäfflein, U. Spillmann, G. Weber, and Th. Stöhlker</i>	52
Towards a three-dimensional reconstruction of Compton scattering events within a Compton polarimeter <i>H. El-Ammari, W. Middents, T. Over, G. Weber, and Th. Stöhlker</i>	53
First X-ray Spectroscopy Measurements with S-EBIT II <i>R. Simon, T. Morgenroth, and S. Bernitt</i>	54
High-Precision X-ray Spectroscopy for Astrophysics with PolarX-EBIT <i>S. Bernitt, C. Shah, M. Togawa, M. Botz, R. Steinbrügge, M. A. Leutenegger, and J. R. Crespo Lopez-Urrutia</i>	55
Background measurements of the Darkfield technique for Quantum Vacuum Birefringence at the European XFEL <i>P. Khademi, A. Sävert, W. Hippler, R. Löttsch, G. G. Paulus, and M. Zepf</i>	56
Progress Report of the Negative Ions Laser Photodetachment Project <i>O. Forstner, S. Prasad Pulipati, and K. Wendt</i>	57
Fast ion cooling and ion cloud preparation with the HILITE Penning trap <i>S. Ringleb, M. Kiffer, M. Vogel, and Th. Stöhlker</i>	58

First experimental determination of the branching ratio of an intra-shell transition in a He-like heavy ion system	
<i>F. M. Kröger, S. Allgeier, Z. Andelkovic, S. Bernitt, A. Borovik, L. Duval, A. Fleischmann, O. Forstner, M. Friedrich, J. Glorius, A. Gumberidze, Ch. Hahn, F. Herfurth, D. Hengstler, M. O. Herdrich, P.-M. Hillenbrand, A. Kalinin, M. Kiffer, T. Köhler, M. Kubullek, P. Kuntz, M. Lestinsky, B. Löher, E.B. Menz, T. Over, N. Petridis, Ph. Pfäfflein, S. Ringleb, R. S. Sidhu, U. Spillmann, S. Trotsenko, A. Warczak, G. Weber, B. Zhu, C. Enss, and Th. Stöhlker</i>	59
Low-energy Dielectronic Recombination of Ne³⁺ Measured at CRYRING@ESR	
<i>E. B. Menz, E.-O. Hanu, M. Lestinsky, M. Looshorn, W. Biela-Nowaczyk, C. Brandau, M. Fogle, P.-M. Hillenbrand, R. Schuch, K. Ueberholz, G. Vorobyev, S. Wang, A. Warczak, S. Schippers, and Th. Stöhlker</i>	60
High brightness ion sources for strong-field laser and other applications	
<i>F. Machalett, B. Ying, A. Sommerfeld, S. Lippmann, Th. Stöhlker, and G. G. Paulus</i>	61
THEORY	62
Two-beam laser photon merging	
<i>C. Sundqvist and F. Karbstein</i>	63
Bayesian optimization of quantum vacuum signals	
<i>M. A. Valialshchikov, F. Karbstein, D. Seipt, and M. Zepf</i>	64
Exploring new states of matter with a photonic emulator	
<i>F. Karbstein, S. Stützer, H. Gies, and A. Szameit</i>	65
Laser Resonance Chromatography of ²²⁹Th³⁺ in He: an ab initio investigation	
<i>G. Visentin, A. Borschevsky, L. A. Viehland, S. Fritzsche, and M. Laatiaoui</i>	66
Comparison of theory and experiment for radiative characteristics in Tm I	
<i>A. Bondarev, M. Tamanis, R. Ferber, G. Başar, S. Kröger, M. Kozlov, and S. Fritzsche</i>	67
Coulomb excitation of hydrogen atoms by vortex ion beams	
<i>A. V. Maiorova, D. Karlovets, S. Fritzsche, A. Surzhykov, and Th. Stöhlker</i>	68
Tracing the effects of fundamental frequencies in laser pulses on electron momentum and ionization	
<i>D. F. Dar and S. Fritzsche</i>	69
Partial-wave representation of the strong-field approximation — length versus velocity gauge	
<i>F. Liu, S. Fritzsche, and M. Kübel</i>	70

Comparison between velocity and length gauge in strong-field approximation under partial-wave representation <i>K. Zou , F. Liu, and S. Fritzsche</i>	71
Towards enhanced efficiency of spontaneous parametric down-conversion with varying focal planes of interacting beams <i>R. Bernecker, B. Baghdasaryan, and S. Fritzsche</i>	72
Interaction of Hermite-Gaussian modes with a macroscopic atomic target <i>S. Ramakrishna, Z. W. Wu, A. V. Maiorova, and S. Fritzsche</i>	73
Quantum electrodynamics of relativistic Luttinger fermions <i>H. Gies and M. Picciao</i>	74
3D simulations of angular deflection as novel signatures of radiation reaction in electron-beam laser sidescattering <i>P. Sikorski, A. G. R. Thomas, S. S. Bulanov, M. Zepf, and D. Seipt</i>	75
Phase space structure of nonlinear Compton scattering <i>N. Larin and D. Seipt</i>	76
Laser polarization control of ionization-injected electron beams and x-ray radiation in LWFA <i>A. Mukherjee and D. Seipt</i>	77
PUBLICATIONS	78
THESES	92

FOREWORD

Dear friends and members of the Helmholtz Institute Jena,

Time is running fast! Fifteen years ago, the Helmholtz Institute Jena (HI-Jena) was founded as an institute of GSI Darmstadt on the campus of the Friedrich Schiller University Jena, with the University and the Helmholtz centers DESY and HZDR as additional partners. It combines established scientific expertise of the university and the other partners with the strategic mission of GSI. The Institute's mission is excellence in fundamental and applied research based on high-power lasers, particle accelerators, and x-ray science. In the pursuit of this, it addresses the coupling of intense light with matter, and conducts various research and development efforts of advanced instrumentation for dedicated experiments at the flagship facilities for extreme matter research, the EU-XFEL in Hamburg and the international FAIR project in Darmstadt.

Being hosted at the campus of the Friedrich Schiller University, the close contact of HI-Jena with the research groups from the university helped establish the high-power laser systems POLARIS and JETi200 and also specialized detector, x-ray and cryo-laboratories, bolstering the Institute's active involvement in the strategic missions of GSI. During the reporting period, particular emphasis was given to the FAIR phase-0 activities at GSI, experiments related to vacuum birefringence at European XFEL as well as to experiments at the laser facilities at HI-Jena's own high-power laser facilities.

Key to the success of the Institute are the young researchers, postdocs and PhD students, who are actively engaged in research and the close cooperation with our partners, in particular the colleagues from the University of Jena. In this context, it should be emphasized that for the accomplishments in research the young scientists were again honored with prizes and awards. In November 2023, HI-Jena scientist Dr. Jan Rothhardt received the Beutenberg-Campus Jena e. V. science prize together with a team from the University of Jena, Fraunhofer IOF and the Leibniz Institute for Natural Product Research and Infection Biology – Hans Knöll Institute (HKI). The researchers have developed a novel microscopy method that provides insights into the nanoworld of microorganisms in the extreme ultraviolet light spectrum. Furthermore, two PhD candidates from Helmholtz Institute Jena, Wilhelm Eschen and Chang Liu, were awarded the 2023 Siegfried Czapski Publication Prize for outstanding publications within the Jena Alliance of Graduate Schools. The two doctoral students received the prize for their publication in the journal *PhotoniX* on visualizing the ultra-structure of microorganisms using table-top extreme ultraviolet imaging. Moreover, Prof. Dr. Thomas Stöhlker received an ERC Advanced Grant from the European Research Council (ERC). His project HITHOR (Highly Ionized Trapped 229-Thorium: A New Paradigm Towards a Nuclear Clock) has been awarded the European Union's research funding prize for established scientists. HITHOR experiments will be performed at GSI's ion storage ring and trapping facilities (ESR and HITRAP) where highly ionized 229-thorium can be synthesized, decelerated, trapped and cooled and precisely studied. This project profits considerably from the ongoing developments at the Institute related to high-power UV lasers.

Education and promotion of the next generation of young scientists is a particular focus of activities of the Institute. The Research School of Advanced Photon Science of the Helmholtz Institute Jena, closely cooperating with the Helmholtz Graduate School for Hadron and Ion Research, is a

well-established institution that provides next-generation scientists with supervision, education, and support during their doctoral phase. The number of participants remains stable at between 50 and 60, with half the students directly financially supported by the Helmholtz Institute Jena and the other half third-party funded. The Research School exhibits a pronounced international visibility, with about 60 % PhD candidates from abroad.

The promotion of excellent young scientists at the Institute also includes the establishment and support of young investigator groups. Currently three young investigator groups are active at the Institute. In 2023, Dr. Peter Micke started his Helmholtz Young Investigator Group on “Quantum logic spectroscopy for frequency metrology of heavy and simple ions”. In 2024, he was appointed junior professor for “Laser spectroscopy in ion traps” at the University of Jena.

The Institute is increasing its outreach activities to high school students to promote science and the work as a researcher as future profession. In 2023, the Institute joined as a new site partner the BMBF funded “Netzwerk Teilchenwelt” which organized, from November 6th to 12th, the “Week of the Particle World” throughout Germany. The Helmholtz Institute Jena took part as a new site partner of the network with a public hybrid lecture on nuclear astrophysics and a small exhibition in the foyer of the new institute building.

As already reported in the last annual reports, the Helmholtz Institute is facing challenges with regard to its running budget due to inflation and the general rise in costs. The acquisition of third-party funding is therefore of crucial importance and receives special attention. As such, the HI-Jena co-creation project “Innovation partnership for highly volatile EUV beam sources for applications in metrology and imaging (InnoEUV)” was successfully acquired with a funding of 915,000 EUR as part of the Helmholtz Association’s IVF. Within this project, the Institute is investigating a new approach in generating coherent laser-like EUV radiation at a wavelength of 13.5 nm with revolutionary characteristics in co-creative collaboration with Active Fiber Systems GmbH and potential end users. Moreover, in a new cooperation between the Helmholtz Institute Jena and the Friedrich Schiller University Jena, a research group is investigating novel imaging methods in the short-wave XUV spectral range. The project will initially run for three years and is being funded by the Free State of Thuringia and the European Social Fund Plus of the European Union with a total of around 900,000 EUR, split equally between the partners. Also, the Free State of Thuringia is supporting the research infrastructure in the new research building of the Helmholtz Institute Jena with a series of projects co-funded by the European Union as part of the European Regional Development Fund (ERDF), promoting novel research infrastructure for high-power laser systems of the future. There, the University of Jena and the Helmholtz Institute Jena jointly endeavor to achieve new peak power levels and intensities at the POLARIS and JETi200 laser systems (2023 FGI 0023 “Infrastructure to increase the peak intensity of the high-power laser systems at HI Jena”). At the same time, the pulses can be flexibly shaped using a new type of AI-compatible control system (2023 FGI 0022 “Artificial intelligence for high-power lasers at the Helmholtz Institute Jena” and 2022 FGI 0005 “Laser beam shaping unit for the Helmholtz Institute Jena”) and synchronized at a femtosecond level (2022 FGI 0008 “Femtosecond synchronization of high-power lasers”). This will open up completely new experimental possibilities for the Institute and further expand research into laser-based particle and secondary radiation sources at a world-class level.

This annual report presents the scientific activities and successes of 2023. Enjoy reading.

Public Outreach and Early Career Support for Young Scientists

R. Märtin*¹, C. Hahn¹, and G. Weber¹

¹HI Jena, Fröbelstieg 3, 07743 Jena, Germany

One of the main missions of the Helmholtz Institute Jena is the recruitment, education, and support of early career scientists. Efforts already start on the high school level to counteract the shortage of qualified employees in the natural sciences. Moreover, the strengthening of science communication to politics and the general public is one possibility to facilitate technology transfer and to bring research results into application

The promotion of young researchers during their doctorate is organized through the already well-established Research School of Advanced Photon Science (RS-APS). The outreach program at the institute will be further expanded, amongst others, by joining the national BMBF initiative “Netzwerk Teilchenwelt” in 2023.



Figure 1: Group picture of Lecture Week participants.

During this reporting year 63 PhD students participated in the program of the research school of the Helmholtz Institute Jena. With more than 60% of foreign origin and 16% female students, the number of graduates per year participating in RS-APS reached its highest level to date with 12 successfully completed doctorates.

At the end of February 2023, the Research School of Advanced Photon Science hosted already its 10th edition of its “Joint RS-APS & HGS-HIRe Lecture Week”. With this the Research School is not only celebrating its “Lecture Week anniversary” but also returned for the first in-person event after the Corona pandemic. The event took place at the University of Jena and 17 students got to know the four different research areas of the APPA collaboration at FAIR.

Several students of RS-APS also achieved further academic successes. Two PhD candidates, Wilhelm Eschen

and Chang Liu, were awarded with the Siegfried Czap-ski Publication Prize for their outstanding publication in the journal *PhotoniX*. Robert Klas has received the “Hugo Geiger Award for Young Scientists” granted by the Free State of Bavaria and the Fraunhofer-Gesellschaft. Moreover, during the reporting year two members of the research school received poster prizes at international conferences, with Philip Pfäfflein being awarded a prize for his poster contribution at the International Conference on Photonic, Electronic and Atomic Collisions (ICPEAC 2023), and Marc Oliver Herdrich at the International Conference on Precision Physics and Fundamental Physical Constants (FFK 2023).

Targeting the outreach to the public and students on the high school level, the Helmholtz Institute Jena supported the MINT Festival 2023 in Jena, which aims to get students of all ages excited about mathematics, computer science, natural sciences, and technology. Scientists from HI Jena presented the work as a physicist with an exhibition booth at the speed dating session with high school students.

In 2023, scientists from HI Jena also tutored students who were interested in getting an active inside view into the research at the HI Jena, working for two weeks on a dedicated physics project in the context of a high-school student internship. Additionally senior scientists at the institute supported and supervised seminar theses which are mandatory for students on the senior high school level in Thuringia.

Since October 2023 HI Jena is an official site partner of the BMBF-funded collaboration “Netzwerk Teilchenwelt”. The institute launched its new membership with the participation in the “Woche der Teilchenwelt” which took place from November 6th to 12th throughout Germany. The Helmholtz Institute took part with a public hybrid lecture on nuclear astrophysics and a small exhibition in the foyer of the new institute building. In addition to information about the Helmholtz Institute itself and the collaboration network “Teilchenwelt”, visitors were able to gain a small insight into the physics of X-rays and radioactive radiation using a mechanical X-ray scattering model and a cloud chamber.

* r.märtin@hi-jena.gsi.de

Outreach via Stratosphere

V. Tympel^{*1,2} and I. Kadner³

¹HI Jena, Fröbelstieg 3, 07743 Jena, Germany; ²GSI, Planckstraße 1, Darmstadt; ³NaWi School Verein Naturwissenschaftliche Bildung e.V., Feldstr. 12b, 16341 Panketal

The flight of a stratospheric balloon is an exciting undertaking and suitable to arouse an interest in the STEM (science, technology, engineering, and mathematics) subjects among high school students. The Regener-Pfotzer maximum (extremum of secondary cosmic rays) at an altitude of about 20 km is a worthwhile target that can be easily measured with Geiger-Müller counters (GMCs).

In cooperation with the NaWi School, a student soldering kit (Fig. 1 (left)) for an airworthy Geiger-Müller counter (GMC) was developed. The GMC is based on an Arduino Nano and implements a regulated and student-safe 400 V power supply for the counter tube, pulse counting and data communication incl. daisy chaining. The communication takes place according to the XDATA protocol for meteorological measuring instruments, such as ozone probes. The data is then taken over by an original or a reprogrammed weather radiosonde and sent to the ground together with GPS positions. The U.S. National Oceanic and Atmospheric Administration (NOAA) has assigned the GCM its own identifier, so that decoding programs for radiosondes such as RS41Tracker (Fig. 2) can display the measured values live via a beamer.

A test of the soldering kit was carried out in 2021 by a student at the Max-Steenbeck Gymnasium in Cottbus. 13 steps with soldering and measuring tasks are necessary to complete the GMC (Fig. 1 (right)). The seminar work of Zuzanna Pacholska was successful and she received a Dr. Hans Riegel award for physics at the University of Potsdam in 2022.

A full system test was carried out at the AstroCamp of DESY and NaWi School in August 2023 at Werbellinsee north of Berlin. 20 selected high school students prepared and carried out a complex balloon mission under guidance. The radio connection was made in the 70-cm amateur radio band with the support of the German Amateur Radio Club local chapter Jena (DARC X-22). Thanks to the radio connection, the students were able to collect important data during the flight. As expected, the Regener-Pfotzer maximum could be detected at an altitude of about 20 km (Fig. 3).

With the increase in solar activity, a reduction in the amplitude of the Regener-Pfotzer maximum is expected for 2024 [1]. For the Day of Physics and Astronomy at the University of Jena, a balloon launch with several GMCs is planned. For the first time, all 6 possible instrument slots will be used in one mission.



Figure 1: Soldering kit (left) and finished GMC (right).

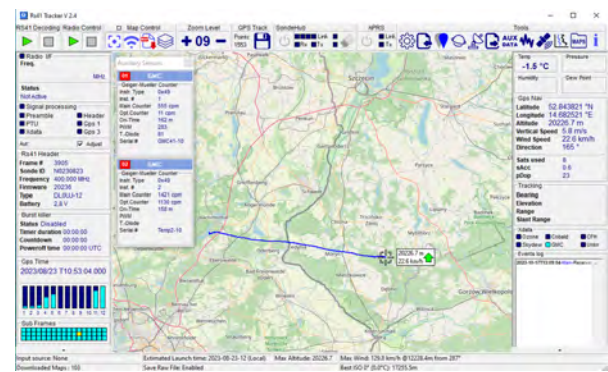


Figure 2: Decoding software RS41Tracker with measurement data, telemetry and trajectory on the map.

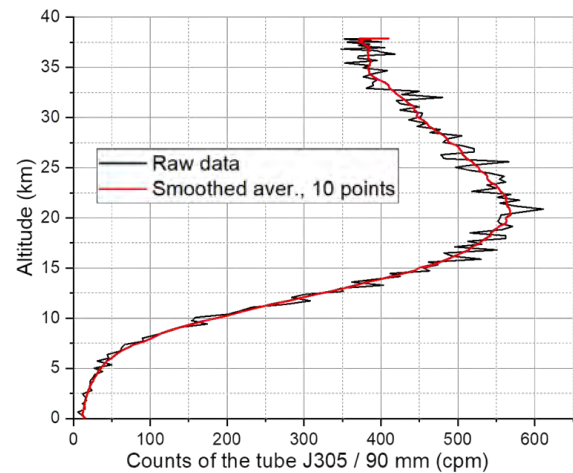


Figure 3: Regener-Pfotzer maximum measured at AstroCamp mission in August 2023.

References

- [1] R. Sarkara *et al.*, Measurement of secondary cosmic ray intensity at Regener-Pfotzer height using low-cost weather balloons and its correlation with solar activity, *Advances Space Res.* **60**, 991 (2017).

* v. tympel@hi-jena.gsi.de

HIGH POWER LASER DEVELOPMENT

Description of optical design software LaserCAD

C. Anschütz^{*1,2}, J. Hein^{1,2}, H. Zhuang^{1,2}, and M. Kaluza^{1,2}

¹HI Jena, Fröbelstieg 3, 07743 Jena, Germany; ²IOQ, FSU Jena

Despite the fact that a number of high quality geometric ray-tracing software tools are commercially available and sometimes even free of charge, all of them are missing the requirement to combine the determination of accurate beam parameters, being scriptable to include optical models in optimization routines, and connecting optical components with their mechanical mounts. Therefore we decided to develop an open-source, parametric software tool designed for optics simulation and visualization. Developed based on the Python programming language, LaserCAD enables users to perform optical tracing and model the outcomes using FreeCAD, an open source 3D computer aided design software.

The hierarchic object-oriented programming of LaserCAD makes it possible to model complex optical setups with parametric dependencies. The Python objects allow an easy to handle grouping, positioning and orientation of optical components as well as any combinations of them. Figure 1 show as an example a 3D model of a optical grating stretcher modeled with LaserCAD and rendered by FreeCAD.



Figure 1: A 3D model of an optical stretcher designed with LaserCAD and rendered with FreeCAD.

The software so far includes:

- ABCD matrix formalism for paraxial analysis of superstructures including astigmatic optics
- Eigenmode calculation of optical resonators
- Beam propagation based on Gaussian optics
- Diffraction from gratings and refraction
- Calculation of the spectral phase for ultrashort laser pulse analysis

* clemens.anschuetz@uni-jena.de

- Optimization of imaging
- Indication of beam positioning on opto-mechanics to avoid collisions and beam clippings

By incorporating fundamental principles such as the law of reflection, Snell's law, and the ABCD-matrices, LaserCAD offers a versatile platform that supports various mutable optical elements, including lenses, mirrors, gratings, and adjustable light sources such as ray groups with diverse distributions and Gaussian beams. The inclusion of peripheral fixation for optical elements in LaserCAD enhances the realism of the 3D modeling and brings it closer to the intricacies of a laboratory setup. Conflicts in the settings can be found easily and therefore be avoided before laboratory implementation.

The ray tracing output was benchmarked against a couple of well established optics design tools like COMSOL [1], FRED citefred, and Mathematica with Optica package [3].

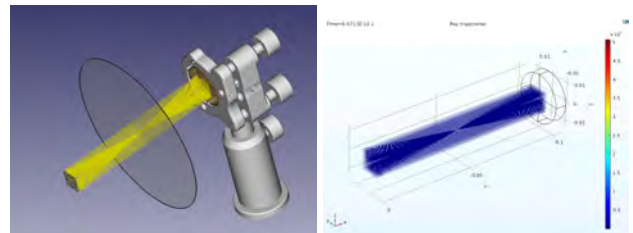


Figure 2: Ray tracing comparison of an square beam hitting a spherical mirror in LaserCAD (left) and COMSOL (right).

One of these test scenarios is depicted in Fig. 2. Both approaches result in equivalent ray paths, but LaserCAD provides a realistic view of the model through incorporation of commercially available opto-mechanics. The whole setup was programmed with only 15 lines of python code.

In future versions it is intended also to implement computation of spatial-temporal couplings of ultrashort laser pulses. An output in form of Kostenbauder[4] matrices was already tested.

References

- [1] <https://www.comsol.de>
- [2] <https://photonengr.com/fred-software/>
- [3] <https://www.wolfram.com/products/applications/optica/>
- [4] A. G. Kostenbauder, IEEEQE, 26 [6], 1990, 1148--1157

Design of a stretcher-compressor-pair for a 2400 nm CPA system

C. Anschütz^{*1,2}, Z. Zhang^{1,2}, J. Hein^{1,2}, and M. Kaluza^{1,2}

¹HI Jena, Fröbelstieg 3, 07743 Jena, Germany; ²IOQ, FSU Jena

Terawatt lasers with a center wavelength of 2400 nm were identified as promising tools for various topics in high intensity laser research. The goal of this project is to develop such a system with the benefit of an all diode pumped classical CPA architecture where an active medium reaching gain saturation provides pulses less influenced by the high power pump as it would be the case for an optical parametric CPA.

Many effects invoked by the interaction of strong laser fields with matter would benefit from longer wavelengths [1, 2]. The normalized vector potential a_0 reads as

$$a_0 = 8.55 \times 10^{-10} \sqrt{I}[\text{W}/\text{cm}^2] \cdot \lambda[\mu\text{m}] \quad (1)$$

for a plane wave with intensity I and wavelength λ and therefore strongly increases with increasing λ . Moreover, with longer wavelengths multi-photon interactions become less important and the role of the field strength increases.

A very promising candidate for the amplification of ultra-short pulses in the mid infrared are Cr^{2+} doped chalcogenides like zinc selenide (ZnSe) and zinc sulfide (ZnS). They offer absorption and emission band widths of several hundred nanometers and peak emission cross sections of more than 10^{-18} cm^2 around 2400 nm wavelength, which is three times longer than the common Ti:sapphire wavelength. In combination with good thermal conductivity, very weak excited state absorption, and available pump sources it is an auspicious laser material [3].

Aiming at the development of a terawatt ultra-short pulse laser based on Cr:ZnSe/S it is planned to stretch 60 fs pulses from a seed laser and to amplify them with two stages afterwards to an energy of 100 mJ.

Up to now the commissioning of the ultra short pulse seed laser has been completed as well as the design, simulation, construction and characterization of the stretcher and compressor module. For the system design our novel LaserCAD tool was used from which a 3D sketch of the stretcher is displayed in [5]. To keep the construction and maintenance of the first prototype flexible and quick, we decided to use only standard components. The stretcher design follows the offner telescope while the compressor module, which setup is depicted in figure 1 consists of four gratings. After successful implementation the whole setup was characterised and results are reported in [4]. The pulses could be transformed from 60 fs from the seed laser back to 92 fs after the compressor with about 26% power conservation. The auto correlation intensity curve after the compressor is shown in figure 2. The overall group delay

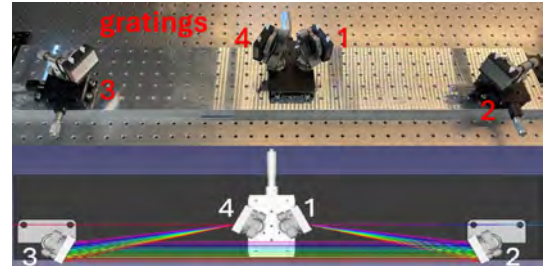


Figure 1: A camera picture of the 4 grating compressor and its 3D model designed with LaserCAD. The gratings are labeled in the order they get hit by the beam.

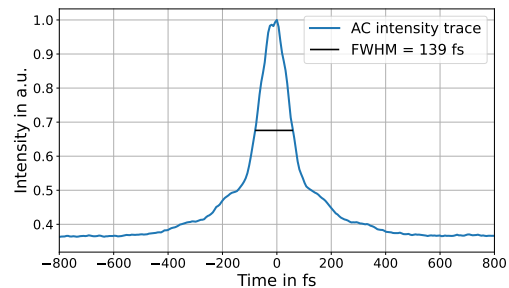


Figure 2: Auto correlation intensity trace of the recompressed pulse. The FWHM of the trace is about 139 fs which corresponds to a pulse with of 92 fs.

dispersion was simulated to be $3.4 \cdot 10^6 \text{ fs}^2$, which leads to a predicted stretching factor of about 3500.

After completion of the stretcher and compressor we will setup and implement the two amplifier stages. As pump source a home made, cryogenically cooled, diode pumped Tm:YAG laser delivering 300 mJ pulses at 1883 nm will be used. For further improvement of the dispersion management mirrors and gratings with larger aperture and higher damage thresholds will be used.

References

- [1] E. Esarey, C. B. Schroeder, W. P. Leemans, *Rev. Mod. Phys.* **81**, 1229 (2009)
- [2] Popmintchev *et al.*, *Nature Photonics* **4**, 822-832, (2010)
- [3] Irina T. Sorokina and Evgeni Sorokin, *IEEE Journal QE* **21**, 273-291, (2014)
- [4] Zedi Zhang, *Simulation and Assembly of an Offner-Stretcher and Compressor pair for Chirped Pulse Amplification at 2400 nm*, master thesis, RLP/IOQ FSU-Jena (2024)
- [5] *Description of optical design software LaserCAD*, C. Anschütz, J. Hein, H. Zhuang, and M. Kaluza, this report

* clemens.anschuetz@uni-jena.de

Update on the Active Stretcher System for the POLARIS Upgrade

G. A. Becker^{*1}, M. Hornung^{1,2}, M. Hellwing¹, F. Schorcht², and M. C. Kaluza^{1,2}

¹Institut für Optik und Quantenelektronik, Friedrich-Schiller-Universität Jena, Germany; ²Helmholtz Institute Jena, Fröbelstieg 3, 07743 Jena, Germany

We present an update on the active pulse stretcher used in the POLARIS laser system. The angle of incidence on the grating has been changed from 60.7° to 54° to match the new pulse compressor. In test operation, pulses were successfully amplified to a pulse energy of 0.3 mJ and stretched to a pulse duration of 1.3 ns. With a test compressor set up, these pulses were compressed to a full-width-at-half-maximum (FWHM) duration below 120 fs.

For the experiments in the new joint target area Fraunhofer, the POLARIS laser system will receive a new compressor system, including a monolithic optical grating, a larger vacuum chamber and new beamlines. Since the angle of incidence of this new compressor will be 54° instead of 60.7° for the old one, the new active stretcher system had to be tested for this angle as well [1]. As the new compressor will be installed in the near future, a smaller test compressor was set up. The current status of the compressor laboratory is described in another part of this annual report. Due to its smaller size, the test compressor can recompress pulses from 1.3 ns instead of the 3 ns of the large compressor. To test the performance of the active stretcher, it was seeded with laser pulses having a duration of 0.5 ps and containing a pulse energy of 70 μ J generated by the front end of the POLARIS laser system. During 15 round trips, these pulses were stretched to 1 ns and amplified to 300 μ J in the active stretcher. Afterwards, the pulses were directed to the test compressor, passing through a DAZZLER HR45-1030 [2] to correct the phase aberrations of the pulses. For this purpose, the compressed pulses were characterized using an IR-Spider [3]. The phase measured by the Spider was used to apply a polynomial phase correction to the DAZZLER. For fine correction, the phase was measured with a WIZZLER and corrected with a WIZZLER-DAZZLER loop [2]. So far, the spectral bandwidth of the laser pulses has been 17 nm, which limits the minimum achievable pulse duration. Since the seed pulses provided by the front-end have a larger bandwidth of 30 nm due to the use of an XPW process [4], it is necessary to broaden the bandwidth of the amplified pulses by shaping the gain profile of the amplifier part of the active stretcher by using tunable spectral filters [5], which will be done in the next step.

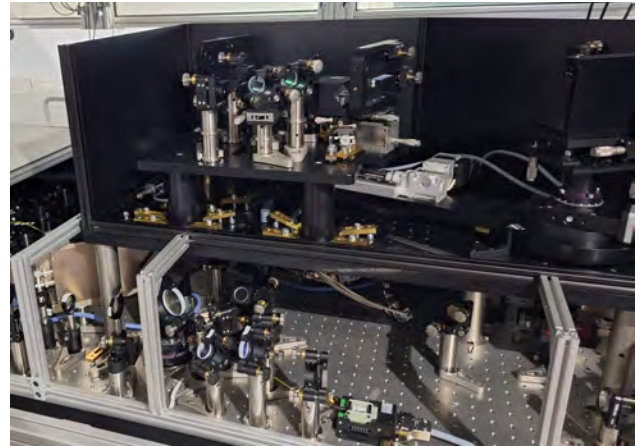


Figure 1: Photography of the current setup of the active stretcher

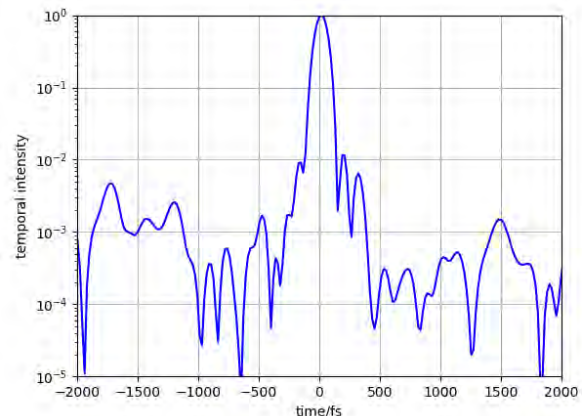


Figure 2: Pulse duration measurement of a 116 fs (FWHM) laser pulse. The laser pulse had a spectral bandwidth of 17 nm (FWHM).

References

- [1] M. Hornung *et al.*, HI Jena Annual Report, 15 (2022).
- [2] <https://fastlite.com>
- [3] <https://www.ape-berlin.de/>
- [4] M. Hornung *et al.*, HI Jena Annual Report, 17 (2021).
- [5] S. Hornung *et al.*, Opt. Lett. **41**,4708 (2016).

* georg.becker@uni-jena.de

POLARIS Pulse Compressor and Beam Transport Upgrade

M. Hornung^{*1,2}, M. Ostermann², M. Hellwing², F. Schorcht², and M. C. Kaluza^{1,2}

¹Institut für Optik und Quantenelektronik, Friedrich-Schiller-Universität Jena, Germany; ²Helmholtz Institute Jena, Fröbelstieg 3, 07743 Jena, Germany

We report on the upgrade of the POLARIS pulse compressor and the beam transport towards the target areas.

In Figure 1 the schematic layout of the pulse compressor upgrade including parts of the beamline to the different target areas is shown. The details of the new optical configuration for the compressor have already been described in [1].

The gratings of the pulse compressor will be located in two different chamber (chamber 1 and 2) which are connected with a tube to enable up to 6 m of separation length. The roof-top mirror required for 2-pass compression with only two gratings will be placed in chamber 1 together with the in- and outcoupling optics. Chamber 1 is currently in production by Streicher, spol. S r.o. Plzeň in the Czech republic. The delivery and installation is expected in Q3/2024. Chamber 2 is an existing chamber which will be reused for the new compression setup. After compression the laser pulse is deflected in turning chamber 3 and sent to the switchyard chamber 4. Chamber 3 was manufactured by PINK GmbH Vakuumtechnik, Germany. In the switchyard chamber the pulse can either be sent to the existing POLARIS target area below the compressor lab ortowards the new Target Area Fraunhofer (TAF).

The switchyard chamber which was formerly used a the main compression chamber will be modified to fit to the newly developed beam transport system. For this purpose three DN500 and one DN400 flanges are attached to the chamber.

*Marco.Hornung@uni-jena.de

Since the beam height in the new target area is clearly above the compression beam height an additional in-vacuum periscope is required to lift the POLARIS beam height from 0.8 m to 1.56 m above ground. The periscope will be installed in chamber 5 which is currently still in its design phase. Chamber 6, a 90° turning chamber, is required to send the compressed laser pulses in the direction of the new target area. This chamber was manufactured by Pfeiffer Vacuum, Components and Solutions GmbH, Germany.

This chamber has to be mounted more than 5 m above ground and a stable frame with optimized and reduced vibration characteristics has to be developed. An illustration of this frame is depicted in Figure 1 in orange.

Special emphasis was given to the overall stability of the optical mountings in the vacuum chambers. All breadboards were optimized and improved to enable highest stability with respect to mechanical vibrations. For example, the breadboards of the chamber 2,3 and 4 will be supported be massive granite blocks instead of expansive metal constructions.

For example, the breadboards of the chambers 2,3 and 4 will be supported be massive granite blocks instead of metal constructions. Currently, the old POLARIS compression lab (size 60 m²) is cleared from the technical installations and wall breakthroughs are inserted for the beam transport. Further-more, the floor will be prepared for the new installations.

References

- [1] M. Hornung, HI Jena annual report, p. 16 (2022).

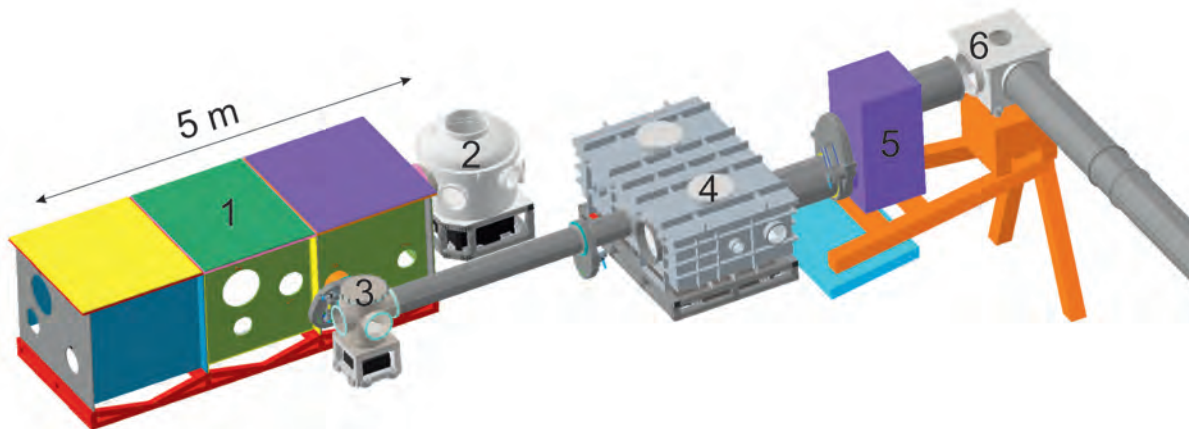


Figure 1: Layout of the POLARIS pulse compressor with switchyard and beam transport to the different target areas. 1: pulse compression chamber, 2: grating chamber for pulse compressor, 3: 90° turning chamber, 4: switchyard chamber, 5: periscope chamber and 6: turning chamber.

Beam Transport from POLARIS and JETi200 to the new Target Area Fraunhofer (TAF)

M. Hornung^{*1,2}, M. Ostermann², T. Köhler², A. Sävert^{1,2}, M. Zepf^{1,2}, and M. C. Kaluza^{1,2}

¹Institut für Optik und Quantenelektronik, Friedrich-Schiller-Universität Jena, Germany; ²Helmholtz Institute Jena, Fröbelstieg 3, 07743 Jena, Germany

We describe the schematic layout of a beam transport system at HI Jena. This beam transport system will deliver pulses from JETi200, JETiONE and POLARIS from their individual labs to the Target Area Fraunhofer.

For the future laser plasma experiments in TAF it will be essential to bring all laser pulses in the target chamber together. The purpose of this project is to develop an ultra-stable beam transport and modification system which provides unique features for future experiments. An overview of the planned vacuum system is shown in figure 1. The JETi200 and JETiONE laser pulses, starting at (1), are sent through DN320 ISO-K vacuum tubes and turning chambers to the wedding chamber (3).

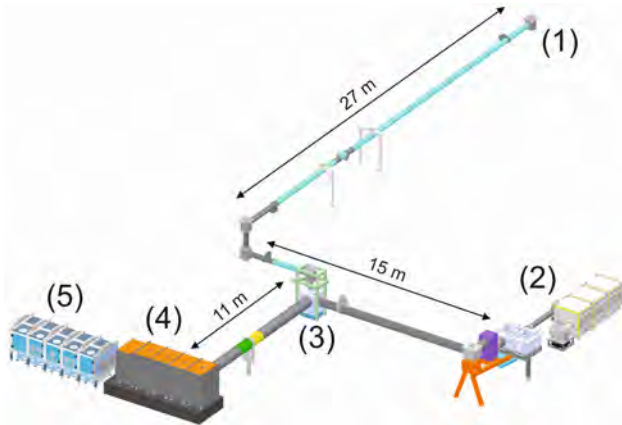


Figure 1: Simplified layout of the vacuum system for laser beam modification and transport at HI Jena. (1) JETi200 and JETiONE laser system. (2) POLARIS laser system. (3) wedding chamber. (4) beam shaping chamber (5) target chamber.

The POLARIS laser pulses (2) are propagating through DN500 ISO-K vacuum tubes through a periscope and a turning chamber also towards the wedding chamber. Continuing from the wedding chamber all three pulses are propagating parallel into the beam shaping chamber (4). The beam shaping chamber provides a variety of possibilities to modify and optimize the laser pulses before they are sent to the target chamber (5). Finally, in the target chamber which was described before in [1], the high-intensity experiments are carried out.

In Figure 2 a sectional view of the wedding chamber is displayed. The wedding chamber is currently in production at Pfeiffer Vacuum Components & Solutions GmbH, Ger-

many and its delivery is expected in Q3/2024. The breadboard with a thickness of 100 mm is mounted with 140 mm diameter thick connection feet onto a 220 mm thick granite block. The granite block will be bolted and glued onto the concrete floor for maximum stability.



Figure 2: Sectional view of the wedding chamber. 1: vacuum chamber (1.0 m x 1.0 m x 1.4 m). 2: granite base (0.9 m x 1.0 m x 0.2 m). 3: breadboard. 4: connecting foot.

The beam shaping chamber ((4) in Fig.1) is currently in its final construction phase. With a size of 6.0 m x 1.6 m x 2.2 m this chamber will provide plenty of space for different beam modifications. A plasma mirror as well as a pulse shortening unit are envisioned to be installed. Furthermore, the polarisation of each laser pulse can be rotated and long focal length off-axis parabolas can be installed to enable experiments with long focal lengths of up to 15 m. Special attention to the stability is paid with a simulated and optimized shear wall construction for the ultra-stable mounting of two breadboards in different heights of 1.0 m and 2.15 m above ground.

References

- [1] P. Hilz, HI Jena annual report, p. 20 (2022).

*Marco.Hornung@uni-jena.de

Vibration Measurements and Improvement of the TAF Beam Transport System

M. Hornung^{*1,2}, R. Berg-Jahnke³, D. Heiland³, T. Köhler², and M. C. Kaluza^{1,2}

¹Institut für Optik und Quantenelektronik, Friedrich-Schiller-Universität Jena, Germany; ²Helmholtz Institute Jena, Fröbelstieg 3, 07743 Jena, Germany; ³Baudynamik, Heiland & Mistler GmbH, Bergstraße 174, 44807 Bochum

We present measurements and findings in the context of the stability of the beam transport to the TAF target area. JETi200 and POLARIS will be used together in future experiments in this new target area. This requires low spatial jitter of the laser pulses and therefore very low vibration levels of the beam transport system. Here, we give an overview how the stability aspect influences the design and construction of the beam transport system.

The three individual laser systems JETi200, JETiONE and POLARIS will be used together in the target area Fraunhofer (TAF). Since these laser pulses have fs pulse duration and μm size focal spots the requirements for their stability and synchronization are outstanding. The temporal synchronisation will be realized with a state-of-the-art temporal synchronisation system. In this report we give an overview about ongoing work with respect to the overall spatial stability of the laser infrastructure components required for the beam transport to the new of target area Fraunhofer (TAF). In order to identify suitable positions for the beam transport elements we performed a measurement campaign of the building dynamics at HI Jena in collaboration with Baudynamik Heiland & Mistler GmbH, Germany.

In this campaign the vibration level of all corresponding laser labs (JETi200, POLARIS and TAF) was measured simultaneously in a 24 h measurement at 32 different measurement points under different operation conditions. One exemplary measurement of a vibration velocity measurement during the daytime in the POLARIS labs is shown in figure 1. The measured vibration level is well below the so called “nano-EF” vibration criteria, which stands for very strict requirements in REM- and TEM technique for

sub-Angstrom resolution [1]. Also the partially stronger vibration criteria G (VC-G) is fulfilled in most cases. That means the overall vibration level within the HI Jena laser labs is classified as very good. Nevertheless, and not shown in the exemplary measurements in figure 1, some positions in our labs were not suitable for the installation of beam transport components due to enhanced vibrations or too less stiffness. In some cases we found equivalent alternative positions and in other cases we had to modify and reinforce the building structure. In figure 2 the accepted position of a future vacuum chamber to combine JETi200, JETiONE and POLARIS is shown. During the measurements it was found that the ground at this position led to a stability level well above the nano-EF criteria and was therefore not suitable. Here, the foundations had to be reinforced with a well defined portion of reinforcing steel and connection to existing stable structures to increase their stiffness. A similar modification is also required for a position of the JETi200-JETiONE beamline and this modification is still ongoing. Once stable mounting positions for all parts of the beamline have been found vibration optimized frames will be designed to support the mounting of the required vacuum chambers. Due to the large mounting height of some components (up to 5 m above ground) the design and construction of the frames is challenging.

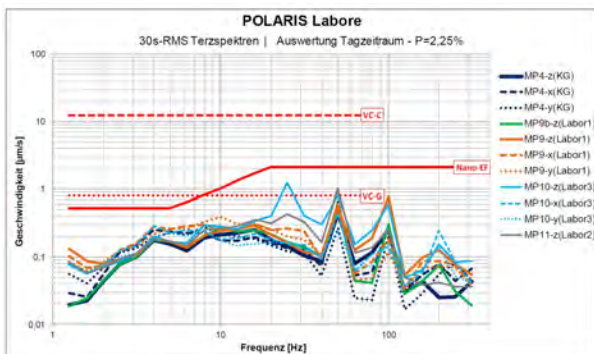


Abbildung 4-6: Gemessene Schwinggeschwindigkeits-Terzspektren in den POLARIS Laboren

Figure 1: Measured vibration velocity spectrum of the POLARIS laser labs.



Figure 2: Basement for a beam transport vacuum chamber. a) exposed problematic area. b) newly cast base.

Due to the knowledge of the vibration levels and the stiffnesses of the mounting positions we were able to optimize all the required mounting positions for the beamline mirrors and provide a low spatial jitter beam transport system in the future. This project is still ongoing.

References

[1] VDI guidelines, VDI 2038-2, Germany (2013).

* Marco.Hornung@uni-jena.de

Status of the Tango Control system at JETi200

D. Hollatz^{*1,2}, A. Sävert^{1,2}, P. Hilz^{1,2}, and M. Zepf^{1,2}

¹HI Jena, Fröbelstieg 3, 07743 Jena, Germany; ²IOQ, FSU Jena

The extension building of the Helmholtz-Institute Jena offers new opportunities for high intensity laser experiments with JETi200 and POLARIS in the new Target Area Fraunhofer (TAF). The scale of those experiments with both lasers together plus experimental diagnostics and data management requires a common control system. We decided to use Tango Controls as the framework to build this system. We present the current status and progress since last years annual report.

JETi200 and POLARIS are two high-power laser systems at the Helmholtz-Institute Jena. These two systems are operated completely independent from each other since their installation over 10 years ago. With the new extension building completed in late 2022, Target Area Fraunhofer offers the opportunity to perform experiments with both lasers at the same time.[1, 2] To enable these, significant infrastructure modifications are necessary, for example the connection of both vacuum and safety systems along with beamlines through the building. Another key area is laser control from a new control room and unified data acquisition. To provide this functionality, we decided to build a distributed control system for both lasers and the target areas. We considered different options for the framework, for example EPICS, Tango Controls and GEECS, with each having unique advantages and drawbacks.[3] After getting in touch with other institutes using the respective frameworks as well as attending community meetings, we made the decision to use Tango Controls at HI Jena. We established contacts to other institutes of similar scale as HI Jena that are currently building a Tango Controls system to discuss concepts and exchange ideas, specifically LMU Munich, MBI-Div-B in Berlin and HHU Düsseldorf. We are also in contact with DESY, HZDR and GSI.

To make HI Jena ready for the control system, we need to update our IT infrastructure. We acquired a new PC with sufficient processing power, network bandwidth and data storage to function as the Tango Host for JETi200. This machine features a 32-core AMD CPU, an NVIDIA A100 GPU, 2x 10Gbit/s Ethernet and NVMe SSD storage. The control system also requires a network upgrade to connect JETi200 with POLARIS and TAF. We purchased 10Gbit/s switches to raise the network speed of each subnet to 10Gbit/s. The switches will be interconnected with optical fibers that provide 100Gbit/s bandwidth, making HI Jena ready for a control system with hundreds 1Gbit/s cameras and support for multiple modern 10Gbit/s cameras.

The Tango Host will run the Tango database as well as device servers for Allied Vision cameras and our own step-

per motor control boxes. The Tango database stores configuration parameters like IP addresses and hardware properties like camera and motor controller settings. To control our Allied Vision cameras, we use TangoVimba, a device server developed by Johannes Blume from DESY that we could adapt for HI Jena, which saved us significant development time. The device server for our own stepper motor control boxes, called BahrmannBoxes, was developed by us and tested successfully at JETi200. Together with LMU and MBI, we work on a laser beam drift compensation within the Tango Controls ecosystem. The prototype was tested successfully and it is planned to use this at an experimental campaign at JETi200 target 2. To further safe development time, we plan to use other frameworks from the Tango Controls ecosystem, specifically Taurus, Sardana and HDB++. Taurus is a toolkit to develop GUI's for Tango devices using PyQt, which is especially useful for smaller standalone applications like the laser beam drift correction. Sardana is a control system framework that is compatible with Tango to provide high level functionality and simple automation, for example parameter scans and structured experiment data acquisition. It serves as a front end for users to the control system. HDB++ is a database for Tango attributes, so it can be used for automated logging of experiment parameters like motor positions, temperatures, laser energy and so on to build a history of the experiment. It can also be used for experiment data storage.

We also want to control JETi200 via Tango, which is a commercial system from Amplitude Technologies. We are in contact with the company to purchase a Tango Gateway between the Amplitude system and Tango.

Independent from but related to the Tango control system is the automatic pointing stabilization for JETi200. Here we use an artificial neural network to predict the pointing angle of the next laser shot and correct it in advance to reduce pointing fluctuations.[4] The hardware to perform these calculations is installed in the Tango Host PC. Beyond that, a control system paves the way for high-level feedback loops, for example an automated LWFA electron beam optimization. Once the control system is operational, we will start to work on these.

References

- [1] D. Hollatz, HIJ annual report, (2022).
- [2] P. Hilz, HIJ annual report, (2023).
- [3] S. Feister *et al.*, arXiv.2306.01661, (2023).
- [4] A. Sävert, HIJ annual report, (2023).

*dominik.hollatz@uni-jena.de

Dependence of transverse mode instability threshold on the modal content of the seed light in fiber amplifiers

Yiming Tu^{*1,2}, Cesar Jauregui^{2,3}, and Jens Limpert^{1,2,3}

¹HI Jena, Fröbelstieg 3, 07743 Jena, Germany; ²IAP, FSU Jena, Albert-Einstein-Straße 15, 07745 Jena, Germany;

³Fraunhofer Institute for Applied Optics and Precision Engineering, Albert-Einstein-Str. 7, 07745 Jena, Germany

We experimentally investigate the impact of the modal content of the seed beam on the transverse mode instability threshold in high-power fiber amplifiers. We have built a system comprising a spatial mode multiplexer that allows manipulating the power content of the fundamental mode and the higher-order mode in the seed beam. Such beams, with the same power but different modal contents, were coupled into a multimode active rod-type fiber and the evolution of the TMI threshold was studied.

Transverse mode instability (TMI) is a nonlinear thermal effect that limits the output average power of high-power fiber laser systems with diffraction-limited beam quality [1]. Studying TMI inspires mitigation strategies which can improve the performance of high-power fiber laser systems for a wider range of scientific applications. TMI manifests itself as a dynamic energy transfer between transverse modes once the average power of the system reaches a certain value (which is called the TMI threshold). The physical origin of TMI is rooted in a quasi-periodic modal interference pattern (MIP) formed by at least two transverse modes propagating along the fiber. The MIP then inscribes itself, through the induced heat and thermo-optic effect, into a refractive index grating (RIG) in the fiber core, which enables modal energy transfer if a phase shift between the MIP and RIG exists [2].

In this work we have integrated a spatial mode multiplexer into a seed system which allows for an accurate control of the modal content of the seed beam. With this system we have managed to experimentally investigate the impact of the seed modal contents on the TMI threshold. During our experiment, the seed beam was fixed at 3 W but with different modal contents and was 4-f imaged onto the end facet of a multimode, active, rod-type fiber, which has 85 μm core, 200 μm cladding and 76 cm length. The TMI threshold was measured by the 2 photodiode method [3]. Additionally, a corresponding simulation was also carried out with the dynamic model described in [4].

Figure 1 shows the evolution of the TMI threshold as a function of higher-order mode content in the seed beam both for the experimental data (in blue) and for the simulations (in red). As can be seen, there is an excellent match between simulation and experiments. When the fundamental mode (FM) is dominant the TMI threshold drops rapidly as the higher-order mode (HOM) content increases. Such drop is not surprising, since the amplitude of the RIG becomes stronger with increasing HOM content and, thus, the system becomes more sensitive to the noise, which implies

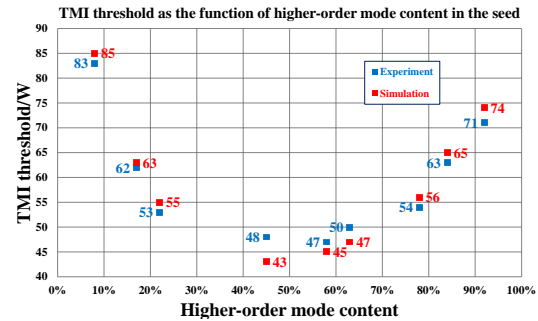


Figure 1: TMI threshold as a function of higher-order mode content in the seed beam both experimentally measured (blue points) and simulated (red points)

a lower TMI threshold. What has not been shown before is that the TMI threshold increases again when the HOM content exceeds 50%. The reason for that is related to gain saturation, which starts weakening the amplitude of the RIG from the outer boundaries of the core inwards (in the radial direction) as the HOM content increases. This mechanism is akin to that leading to an increase of the TMI threshold with higher gain saturation for a dominant FM [5]. The difference is that with a dominant FM mode the RIG is weakened from the inner part of the core outwards (in the radial direction) and with the dominant HOM the direction of weakening is mostly reversed.

In summary, we have carried out a systematic measurement of the TMI threshold with respect to the HOM content of the seed, together with the corresponding simulation. Both experiment and simulation showed a very good agreement and revealed the decrease and later increase of the TMI threshold as the HOM content of seed beam steadily grows. Gain saturation plays the main role in explaining this behavior. This work would enlighten the research for the spatial beam control and the potential power scaling for high-power fiber laser systems.

The authors acknowledge support by DFG (416342637, 416342891) and FhG CAPS.

References

- [1] C. Jauregui *et al.*, Nat. Photonics, **7**, 861 (2013).
- [2] C. Jauregui *et al.*, Adv. Opt. Photonics, **12**, 429 (2020).
- [3] H. J. Otto *et al.*, Opt. Express, **20**, 15710 (2012).
- [4] C. Jauregui *et al.*, Opt. Express, **26**, 10691 (2018).
- [5] A. V. Smith *et al.*, Opt. Express, **21**, 15168 (2013).

* yiming.tu@uni-jena.de

High power laser sources based on a 49-core Ytterbium doped fiber

A. Klenke^{*1,2,3,4}, M. Bahri³, C. Jauregui^{3,4}, J. Nold⁴, S. Haarlammert⁴, T. Schreiber⁴, and J. Limpert^{1,2,3,4}

¹HI Jena, Fröbelstieg 3, 07743 Jena, Germany; ²GSI GmbH, Planckstraße 1, 64291 Darmstadt, Germany; ³FSU Jena, Albert-Einstein-Str. 15, 07745 Jena, Germany; ⁴Fraunhofer IOF, Albert-Einstein-Str. 7, 07745 Jena, Germany

We present the next generation multicore fiber with 49 Ytterbium-doped cores that can be employed either for the generation of femtosecond pulses via coherent beam combination, as well as for high energy nanosecond pulses via incoherent beam combination.

Multicore fibers have the potential to combine the advantages of optical fibers (such as their high average power capability, high efficiency and good beam quality) with those stemming from the large beam areas commonly used in other laser architectures. We have previously demonstrated up to 500 W average power with ultrashort pulses when combining the output beams from a 16 core fiber via coherent beam combination into a single, high-quality, output beam [1]. For the next generation of multicore fibers, we have increased the core count to 49 and implemented an air-cladding for optical pump guiding. In addition, we explore the incoherent beam combination method for nanosecond pulses as an additional beam combination concept that does not require phase control of the individual beams and allows to extract the maximum energy from the fiber due to the longer pulse duration, which opens up a new class of applications.

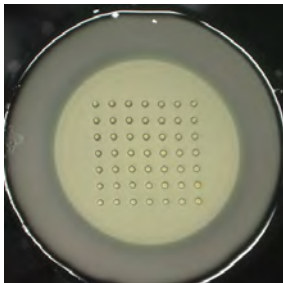


Figure 1: Image of the fiber end-facet showing the 49 cores and the air-cladding for guiding of the pump light.

The realized multicore fiber is based on the rod-type geometry, with the end-facet shown in figure 1. It contains 49 ytterbium-doped cores in a square arrangement. In contrast to the previous fiber, we have implemented an air-cladding that provides a higher numerical aperture which enables optical pumping with the highest available power. The fiber was drawn in different sizes, where a version with 25 μm core diameter has sufficient beam quality to support coherent beam combination. A version with 30 μm cores was then employed for incoherent beam combination. In both cases, fiber lengths of around 1 m were chosen.

For the coherent combination setup, we use a system design based on segmented-mirror splitters (SMS) elements

for beam splitting and combination. In between, two identical multicore fibers acting as the pre-amp and main-amp are inserted. To allow for scalability to this high channel count, we use a compact phase array based on MEMS technology together with a in-house developed software based phase stabilization software running on a PC [2]. As the fibers are not polarization maintained, we realized a beam array polarization controller with a spatial light modulator. This setup is seeded by frontend providing stretched femtosecond pulses with 1 ns duration and at the output, the now combined pulses are compressed with a grating compressor. With this setup, we have observed combination efficiencies of up to 80%, limited by the beam positioning and beam quality of the individual beams. However, the combined beam showed excellent beam quality with an M^2 value of less than 1.1x1.1. Preliminary results show 330 fs duration pulses with up to 1.75 mJ energy.

The multicore fiber is also a perfect platform for incoherent combination. In this concept, the output beams from the individual cores are focused to a common point and, because they are assumed to be incoherent, the result is the addition of the individual beam intensity profiles, which provides a homogenization effect. By using a multicore fiber as a Q-switch oscillator, there is no inherent coherence between the emitted nanosecond pulses from the individual beams. Up to 10 mJ total energy with repetition rates up to 5 kHz could be achieved. An additional main amplifier then boosts the output to up to 110 mJ total energy, which is a new record for fiber based sources. This corresponds to the extraction up to 75% of the energy that can be stored in the fiber. This high energy level makes these compact setups a good driver for specific applications, e.g. next generation incoherent EUV sources.

Future fiber developments will focus on allowing for higher core diameters while sustaining near-diffraction limited beam quality, which is a technology already shown for single-core fibers. This will allow for coherent beam combination reaching Joule-class as well as incoherent beam combination systems with over 1 J of total pulse energy.

The authors acknowledge funding from TAB (FGR0022), FhG CAPS, ERC SALT, BMBF (13N15244, PINT), DFG (416342637, 416342891)

References

- [1] A. Klenke *et al.*, Opt. Lett. **47**, 345 (2022).
- [2] A. Klenke *et al.*, Opt. Express **26**, 12072-12080 (2018).

* a.klenke@hi-jena.gsi.de

Intensity Tagging for Ultrashort High-Power Laser

Xinhe Huang^{*1,2}, Alexander Sävert¹, and Matt Zepf^{1,3}

¹Helmholtz Institute Jena, 07743 Jena, Germany; ²Albert-Ludwigs-Universität Freiburg, 79098 Freiburg, Germany;

³Friedrich-Schiller-Universität Jena, 07743 Jena, Germany

The precision of strong field quantum electrodynamics experiments is challenged by shot-to-shot laser intensity fluctuations. We propose a high-precision, non-linear diagnostic method for on-shot tagging of peak intensity. This involves using second harmonic generation to create a nonlinear replica of the focal spot and measuring the ratio of peak fluences between the fundamental and second harmonic beams.

The precise diagnostic on laser intensity is critical to the LUXE (Laser Und XFEL Experiment) project [1] at DESY. It will measure processes in the SFQED regime with high precision by either directly colliding 17 GeV electron bunches from the XFEL electron accelerator or converting them to high-energy photons via Bremsstrahlung with a tightly focused laser beam. The main challenge is the shot-to-shot laser intensity fluctuation, as simulations show that a 5% variation in laser intensity can cause up to a 40% uncertainty in the Breit-Wheeler pair production rate. Hence, we developed a method to tag the laser pulse intensity shot-to-shot with better than 1% precision.

We use second harmonic generation (SHG) in an all-optical setup to tag the laser pulse intensity. A near-infrared (NIR) laser pulse is focused into a thin beta-barium borate (BBO) crystal, and the focal spot of the fundamental beam and its frequency-doubled replica are imaged onto a CCD. In our experiment, with SHG conversion rates of less than 0.1%, the generated 2ω pulse intensity is proportional to the square of the fundamental beam's intensity. The ratio R , defined as $R = \sqrt{F_{2\omega}}/F_\omega$, where F is the fluence, can be obtained by capturing the focal plane images of both the fundamental and SHG beams. This ratio can be used as a

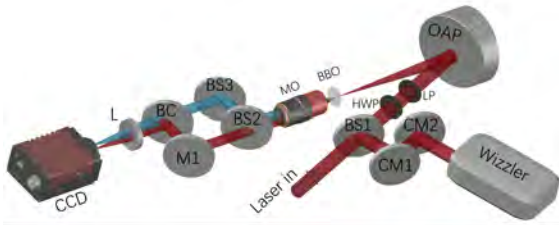


Figure 1: Laser intensity tagging system: For the beam reflected by BS1 (beam splitter), its spectral phase is compensated by the chirped mirrors (CM), and its temporal duration is measured by a Wizzler. A BBO crystal with a thickness of $10 \mu\text{m}$ is positioned at the focal plane for SHG. An imaging system consisting of a microscope objective (MO) and an achromatic lens (L) images the same focal plane to a CCD camera for two wavelengths.

* xinhe.huang@uni-jena.de

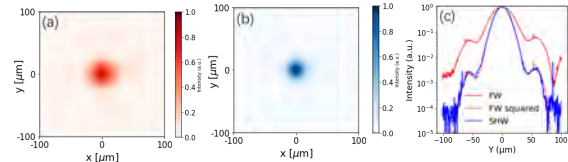


Figure 2: (a) The focal spot of the fundamental beam (b) the focal spot of the 2ω beam (c) the lineout of the fundamental focal spot (solid red), the 2ω focal spot (solid blue), and the red curve squared in dotted red.

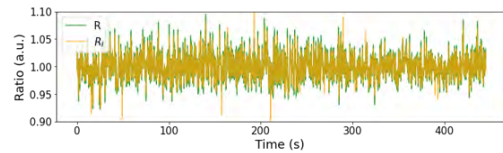


Figure 3: R and R_I for over 2000 shots.

reference for on-shot intensity tagging.

The experiments were carried out with the JETi-laser system at the Institute of Optics and Quantum Electronics in Jena. The experiment setup is shown in Fig.1. Fig.2 displays the focal spot images. In Figure 2(c), the blue curve and the red dotted curve overlap, showing a quadratic relationship between each corresponding point in the transverse plane of the two focal spots.

We take focal spot images at 5 Hz for more than 2000 shots. Fig.3 plots the results of the fluence ratio R and the intensity ratio $R_I = R\tau_\omega/\sqrt{\tau_{2\omega}}$ with τ the pulse duration. Compared to R with an RMS of 2.4%, the RMS of R_I is 2.1%, indicating that the contribution from pulse duration fluctuations is disentangled.

The relative fluence precision within FWHM of focal spot is 0.01%, determined by the Poisson noise \sqrt{N}/N with N the total counts within FWHM. The Wizzler measures the temporal duration with a 0.2% error for near-Fourier transform pulses [2].

In this work, we assessed the precision of laser intensity measurement using second harmonic generation. This method approaches the 1% precision required by the LUXE project. In the LUXE experiment, this method will be applied to the actual focal spot and cross-verified with comprehensive intensity measurements.

References

- [1] H. Abramowicz *et al.*, EPJ Spec. Top. **230**, 2445 (2021).
- [2] T. Oksenhendler, "Self-referenced spectral interferometry theory," arXiv:1204.4949 (2012).

Compact, folded multi-pass cell for energy scaling of post-compression

A. Schönberg*¹ and C.M. Heyl^{1,2,3}

¹Deutsches Elektronen-Synchrotron DESY, Notkestrasse 85, 22607, Hamburg; ²HI Jena, Fröbelstieg 3, 07743 Jena, Germany; ³GSI Helmholtzzentrum für Schwerionenforschung GmbH, Planckstrasse 1, 64291 Darmstadt

Recent advances in Multi-pass cell (MPC)-based laser pulse post-compression have established this technology over a wide range of parameters. A key challenge is pulse energy up-scaling, where the main limitation stems from the laser-induced damage threshold (LIDT) of the MPC mirrors. To overcome this, either higher LIDT coatings or larger MPCs are needed. However, larger MPC sizes may become impractical if laser pulse energies exceeding a few tens of millijoule are targeted, necessitating alternative methods. We address challenge and develop a novel, energy-scalable, compact MPC (CMPC) scheme enabling post-compression of high-energy pulses while maintaining compact setup sizes.

Ultrafast laser technology providing ultrashort, high-peak power laser pulses is pivotal for various applications including e.g. attosecond pulse generation and laser-plasma acceleration. For these applications, the combination of high peak and average power is often essential. However, combining both peak and average power scalability remains a challenge for ultrafast laser systems.

Post-compression techniques, especially, if combined with high average-power ytterbium lasers provide a promising route to overcome these limitations. In particular, Herriott-type multi-pass cells (MPCs) have been established as a powerful scheme for the generation of ultrashort, high peak- and average power laser pulses, with large compression factors of typically around 10-20 [1]. However, energy up-scaling is still a key challenge for these systems. MPCs are fundamentally limited by the laser-induced damage-threshold (LIDT) of the mirror coatings. Energy-scaling of MPCs is possible by scaling the size of the MPC [1]. However, at large sizes, e.g. about 10 m for 200 mJ [2], MPCs can become impractical for standard laboratory settings.

To achieve pulse energy scalability while maintaining a compact setup, we propose a new MPC geometry. Our compact multi-pass cell (CMPC) uses a weakly focused fundamental mode and a linear beam pattern, allowing the beams to be folded inside the cell using two additional planar mirrors (Figure 1). This approach introduces a new energy scaling parameter, the folding ratio Γ , which reduces the setup length to the effective length $L_{\text{eff}} \approx L/\Gamma$, as illustrated in Figure 1A.

As proof of concept, we demonstrate spectral broadening of 1030 nm, 8 mJ, 1 ps pulses in a CMPC with an effective length of around 45 cm, while maintaining a moderate maximum mirror fluence of 170 mJ/cm². The CMPC

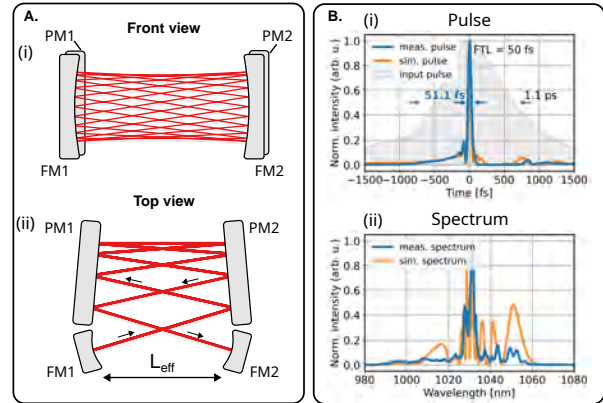


Figure 1: A. Layout of the CMPC scheme B. (i) Measured input- and compressed pulses, along with simulated pulses. (ii) Measured and simulated spectra. [3].

focusing mirrors FM1 and FM2 (Fig. 1A) have a radius-of-curvature of $R = 25$ m and the CMPC length L , which is defined by the optical path length traveled by the beam from FM1 to FM2 (or vice-versa), is $L \approx 8.63$ m. The folding ratio is set to $\Gamma = 25$, so that $L_{\text{eff}} \approx 8.63 \text{ m}/25 \approx 35$ cm. In our case, $L_{\text{eff}} \approx 45$ cm is slightly longer than the calculated value, since the focusing mirrors are placed at a certain distance behind the planar mirrors, due to geometrical restrictions. The total number of reflections on the mirrors then amounts to $2N\Gamma = 550$. Nevertheless, we measure a transmission of $> 89\%$ through the CMPC at full power (8 W). Spectral broadening is achieved using ambient air at 1 bar as nonlinear medium and the pulses are then sampled using a wedge reflection and compressed down to 51 fs (Fig. 1B).

In conclusion, we have developed a compact MPC, enabling energy-scaling of MPC-based post compression at small footprint. We demonstrated spectral broadening of 1030 nm, 8 mJ, 1 ps in a 45 cm long setup. Our results can prospectively enable further energy up-scaling, supporting e.g. 100 mJ level pulses in a compact, 2 m long table-top setup.

A.S. and C.M.H. acknowledge the Helmholtz-Lund international graduate school HELIOS for funding and support.

References

- [1] A.-L. Viotti *et al.*, *Optica*, vol. **9**, no. 2, Feb. 2022.
- [2] Y. Pfaff *et al.*, *Optics Express*, vol. **31**, no. 14, Jun. 2023
- [3] A. Schönberg *et al.*, High-Brightness Sources and Light-Driven Interactions Congress, paper HTu3B.2 (2024)

* arthur.schoenberg@desy.de

More than 100-fold pulse compression by hybrid multi-pass multi-plate spectral broadening

M. Seidel^{*1,2,3}

¹HI Jena, Fröbelstieg 3, 07743 Jena; ²GSI Helmholtzzentrum für Schwerionenforschung GmbH, Planckstrasse 1, 64291 Darmstadt; ³Deutsches Elektronen-Synchrotron DESY, Notkestrasse 85, 22607 Hamburg

Yb-ion based lasers have been established in ultrafast optics laboratories as new workhorses over the past years. They gradually replace Ti:sapphire technology because of their superior power-handling capability and reliability. However, Yb-lasers do not provide sufficient gain bandwidth to generate few-cycle pulses which are necessary for extreme nonlinear optics applications. We have recently shown for the first time nonlinear post-compression of picosecond pulses to sub-10 fs at GW pulse peak power levels, which are well suited for applications like high-harmonic generation. The reported setup uses the hybrid multi-pass multi-plate technique in two consecutive compression stages. It does not require vacuum chambers or pressure vessels and has a very compact footprint of less than 1 m².

Multi-pass cells (MPCs) have advanced the nonlinear spectral broadening method to record-high average power levels as well as unprecedented combinations of pulse compression factors and optical efficiencies [1]. However, studies which report compression to the few-cycle regime (three carrier cycles correspond to about 10 fs at 1030 nm central wavelength) are still relatively scarce since large MPC mirror bandwidths with precise dispersion control are needed [1]. With the setup shown in Fig. 1, we were able to reduce the durations of picosecond pulses emitted from a Yb:YAG amplifier by more than 100-times to 8.2 fs. The hybrid multi-pass multi-plate technique [2] was used to compress the picosecond pulses to sub-50 fs in a first stage (MPC1). In a second stage (MPC2), the dispersion of complementary chirped mirrors was matched to the dispersion of two 1 mm thin Kerr media. In this way, spectra covering

*m.seidel@hi-jena.gsi.de

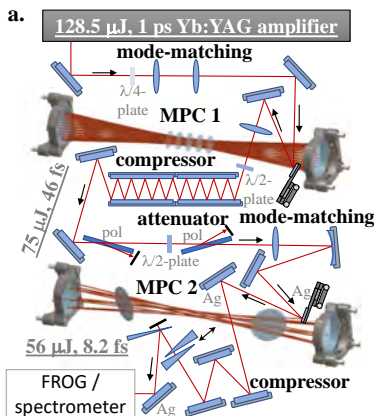


Figure 1: Double-stage hybrid pulse multi-pass multi-plate setup. Reprinted from [3].

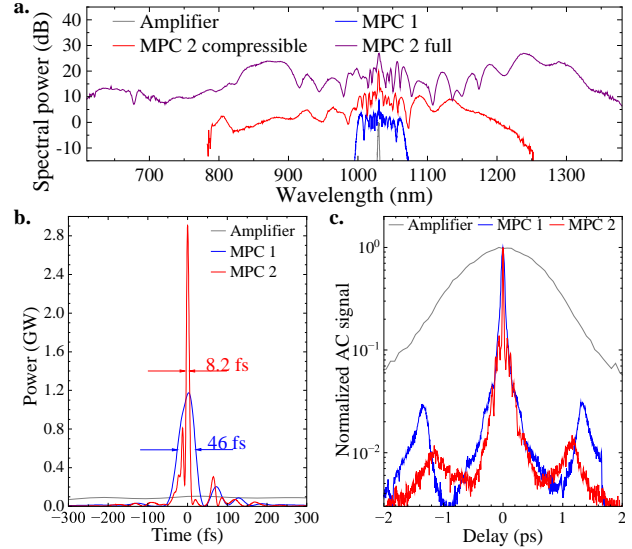


Figure 2: **a.** Ultrabroadband spectra achieved by the double-stage hybrid multi-pass multi-plate approach. Compressing the ultraviolet spectrum would require higher-order dispersion control. By compensating group delay dispersion only, the blue spectrum after MPC1 and the red spectrum after MPC2 was compressed. **b.** Time-dependent pulse profiles measured by frequency-resolved optical gating (FROG). **c.** Autocorrelations show that optical power is tightly confined to the tens of fs delay range. Adapted from [3].

the full octave-spanning mirror bandwidths were generated (Fig. 2a), potentially supporting single-cycle pulses. We had only the means to control second-order dispersion, and thus had to restrict ourselves to compress the red spectrum of Fig. 2a to 8.2 fs, i.e. the duration of 2.4 carrier cycles (Fig. 2b). A peak power of 2.8 GW was obtained. Moreover, the nonlinear method enhanced the contrast between the main pulse and the low-intensity background by almost two-orders of magnitude (Fig. 2c). The scheme can be applied to MHz-rate extreme nonlinear optics experiments. In upcoming studies, we intend to scale the peak power towards the 100 GW level.

I acknowledge DESY, a member of the Helmholtz Association HGF, for the provision of experimental facilities.

References

- [1] A.-L. Viotti *et al.*, *Optica* **9**, 197 (2022).
- [2] M. Seidel *et al.*, *Ultrafast Science* **22** 9754919.
- [3] A.-L. Viotti *et al.*, *Optics Letters* **48**, 984 (2023).

High-quality pulse compression in nonlinear multipass cells enabled by dispersion engineering

M. Karst^{*1,2}, M. Benner¹, P. Gierschke^{2,3}, H. Stark^{2,3}, and J. Limpert^{1,2,3}

¹HI Jena, Fröbelstieg 3, 07743 Jena, Germany; ²IAP, FSU Jena, Albert-Einstein-Str. 6, 07745 Jena, Germany;

³Fraunhofer Institute for Applied Optics and Precision Engineering, Albert-Einstein-Str. 7, 07745 Jena, Germany

We present a dispersion-engineered multipass cell that operates in the enhanced frequency chirping regime. By using dispersive cavity mirrors, we reshape the nonlinear interaction, resulting in a smoother, broadened spectrum and significantly improved compressed pulse quality. An Yb-laser operating at 50 kHz was compressed from 205 fs to 32 fs, with over 96% of the energy in the main pulse feature. This first experimental demonstration of enhanced frequency chirping in a multipass cell highlights the potential for dispersion-tailored pulse compression.

Gas-filled Herriott-type multipass cells (MPCs) [1] have become the driving force for the post-compression of ytterbium based laser systems. Though self-phase modulation-based pulse compression techniques inherently produce side-pulses due to spectral modulations. These side-pulses reduce the energy in the main temporal feature and decrease pulse contrast, even in transform-limited pulses. Introducing additional positive dispersion can suppress spectral modulations, reshaping the nonlinear interaction and eliminating temporal side features. This phenomenon, coined enhanced frequency chirping (EFC), was first reported in 1982 in single-mode optical fibers [2]. Applying EFC to multipass cells allows for the precise tailoring of the nonlinear and dispersive interplay.

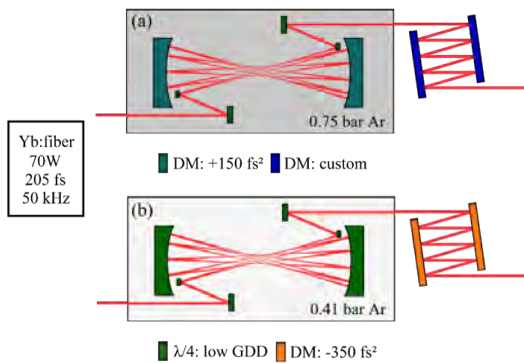


Figure 1: Schematic of the experimental setups. Configuration (a) being the EFC-MPC and configuration (b) the standard-MPC.

To achieve a clean pulse shape the dispersion of the MPC mirrors and the mirrors for recompression were numerically optimized. To compare the results of the dispersion-engineered MPC operating in the EFC regime, a second MPC was set up using standard off-the-shelf mirrors. Both cells were configured identically in a near-concentric setup

with about 1m in length. Identical laser parameters were used for both configurations, with 70 W average power at a 50 kHz repetition rate and near transform-limited 205 fs pulses from an Yb laser. Temporal characterization using the TIPTOE technique (tunneling ionization with a perturbation for time-domain observation of an electric field) revealed that the EFC-MPCs calculated transform-limited pulses contain 99% of the energy in the main feature, with retrieved traces showing 96%, compared to 93% and 88% for the standard MPC. The EFC-MPC reduced side pulse amplitude by an order of magnitude relative to the standard MPC for transform-limited pulses and by 82% for retrieved pulses. Additionally, the EFC-MPC exhibited a 5% increase in peak power compared to the standard MPC [3].

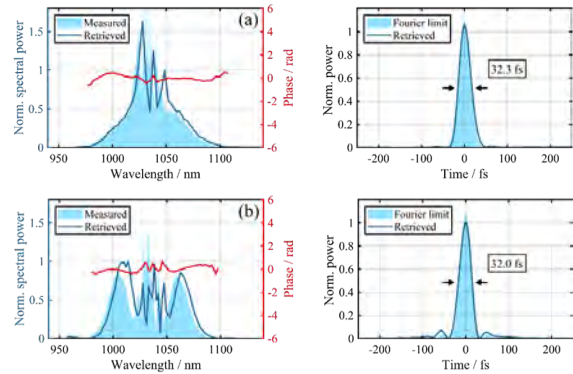


Figure 2: Temporal and spectral characterization of the compressed output pulses for the MPC configurations shown in Figure 1.

The use of dispersion engineering in MPCs enables the enhancement of pulse contrast and peak power compared to conventional MPCs. It can be implemented into the MPC design to improve system performance and is compatible with other contrast enhancement techniques. This work demonstrates the potential for dispersion-tailored pulse propagation in MPCs, with future opportunities to utilize higher-order dispersion terms and amplitude manipulation.

The authors acknowledge funding from Thüringer Aufbaubank (021VF0048); H2020 European Research Council; Fraunhofer Cluster of Excellence Advanced Photon-Source (CAPS).

References

- [1] M. Hanna *et al.*, JOSA B **34**, 1 (2017).
- [2] D. Grischkowsky *et al.*, Appl. Phys. Lett. **41**, 1 (1982).
- [3] M. Karst *et al.*, Opt. Lett. **48**, 5899 (2023).

*maximilian.karst@uni-jena.de

Microscopic Ghost Imaging in the table top XUV

Sukyoon Oh^{*1,2}, Tong Tian^{1,2}, and Christian Spielmann^{1,2}

¹Institute of Optics and Quantum Electronics, Friedrich Schiller University Jena, D-07743 Jena, Germany; ²Helmholtz Institute Jena, Fröbelstieg 3, D-07743 Jena, Germany

Ghost Imaging (GI) is a novel technique in imaging science that has garnered significant attention in recent years. Unlike traditional imaging methods, GI captures information from an object with a single sensor. In this report, we will introduce microscopic ghost imaging in the table top XUV radiation.

Motivation: Traditional microscopy is limited by the Abbe criterion. Using extreme ultraviolet (XUV) and soft X-ray (SXR) radiation (1–100 nm) can significantly improve resolution. XUV radiation, generated by high harmonic generation (HHG) with femtosecond lasers, allows for nanoscale imaging, particularly useful in material sciences and biological imaging. Conventional imaging techniques in the XUV/SXR range face limitations due to strong absorption and losses in optical components. Methods like coherent diffraction imaging (CDI) require monochromatic sources and have low photon flux and high costs [1]. GI offers a solution. Initially developed with quantum entanglement, GI now uses classical sources and computational methods, enabling lens-less imaging with low photon flux. Computational Ghost Imaging (CGI) uses single-pixel detectors and compressed sensing algorithms, making it ideal for XUV environments.

Experimental Setup: The HHG process uses an ultrafast femtosecond Ti laser system at 800 nm and 1 kHz repetition rate, focused on Argon atoms in a nickel tube. The IR beam size at focus is about 50 micro-meter, generating high harmonics with sufficient intensity. In the XUV ghost imaging setup, shown in Figure 1, the broadband XUV source passes through an XUV mask and a microscopic object to reach the XUV detector, without using any lenses or mirrors, except for a thin aluminum filter. The XUV mask, mounted on a linear stage, moves in the X-Y axis direction. GI is reconstructed based on correlations between the pattern and intensity information.

XUV Mask Design: To achieve high-quality ghost images, it is essential to select the optimal pattern, considering factors such as the number of patterns used, their pattern size, and arrangement. Depending on these characteristics, ghost images of varying qualities can be obtained. In our experiment, we chose three fundamental patterns (Differential Hadamard pattern, 4-step Fourier pattern, and Random pattern) to assess the feasibility of GI technique in the XUV domain [2].

Experimental Result: We conducted ghost imaging in the XUV range using various wafers and patterns. Figure 2 a) shows the microscopic image of the object with a 200 micrometer scale bar. The reconstructed ghost image using

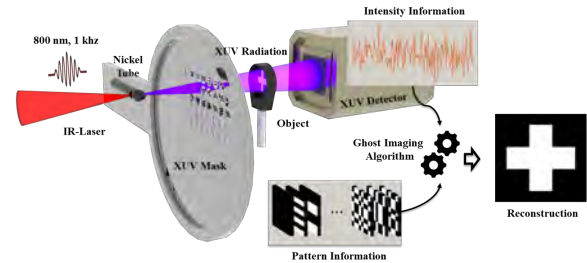


Figure 1: XUV Ghost Imaging Setup. Pulse beam with 800nm, 25fs is directed into a nickel tube filled with argon gas to generate XUV radiation via high harmonic generation. The resulting XUV beam passes through the XUV mask featuring a predefined pattern, interacts with a microscopic-sized object, and is then recorded by the detector.

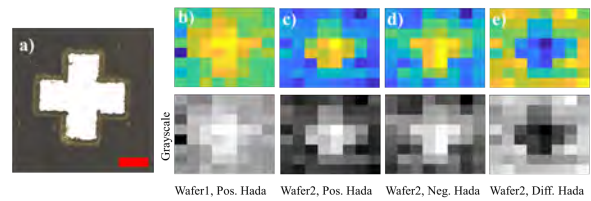


Figure 2: Ghost imaging in the XUV. a) microscopic image of the object with the scale bar corresponding to 200 micro-meter. In b), reconstructed ghost image using wafer 1 and pattern 1. Due to poor etching quality of Wafer 1, the reconstruction results are also of poor quality. Ghost image reconstruction was not feasible for pattern 2 of Wafer 1. Figures c) and d) illustrate ghost images obtained through patterns 1 and 2 on wafer 2, respectively. e) shows the reconstructed ghost imaging with differential hadamard pattern.

Wafer 1 and Pattern 1 is in Figure 2 b), which shows poor quality due to suboptimal etching. Pattern 2 of Wafer 1 did not yield feasible reconstruction. In contrast, Figures 2 c) and 2 d) display improved ghost images with Patterns 1 and 2 on Wafer 2, respectively, demonstrating better etching and pattern transfer. Figure 2 e) presents the reconstructed ghost image using a differential Hadamard pattern, which provided clearer and more defined images, effectively overcoming some limitations of the standard patterns.

References

- [1] Zürich, M *et al.*, Sci. Rep. **4**, 7356 (2014).
- [2] Gibson, G. M. *et al.*, Optics Express **28**, 28190 (2020).

* sukyoon.oh@uni-jena.de

Enhanced Ghost Imaging with Fewer Measurements

T. Tian^{*1,2}, S. Oh^{1,2}, and C. Spielmann^{1,2}

¹Institute of Optics and Quantum Electronics, Abbe Center of Photonics, Friedrich-Schiller-University Jena, Max-Wien-Platz 1, 07743, Jena, Germany; ²HI Jena, Fröbelstieg 3, 07743 Jena, Germany

In this research, an improved ghost imaging system combined flexibility and measurements-based imaging augment was proposed. This methodological enhancement has successfully doubled the contrast-to-noise ratio of the images produced and drastically reduced the root mean squared errors to 0.01, thereby affirming the potential of our approach to provide high-quality imaging with substantially fewer measurements.

Ghost imaging is an innovative technique that allows imaging with a non-spatially resolved detector, making it ideal for certain wavelength ranges where a multi-pixel camera is either unavailable or impractical [1]. Traditional ghost imaging requires a large number of measurements to reconstruct images but often suffers from low imaging quality. To address this challenge, deep learning ghost imaging (DLGI) has been proposed and extensively studied [2,3,4]. In DLGI, every pixel of the final image is associated with illumination patterns and the total intensities detected through neural networks [2]. However, DLGI solely relies on neural networks to map output images, which entails some underlying physical processes being underrepresented, leading to a lack of interpretability and generalizability.

In this study, we present a ghost imaging scheme capable of achieving imaging results comparable to DLGI [3,4], while offering clear physical interpretation, thereby providing insight into the working mechanisms of DLGI. We identified information cancellation during iterations as one of the factors contributing to the deterioration of ghost imaging quality. To mitigate this issue, we handled positive and negative measurements differently in each retrieval iteration to prevent information cancellation. Additionally, to reduce the total number of measurements, we preselected dense information-containing patterns (DICP) that offer greater benefits for final imaging. The procedures of information de-cancellation and DICP act as equivalents to neural networks in mapping final image pixels to patterns and measurements.

With the combined method, the contrast-to-noise ratios (CNR) of the final images doubled, and the root mean squared errors (RMSE) decreased to the scale of 0.01. Moreover, the required number of iterations was reduced to 10% compared to traditional ghost imaging methods employing purely random patterns. The achieved results demonstrate comparable imaging performance to DLGI, where higher imaging performance can be attained with fewer measurements [3,4].

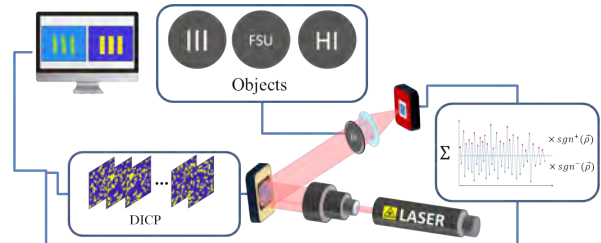


Figure 1: Experimental setup. A collimated laser is modulated by the digital micro-mirror device (DMD) loaded with DICP and recorded by the bucket detector after passing through the object. The recorded data are enhanced by proposed method.

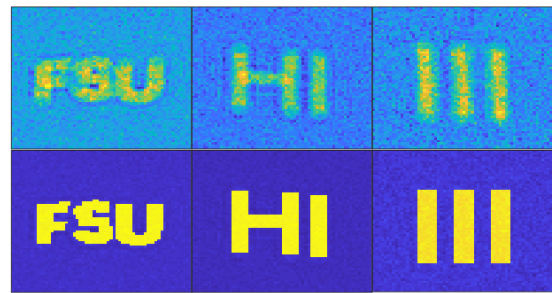


Figure 2: Final imaging results of all three objects. The upper row images are generated from selected dense information with fewer iterations. The lower row images are the enhanced results with proposed augment scheme.

In summary, the proposed scheme not only offers practical advantages in enhancing ghost imaging and portability across different wavelengths but also provides theoretical insights into DLGI's explainability.

References

- [1] A. Valencia *et al.*, Phys. Rev. Lett. **94**, 063601 (2005).
- [2] F. Wang *et al.*, Light Sci. Appl. **11**, 1 (2022).
- [3] Y. Chen *et al.*, Opt. Laser Technol. **167**, 109735 (2023).
- [4] X. Li *et al.*, Opt. Laser Technol. **168**, 109917 (2024).

*tong.tian@uni-jena.de

Broadband ptychography using curved wavefront illumination

Daniel S. Penagos Molina^{*1,2}, Lars Loetgering^{1,3}, Wilhelm Eschen^{1,2}, Jens Limpert^{1,2,4}, and Jan Rothhardt^{1,2,4}

¹HI Jena, Fröbelstieg 3, 07743 Jena, Germany; ²IAP, FSU Jena, Albert-Einstein-Straße 15, 07745 Jena, Germany;

³Carl Zeiss AG, Carl Zeiss Promenade 10, 07745 Jena, Germany; ⁴Fraunhofer IOF, Albert-Einstein-Straße 7, 07745 Jena, Germany

We examine the interplay between spectral bandwidth and illumination curvature in ptychography. By tailoring the divergence of the illumination, broader spectral bandwidths can be tolerated without requiring algorithmic modifications to the forward model. In particular, a strong wavefront curvature transitions a far-field diffraction geometry to an effectively near-field one, which is less affected by temporal coherence effects. The relaxed temporal coherence requirements allow for leveraging wider spectral bandwidths and larger illumination spots. Our findings open up new avenues towards utilizing pink and broadband beams for increased flux and throughput at both synchrotron facilities and lab-scale beamlines.

Early work in single-shot coherent diffraction imaging (CDI) suggested a trade-off between the relative spectral bandwidth $\Lambda = \Delta\lambda/\lambda_c$ and the achievable spatial resolution δ , for a given illumination beam diameter D [1]:

$$\frac{\Delta\lambda}{\lambda_c} < \frac{\delta}{D}. \quad (1)$$

In essence, an increase in spectral bandwidth translates into a loss of spatial resolution for a given beam size. However, recent work has empirically demonstrated that ptychography exhibits a higher tolerance for broadband conditions [2]. In particular, near-field ptychography configurations are more robust than far-field geometries against these decoherence effects. Nevertheless, implementing near-field geometries in the short-wavelength regime, such as XUV or X-rays, is challenging due to physical constraints that limit the minimum object-to-detector distance.

In our work, we explore how wavefront curvature can serve as an additional degree of freedom that relaxes coherence requirements. We present an intuitive explanation for the increased tolerance to broadband illumination under increasing wavefront curvature via the stationary phase approximation. Specifically, the effective region of integration in the Fresnel diffraction integral shrinks as curvature increases. This translates into an effectively smaller beam diameter in Eq. 1. In other words, larger optical path differences do not contribute to the diffraction integral, and the temporal coherence requirement is relaxed.

Our experimental results are shown in Fig. 1. Two general tendencies are observed from the reconstructed micrographs: First, the lateral resolution decreases with increasing bandwidth (left to right columns). Second, the loss

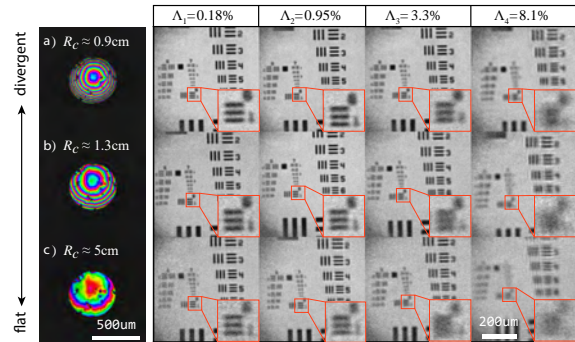


Figure 1: Comparison of ptychographic reconstructions using 3 different wavefront curvatures, each for 4 different relative bandwidths $\Lambda_i = \Delta\lambda/\lambda_c$. *Left column*, reconstructed beam profile (a-c) for variable illumination curvatures. Two general tendencies are seen from the reconstructed micrographs: (1) The lateral resolution decreases with increasing bandwidth (left to right columns). (2) The loss of lateral resolution can be compensated by increasing the wavefront curvature (bottom to top row).

of lateral resolution can be compensated by increasing the wavefront curvature (bottom to top rows). Thus, our main finding is that a larger spectral bandwidth can be tolerated when the curvature of the illumination increases. For example, comparing conditions a- Λ_3 with c- Λ_2 , we see that a comparable imaging resolution is achieved, albeit using a three times larger relative bandwidth in the former.

In essence, larger beam curvatures allow for more relaxed spectral bandwidth requirements. We believe these findings have important bearings on the achievable throughput in photon-limited ptychography experiments, including inherently broadband tabletop high-harmonic generation [3] and x-ray sources [4].

The research was supported by the Helmholtz Association (Ptychography 4.0, ZT-I-PF-4-018 (AsofXm)); Fraunhofer-Gesellschaft (Cluster of Excellence Advanced Photon Sources); Thüringer Ministerium für Bildung, Wissenschaft und Kultur (2018 FGR 0080) and the European Union (European Social Fund)

References

- [1] F. van der Veen *et al.*, *Phy: Cond. Matter* **16**, 5003 (2004).
- [2] W. Xu *et al.*, *Opt. Express* **29**, 40652 (2021).
- [3] W. Eschen *et al.*, *Light. Sci. & Appl.* **11** 117 (2022).
- [4] Y. Yao *et al.*, *J. Synchrotron Radiat.* **28**, 309 (2021).

*d.s.penagosmolina@hi-jena.gsi.de

Setup for the characterization of laser materials and first results

M. Beyer^{*1,2}, M. Hellwing¹, M. Hornung^{1,2}, G. A. Becker¹, J. Hein¹, and M.C. Kaluza^{1,2}

¹Institute of Optics and Quantum Electronics Jena, Germany; ²HI Jena, Fröbelstieg 3, 07743 Jena, Germany

We present the setup of an amplifier cavity to measure the spectral small signal gain of Yb:FP15 glass (future materials: Yb:CaF₂, Yb:LiAs) in a broad spectral range. The results will be utilised to design spectral filters to mitigate gain narrowing during the amplification process. The spectral reflection curves of the designed filters will be verified with an acousto-optic modulator (Dazzler) in the cavity for low output energies.

The experimental setup shown in Figure 1 consists of a diode pumped regenerative amplifier cavity, which can be used either with a short pulse seed laser or in Q-switched mode. The input- and output coupling of the cavity is realised using Glan-laser polarisers. They are chosen in favor of thin film plates (TFPs) because they have a high reflectivity (s-polarisation) in a broader spectral wavelength, enabling the gain measurement in a larger spectral region.

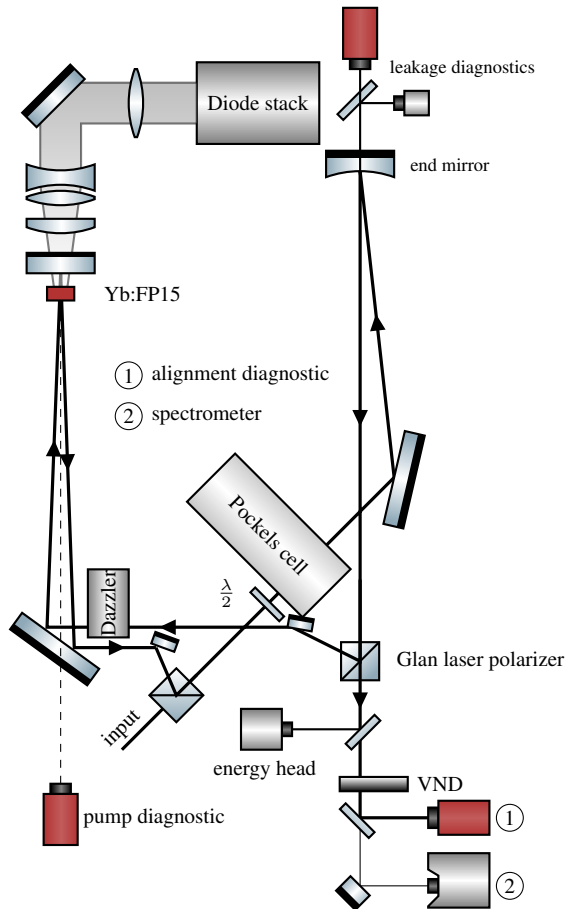


Figure 1: Experimental and diagnostic setup of the amplifier cavity.

To characterize the spectral amplification of Yb:FP15, the spectrum of a generated pulse in the regenerative amplifier with the respective laser material as a function of the Pockels cell opening time was measured. From the change in the shape of the spectrum per round trip and the separately measured pulse energy, the spectrally dependent small signal amplification $g_0(\lambda, \beta)$ can be determined for each wavelength. The obtained curve can be fitted by the small signal gain

$$g_0(\beta, \lambda) = \exp(d \cdot N_{\text{dot}}(\beta\sigma_{\text{em}}(\lambda) - (1 - \beta)\sigma_{\text{ab}})), \quad (1)$$

where $d = 1.3 \text{ mm}$ is the doubled thickness, $N_{\text{dot}} = 6 \times 10^{-20} \text{ cm}^{-3}$ the doping concentration and $\sigma_{\text{em}}, \sigma_{\text{ab}}$ the cross sections [1] of the material.

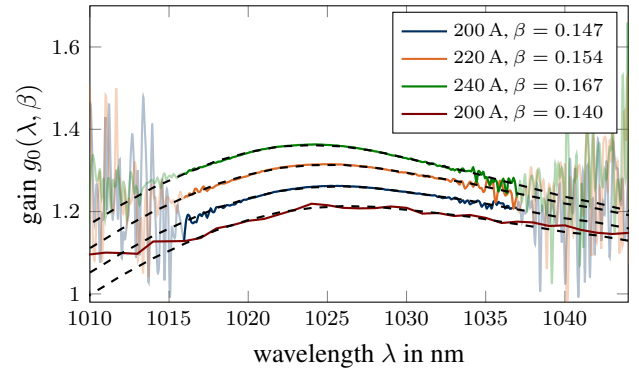


Figure 2: Gain spectrum of Yb:FP15 glass per roundtrip for different pump diode currents.

Figure 2 shows the spectral gain for Yb:FP15 glass for different pump currents of the diode stack, which was successfully obtained in a wavelength range between 1016-1037 nm. The measured gain profile corresponds well to the shape of the small signal gain calculated based on (1).

To access a larger wavelength range, the measurements were repeated by seeding the laser with a tunable, broadband, fs-laser, from which a small spectral window was selected. The gain was then measured with a photo diode (red curve). This confirmed the reliability of the gain simulation for a larger bandwidth. Therefore, the method is suitable to characterize and tailor tunable filters for other Yb:doped laser materials such as Yb:CaF₂ or Yb:LiAs.

To confirm the filter designs, an acousto-optic modulator (Dazzler) will be placed in the cavity at low energies to simulate the spectral reflectivity curves.

References

[1] T. Töpfer, Dissertation, FSU Jena Jena, 2001.

*m.beyer@uni-jena.de

LASER PARTICLE ACCELERATION

Helmholtz Laser-Plasma Metadata Initiative (HELPMI)

A. Kessler¹, M. Schwab¹, M. Kaluza¹, H.P. Schlenvoigt², F. Pöschel², A. Debus², V. Bagnoud³, U. Eisenbart³, and J. Hornung³

¹HI-Jena, Fröbelstieg 3, 07743 Jena, Germany; ²HZDR, Bautzner Landstraße 400, 01328 Dresden, Germany ; ³GSI, Plankstraße 1, 64291 Darmstadt, Germany

The HELPMI project aims at initiating a metadata (MD) standard for High-Intensity-Laser Systems (HIL) and correlated experimental data following the F.A.I.R. principles by defining a vocabulary and an ontology thereof. While for simulation data the OpenPMD standard is already well established, neither an exchange MD nor file format for experimental setups and data are available so far. With HELPMI we will close this gap and define a standard, which will be digitally hosted, machine-readable and extensible by all members of the community.

The tremendous progress enabled by HIL systems opens up new horizons in fundamental research and applications. E.g. relativistic interactions occurring in laser-driven plasmas are widely accepted as one of the most promising next-generation accelerator technologies (LPA: Laser-Plasma-Accelerator) [1]. The physical processes underlying this acceleration regime are highly non-linear and extremely complex, such that experimental creativity and adaptive studies are required to harness and exploit this technology in the future. In addition, the observations from experimental studies need to be compared against numerical simulations. Sophisticated codes based on the particle-in-cell approach are developed and used by many groups worldwide. In order to compare models and simulation results, benchmark codes and the need for common data postprocessing tools have been the motivation for the development of an open and open-source metadata standard **OpenPMD** [3].

Within the experimental community a similar metadata standard has so far not been established yet, in fact not even been defined, even though there is a broad agreement on the type of relevant data. Within HELPMI, we... consider to use **NeXus** [4] as the starting point. NeXus is a community-driven and well-established MD and file format standard for experiments in the Photon and Neutron (PaN) science community.

OpenPMD and NeXus are structured container formats with keywords, attributes and data, exhibiting structure and data upon reading, similar to an office document with embedded tables, calculations etc. Hence, it is highly likely to find schemes and workflows applicable to HIL experiments, e.g., “beams”, “geometry”, “detectors” etc. but these would still have to be transferred into the HIL context. Meta-standard means that it defines the logical layout of particle-mesh datasets in an implementation-independent manner, while allowing for domain-specific standard extensions like the existing extension for particle-in-cell codes.

We aim for a broad acceptance of the MD standard, which is of utmost importance for sustainability beyond the timeframe of this project. To identify the needs of the community, we organised a 1st workshop, which was attended by representatives of the major LPA projects as well as MD and NeXus experts.

HI-Jena has prepared the data of a typical experimental campaign in the form of a NeXus file [5]. We have demonstrated that the NeXus file format is already suitable for data exchange in its current form. To make the standard even more suitable for the LPA domain, we have created a public fork on GitHub [6]

The central part of the project is the development of a dictionary for the HIL community. We have created and published the Devices Detectors Components Library (DDC) [7]. The DDC library shall become a list containing all items and their relevant parameters in the laser-plasma laboratory that could be represented in a metadata system.

In order to automatically export the experiment data to the community format, the SCADA system Tango-Controls is currently being introduced and expanded at HI-Jena.

The authors acknowledge funding from Helmholtz Metadata Colaboration Platform.

References

- [1] <https://www.helmholtz-ard.de/>
- [2] <https://www.icuil.org/>
- [3] <https://www.openpmd.org/>, <https://zenodo.org/record/1167843>
- [4] <https://www.nexusformat.org/>
- [5] https://github.com/NeXus-for-HELPMI/POLARIS_ExpData_Example
- [6] <https://github.com/NeXus-for-HELPMI>
- [7] <https://doi.org/10.5281/zenodo.11143947>

Unified solid state-plasma kinetics modeling for ultrafast laser-solid interactions

Y. Azamoum^{*1,2}, G. A. Becker², S. Keppler^{1,2}, G. Duchateau³, S. Skupin⁴, M. Grech⁵, F. Catoire⁶, S. Hell², I. Tamer^{1,2}, M. Hornung^{1,2}, M. Hellwing², A. Kessler¹, F. Schorcht¹, and M. C. Kaluza^{1,2}

¹Helmholtz Institute Jena, Germany; ²IOQ, FSU Jena, Germany; ³CEA-CESTA, Le Barp, France; ⁴ILM, CNRS, Lyon 1 Univ., Villeurbanne, France; ⁵LULI, CNRS, CEA, Sorbonne Univ., IP Paris, France; ⁶CELIA, Bordeaux Univ.-CNRS-CEA, Talence, France

Combining a solid-state interaction model and kinetic plasma description provides unprecedented access to the interplay of fundamental processes, including initial ionization, in an ultrafast matter transition from cold solid to dense plasma, produced during the rising edge of a laser pulse irradiating a nanofoil target with intensities $\leq 10^{16}$ W/cm².

Ultrafast laser-solid interaction encompasses a multitude of physical processes while their interplay remains largely undetermined. Knowledge of the target dynamics at an early stage of the interaction is essential to applications ranging from material ablation using low-power lasers to ion acceleration employing relativistic intensity lasers. Indeed, fine-tuning of the target properties is needed to prevent the "plasma shielding" which diminishes the ablation efficiency [1] or to optimize accelerated ion beams which require a specific target state during the laser rising edge [2], before the arrival of pulse peak. In this work, the sub-picosecond target transition from cold solid to dense and expanding plasma is first evidenced with a single-shot near infrared (NIR) probing technique employing a chirped laser pulse as a probe in transmission. The probe pulse illuminates longitudinally a 10 nm-thick Diamond-like carbon (DLC) foil interacting with an ultrashort laser pulse with peak intensity of $\sim 10^{16}$ W/cm², exhibiting an exponential-like rising edge [3]. Figure 1 shows that the measured probe transmission $T(t)$ is better described using a two-step model (TSI), starting with an extended solid-state interaction (SSI) model and followed, after the DLC melting point, by a plasma kinetic description (particle-in-cell – PIC). Indeed, the transmission obtained from PIC alone (dashed line) starting from a cold DLC foil drops much faster than in experiment with $\tau_{\text{PIC}} (\sim 50 \text{ fs}) \ll \tau_{\text{exp}} (\sim 600 \text{ fs})$, where τ is the time required for the transmission to drop from 90 % to 10 %. No meaningful τ could be extracted using the SSI model alone, because the full transmission dynamics could not be described (red triangles). However, when combining the extended SSI model and PIC, the TSI shows good agreement with the experiment ($\tau_{\text{TSI}} (\sim 800 \text{ fs}) \sim \tau_{\text{exp}}$). The SSI model, which was originally developed for dielectric materials, was extended to higher densities (blue line) for semiconductors like DLC. The extended SSI domain (red-shaded region) in Figure 1, shows an excellent agreement with experiment, validating the application of the SSI model to lower band

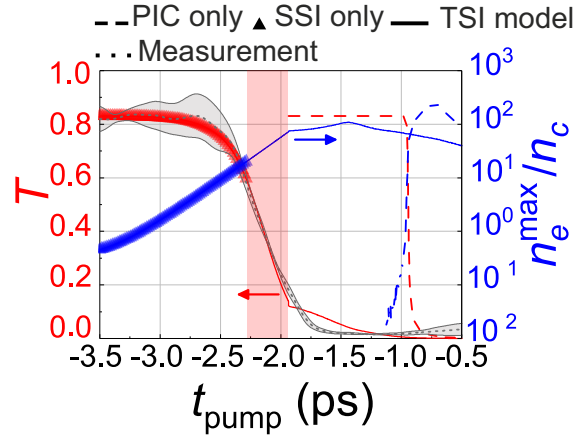


Figure 1: Measured (dotted line) and computed probe transmission (red) through the target (in the high intensity region) during the laser rising edge ($t_{\text{pump}} = 0$ ps is the peak arrival time). The standard deviation over several measurements is given in the gray-shaded region. Dashed, triangles and solid lines are from PIC, SSI and TSI models, respectively. n_e^{max} (blue) are the corresponding maximum electron densities, n_c being the critical density at $\lambda_{\text{probe}} = 800 \text{ nm}$ [3].

gap materials. Although neither SSI nor PIC alone could explain the measurements, they are, however, complementary, as each of them includes necessary fundamental processes to describe an ultrafast laser-solid interaction. On the one hand, the initial stage of the interaction, i.e., ionization of a solid, can only be accurately described using the SSI model whereas the highly overdense and expanding plasma including inner shell ionization can only be described by a PIC code. Finally, our method can be extended to thicker foils that exhibit high initial transmission, such as dielectrics. In this case, the TSI model must be modified accordingly to consider the target inhomogeneity during the interaction. Such a modified TSI model could also be used to describe the ionization and plasma dynamics of thick nontransparent targets, where the initial plasma is produced on the front surface only.

References

- [1] S. Dittrich *et al.*, *Opto-Electron. Adv.* **4**, 200072 (2021).
- [2] M. Rehwald *et al.*, *Nat. Commun.* **14**, 4009 (2023).
- [3] Y. Azamoum *et al.*, *Light Sci. Appl.* **13**, 109 (2024).

* yasmina.azamoum@uni-jena.de

Development of ultrafast burst shot shadowgraphy for plasma diagnostics

Y. Zhao^{*1,2}, X. Huang¹, A. Sävert^{1,2}, and M. C. Kaluza^{1,2}

¹HI Jena, Fröbelstieg 3, 07743 Jena, Germany; ²IOQ, FSU Jena

Few-femtosecond microscopic shadowgraphy is commonly used in investigating laser-plasma interactions and successfully yields good results. However, the snapshot property of this technique, coupled with the shot-to-shot fluctuations of the high-power laser system, restricts our understanding of the transient features in laser-plasma interactions. In this study, we successfully extend the ultrafast microscopic shadowgraphy into burst mode, allowing us to take 4 frames in a ~ 200 fs time window from one single interaction, with a spatial resolution better than $2 \mu\text{m}$ and a temporal resolution approximately 10 fs.

Few-cycle femtosecond optical probes and microscopic shadowgraphy have been successfully used to take snapshots from laser-plasma interactions, reaching femtosecond time and micrometer space resolution [1]. A set of snapshots at different time delays is usually required to fully understand the laser-plasma interaction process. However, the shot-to-shot fluctuations of high-power laser systems are not negligible. Therefore, a burst shot imaging technique is desired. Few-cycle probe pulses have broad spectral bandwidth. That allows us to extend the ultrafast snapshot technique into a burst mode by adding linear chirp into femtosecond probes.

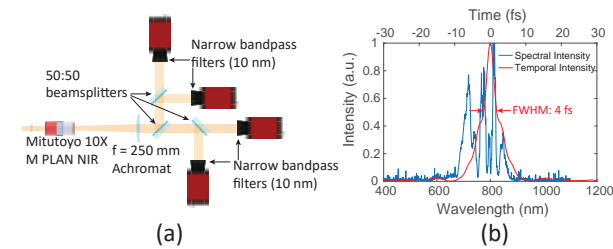


Figure 1: (a) Schematics of the microscopic burst shot imaging setup. (b) Typical probe spectrum and its Fourier transform limit.

In this study, we developed a burst shot microscopic shadowgraphy technique based on sequentially timed all-optical mapping photography (STAMP) [2]. The probe pulse with a bandwidth limited pulse duration of 4 fs was generated via the same method in ref. [1]. A 12 mm fused silica was placed into the probe beam path, resulting in a ~ 300 fs (FWHM) linearly chirped pulse. After the probe pulse propagated through an underdense plasma, it was imaged by the setup shown in Fig. 1. Since the probe pulse was linearly chirped, the temporal resolution of the shadowgrams can be recovered by spectral filtering. Applying a

10 nm bandpass filter with a center wavelength at 800 nm results in a temporal resolution of approximately 10 fs. The spatial resolution test results are given in Fig. 2(a), which show a spatial resolution better than $2 \mu\text{m}$ and close to the diffraction limit. This imaging setup was used to take burst-shot shadowgrams of laser wakefields in an experiment at JETi200. In this experiment, a 22 fs main laser pulse ($\lambda_0 = 800$ nm) with 2.6 J energy was focused by a $f/20$ parabola into a helium gas target. Wakefields were generated inside the plasma with a density around $8 \times 10^{18} \text{cm}^{-3}$. An example of experimental shadowgrams is shown in Fig. 2(b). In these figures, the bubble of the laser wakefield traveled from the left to the right close to the speed of light. The fine structures of the wakefields on the shadowgrams show the temporal resolution of the imaging system is preserved.

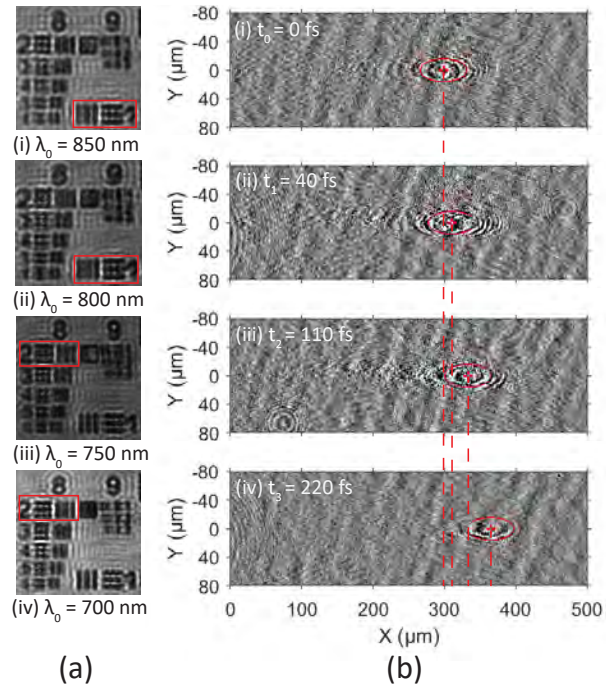


Figure 2: (a) Spatial resolution tests using 10 nm bandpass filters. λ_0 are the center wavelengths of the bandpass filters. (b) Multi-color shadowgrams from a single shot. The time delays relative to the first frame are given in each figure.

References

- [1] M. B. Schwab et al., Applied Physics Letters **103**, 191118 (2013).
- [2] K. Nakagawa et al., Nature Photonics **8**, 695 (2014).

*yu.zhao@uni-jena.de

All-optical measurements of LWFA electron beam source size and emittance

F. C. Salgado^{*1,2}, A. Kozan^{1,2}, D. Seipt^{1,2}, D. Hollatz^{1,2}, P. Hilz^{1,2}, M. Kaluza^{1,2}, A. Sävert^{1,2}, A. Seidel^{1,2}, D. Ullmann^{1,2}, Y. Zhao^{1,2}, and M. Zepf^{1,2}

¹HI Jena, Fröbelstieg 3, 07743 Jena, Germany; ²IOQ, Friedrich-Schiller-Universität Jena, Germany

Novel schemes for generating ultra-low emittance electron beams have been developed in past years and promise compact particle sources with excellent beam quality suitable for future high-energy physics experiments and free-electron lasers. Here we report on a the experimental demonstration of a novel all-optical technique capable to resolve ultra-low beam emittances [1]. Calculations show that tight bounds on the upper limit for emittance and source size can be derived from this ‘laser-grating’ method [2] even in the presence of low signal to noise and uncertainty in laser-grating parameters. In the experiment, the inferred source size and geometric emittance were $(1.7 \pm 0.2) \mu\text{m}$ and $(4.4 \pm 0.9) \times 10^{-3} \pi \text{ mm mrad}$, respectively.

The quality of a particle beam, such as their high brightness and coherence, can be directly linked to the beam’s transverse geometric emittance, $\epsilon_{\text{rms}} = \sigma_x \sigma_{x'} (1 - \rho)$ as a measure of the phase-space volume, where σ_x denotes the rms beam waist (source size), $\sigma_{x'}$ is the rms beam divergence, and ρ is their correlation. While $\sigma_{x'}$ is easily measured, σ_x requires some more effort. We assume the beams to be uncorrelated, $\rho = 0$.

The all-optical method to infer σ_x , first proposed in Ref. [2] and experimentally demonstrated in [1] works as follows: The electron beam is interacting with a laser grating at a certain distance after the end of the LWFA accelerator. The ponderomotive potential of the laser grating modulates locally the momentum spectrum of the tilted transverse phase space ellipse. After some further propagation this momentum space modulation is transferred into an electron density modulation which can be imaged on a scintillating screen (see Fig. 1a).

The modulation depth, quantified via the peak-to-valley ratio, depends on the source size. Hence, measuring the former allows to infer the latter. The inference requires precise knowledge of the laser grating parameters such as its period λ_G and grating strength $\kappa = \mathcal{I}/\mathcal{I}_0$, where \mathcal{I} is the grating intensity and \mathcal{I}_0 represents optimum intensity in the limit $\sigma_x \rightarrow 0$. Theoretical analysis shows that $\kappa \approx 2$ produces the maximum modulation depth for expected source sizes of LWFA beams. Thus, by using $\kappa = 2$ for the inference we can easily obtain an upper limit of σ_x .

In the experiment, the electron beam had a charge of $(5.6 \pm 0.7) \text{ pC}$ per bunch, a divergence of $\sigma_{x'} = (2.6 \pm 0.4) \text{ mrad}$, and an average energy of 73 MeV with an energy spread of $(27.3 \pm 4.8)\%$. These electrons were modulated using a laser grating with a period of $\lambda_G =$

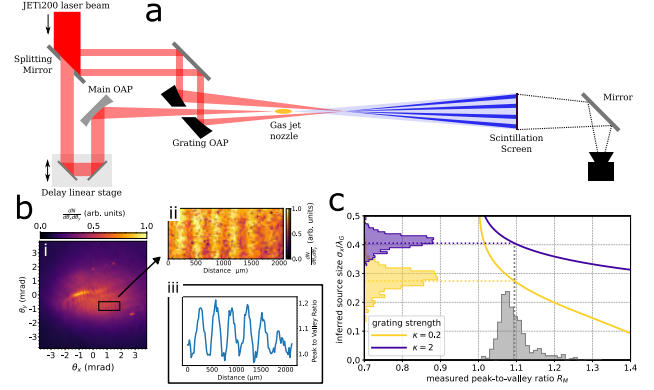


Figure 1: a) Experimental layout for laser interference method, where the central part of the JETi beam (red) accelerates electrons (blue) in a gas jet. The laser grating modulating the electrons is generated by focusing the outer ring of the laser approximately 34.4 mm downstream of the gas jet nozzle. b) The modulated electron beam due to the interaction with the interference fringes of the ring laser beam at the focus imaged with a YAG:Ce scintillation screen (i,ii), and integrated peak-to-valley ratio modulation (iii). c) The distribution of measured peak-to-valley ratios of 184 shots (grey histogram on bottom axis) allows to infer electron beam source size σ_x distributions at different grating strengths κ (histograms on left axis), given here for the absolute upper limit at $\kappa = 2$ (purple) and a grating strength of $\kappa = 0.2$ (yellow).

$(4.2 \pm 0.2) \mu\text{m}$ and $\kappa \approx 0.2$. Fig. 1b displayed the modulated electron beam recorded on a scintillating screen.

By analyzing the peak-to-valley ratio distribution from 184 shots of the modulated electron signal as shown in Fig. 1c, and assuming $\kappa = 2$ we infer the quoted upper limits for source size and emittance. For this experiment, the inferred σ_x is remarkably insensitive to the specific value of κ (see Fig. 1c, yellow vs. purple).

In summary, our experiment [1] demonstrated the feasibility and potential of the all-optical laser grating method for measuring the emittance of LWFA electron beams.

This research was funded by BMBF (Project No. 05K19SJA), DFG Research Unit FOR2783 (Project No. 416708866), and TAB (Contract No. 2019 FGI 0013).

References

- [1] F. C. Salgado *et al.*, Phys. Rev. AB **27**, 052803 (2024).
- [2] A. Seidel *et al.*, Phys. Rev. Accel. Beams **24**, 012803 (2021).

*felipe.salgado@uni-jena.de

Preparations and target fabrication for investigating the peeler scheme at JETi200

I. Salaheldin^{*1}, L. Reichwein², P. Hilz¹, and M. Zepf¹

¹Helmholtz Institute Jena, 07743 Jena; ²Heinrich Heine University Düsseldorf, 40225 Düsseldorf

This project aims to apply the peeler scheme to accelerate protons from CH foils. The target is oriented longitudinally along the laser propagation direction. The laser pulse interacts with the target's front edge, peeling electrons and driving them forward. These electrons then pull out and accelerate protons at the rear edge. In preparation, the targetry process has commenced, and preliminary 3D-PIC simulations have been conducted to assess the feasibility of using the available femtosecond TW laser for this scheme.

Surface plasma waves (SPWs) are generated at the surface-vacuum interface when a laser pulse interacts with the sharp edge of an overdense plasma surface. An overdense plasma, characterized by a plasma frequency ω_p significantly greater than the laser frequency ω_L , can be achieved during this interaction. For solid CH targets, typically $n_e \approx 10^2 n_c$, where n_c is the critical density. Within the scale length $L \gg \lambda_L$, where $\lambda_L = 2\pi c/\omega_L$, the target maintains a sharp density gradient, which is crucial for the excitation of the SPWs [1].

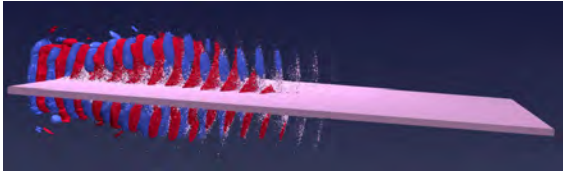


Figure 1: The Peeler acceleration scheme, where a laser pulse hits the front edge of the target (on the left) and propagates along the surfaces of the target in x -direction.

These SPWs serve as the accelerating field for electrons along the surface of the target [1]. Under appropriate resonance conditions, SPWs efficiently are coupled with the incident electron magnetic wave (EMW). This coupling facilitates the transfer of energy from the EMW to the electrons via the SPWs, thereby maintaining the forward electron acceleration along the target surface. The resonance condition is maintained along the dephasing length $L_d = \frac{\lambda}{\lambda^2/\pi^2 w_0^2 + \omega_L^2/\omega_p^2}$ [2]. Once the electrons reach the other edge of the target, they are expelled into the vacuum, leaving behind the relatively heavier protons. This charge separation induces the generation of a static electric field at the target rear edge, which in turn pulls the protons and accelerates them in the forward direction.

An experiment for this scheme is intended to be performed with JETi200 laser at the Helmholtz Institute-Jena, which has $\lambda = 800$ nm, with 2 J on target and a pulse

duration of 25 fs. An off-axis parabola $f/1.5$ is used to focus the beam into $1.8\mu\text{m}$ (FWHM), providing a peak intensity of $3 \times 10^{21} \text{W}/\text{cm}^2$. Using the mentioned parameters, the dephasing length for this case is then calculated to be $L_d = 28.5 \mu\text{m}$.

From an experimental perspective, the generation of SPWs relies on several critical parameters, including the alignment of the target's front edge at the focal plane and maintaining a normal incidence angle of the laser. However, the primary challenge is achieving the ideal target geometry required for peeler acceleration. Fig. 2 presents a prototype bridge-target made of silicon nitride (SiN_x), supported by a bow tie-shaped holder composed of silicon (Si). The bridge has a length of $L = 20 \mu\text{m}$ in the direction of laser propagation and a thickness of 500 nm. Additionally, all surfaces of the bridge are covered with a 50 nm thick layer of perylene, which serves as a proton source for acceleration.

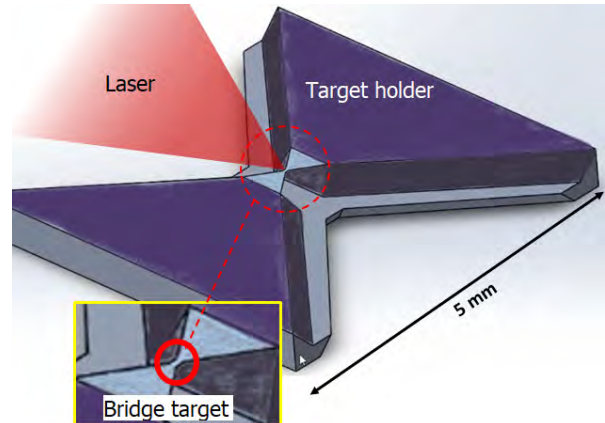


Figure 2: Target prototype intended for the peeler acceleration, with $20 \mu\text{m}$ in laser propagation direction (x), 500 nm thick (y), and $> 50 \mu\text{m}$ in (z).

3D-PIC simulations were conducted implementing the JETi200 laser parameters to obtain preliminary insights and estimations for the upcoming experiments. These simulations yielded protons with energies up to 35 MeV in the laser forward direction. With the planning complete, the next step is to acquire the fabricated targets and conduct the initial experimental run to validate the peeler acceleration concept.

References

- [1] A. Macchi, Phys. Plasmas **25**, 031906 (2018).
- [2] X. F. Shen *et al.*, Phys. Rev. X **11**, 041002 (2021).

* i.salaheldin@gsi.de

Limitations of Emittance Measurement Using Pepper Pot Method

A. Kozan^{*1,2}, F. Salgado^{1,2}, D. Seipt^{1,2}, D. Hollatz^{1,2}, P. Hiltz^{1,2}, M. Kaluza^{1,2}, A. Sävert^{1,2}, A. Seidel^{1,2}, D. Ullmann^{1,2}, Y. Zhao^{1,2}, and M. Zepf^{1,2}

¹HI Jena, Fröbelstieg 3, 07743 Jena, Germany; ²IOQ, FSU Jena

The pepper pot method is a well-known method for transverse emittance diagnostics for conventional accelerators, where the source size is relatively large. In this work, we test the suitability of the method for laser wakefield accelerated (LWFA) electron beams where the source size is constrained by the bubble size. Using GEANT4 Monte Carlo simulations [1], we report that for small source sizes ($\sigma_0 < 5 \mu\text{m}$), corresponding to ultra-low emittance achievable from LWFA sources, the pepper pot method can no longer resolve the emittance.

Emittance characterization is important for the performance of free-electron lasers (FELs) and collider experiments due to beam brightness conditions and luminosity estimation. One of the conventional single-shot methods is so called pepper pot method. The method is based on the principle of sampling the particle beam with a high-Z material mask consisting 2D array of holes, therefore allowing one to infer emittance using accepted electrons which are often called beamlets.

To understand the limitations of the method in resolving small emittances, set of GEANT4 simulations were designed. The simulation parameters and geometry were selected based on the experiment conducted in JETi200 laser.

For these simulations, a total of 3×10^6 electrons were generated from the source. The energy spectrum of the beam was characterized by a Gaussian distribution, with a mean energy of 72 MeV and an root mean square (rms) spread of $\sigma_E = 50$ MeV. Additionally, the rms divergence (θ_{rms}) of the beam was set to 1.85 mrad. The pepper pot mask was located 181 mm downstream of the source, 1269 mm before the screen. The mask had a fixed 200 μm thickness, yet the hole diameter was varied for different runs of the simulation. While the electron beam properties remained fixed, the input rms emittance (ϵ_{rms}) was varied using the relation

$$\epsilon_{rms} = \theta_{rms} \cdot \sigma_0, \quad (1)$$

by modifying the beam source size (σ_0) from 1 to 39 μm .

After each simulation run, the beamlets were recorded on the screen and used to calculate the emittance using the formula given by [2]. For different mask hole diameters, a deconvolution term was added as described in the [3] to suppress the hole size contribution on computation. Consequently, the inferred rms emittance using the pepper pot method was plotted against the input rms emittance as shown in the Fig.1.

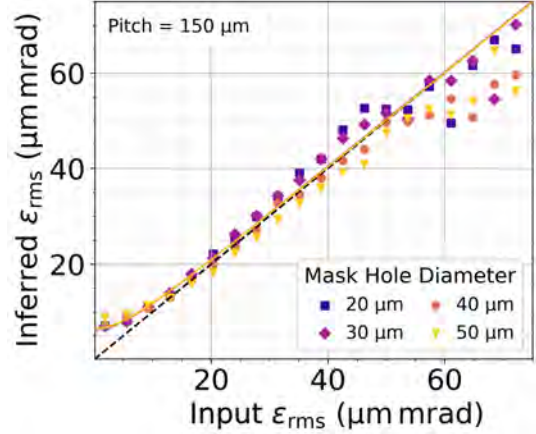


Figure 1: Inferred vs input emittance resulting from 1 to 39 μm σ_0 scan. Masks had 150 μm pitch distance between the holes, and hole diameters varied from 20 to 50 μm . Best fitting had the form of $\epsilon_{rms}^2 = \alpha^2 + \theta_{rms}^2 \sigma_0^2$ with an offset term α .

In Fig.1, the inferred emittance for $\epsilon_{rms} > 40 \mu\text{m mrad}$ ($\sigma_0 > 21 \mu\text{m}$) is deviating from the trend. This is due to the large σ_0 resulting in beamlets overlapping on the screen. As a result, isolation and fitting of individual beamlets gets challenging, leading to an ill-posed result. This gives a design point constraint where the geometrical magnification or the pepper pot geometry (in particular the pitch distance between the holes) should be selected accordingly to avoid any overlapping of the beamlets on the screen for reliable analysis.

In the lower emittance region, where $\epsilon_{rms} < 10 \mu\text{m mrad}$ ($\sigma_0 \leq 5 \mu\text{m}$), the inferred emittance converges to an offset value, indicating that the method is unresponsive to the σ_0 scan. At this small values, the beamlets have a very narrow angular spread, disabling to determine divergence of the beamlets on the screen and hence the emittance.

In conclusion, when the σ_0 is much smaller than the hole diameter of the mask, the pepper pot method overestimates the transverse emittance and this constitutes a limitation of the method for ultra-low emittance characterization.

This research was funded by the Federal Ministry of Education and Research of Germany (BMBF) in the Verbundforschungsframework (Project No. 05K19SJA).

References

- [1] S. Agostinelli *et al.*, NIM-A, **506** (2003).
- [2] M. Zhang, Fermilab-TM-1988, (1996).
- [3] C. M. S. Sears *et al.*, Phys. Rev. ST Accel. Beams **13** (2010).

* a.kozan@hi-jena.gsi.de

Enhanced Laser-Driven Electron and Ion Acceleration Using Near-Critical Density Plasma CNF Targets

P. Tavana^{*1}, M. Gyrdymov², O.N. Rosmej³, and C. Spielmann^{1,4}

¹Institute of Optics and Quantum Electronics, Abbe Center of Photonics, Friedrich-Schiller-University Jena, Max-Wien-Platz 1, 07743, Jena, Germany; ²Goethe University, Frankfurt, Max-von-Laue-Straße 1, 60438 Frankfurt am Main, Germany; ³GSI, Planckstraße 1, 64291 Darmstadt, Germany; ⁴HI Jena, Fröbelstieg 3, 07743 Jena, Germany

We present preliminary results demonstrating the acceleration of direct laser accelerated (DLA) electrons and protons from laser-irradiated long-scale carbon nanotube foams (CNF) at moderate relativistic intensities. These results indicate significantly improved particle acceleration compared to conventional metallic foils.

The experiment was conducted with PHELIX (Petawatt High-Energy Laser for Heavy Ion EXperiments) at GSI Helmholtzzentrum für Schwerionenforschung. The laser pulse of 0.65 ps duration was focused with an $f/5$ off-axis parabolic mirror in a focal spot of $(12 \pm 2) \mu\text{m}$ (FWHM) containing 20 J laser energy. This resulted in a moderate relativistic intensity of $10^{19} \text{ W cm}^{-2}$ in vacuum.

As targets we have used near-critical density CNFs of 1.5 mg cm^{-3} to 3.5 mg cm^{-3} on $10 \mu\text{m}$ gold foil. CNF is made of bundles of carbon nanotubes with diameters ranging from 5 nm to 10 nm (smaller than the laser's skin depth) and lengths between $5 \mu\text{m}$ to $50 \mu\text{m}$, which are randomly arranged, forming a three-dimensional stochastic network [1].

The spectra of electrons were measured using a 1 T magnetic spectrometer with imaging plates as detectors positioned at -10° to the laser axis (Figure 1). The use of CNFs resulted in a significant increase in both the effective temperature and the number of accelerated electrons (blue spectrum) compared to shots on ordinary thin metallic foils (gray spectrum) at high contrast. Specifically, with CNF targets, the maximum measured energy of electrons reached up to 50 MeV, which is five times higher than the energy observed in shots on $15 \mu\text{m}$ copper foil. The effective electron temperature reached 10 MeV by CNF targets, compared to just 1.2 MeV for a shot on copper foil. Additionally, we conducted some shots with pre-ionized CNF targets by applying a delicate ns pulse, which resulted in an enhancement in both the electron energy and the effective temperature of DLA electrons. The underlying efficient electron acceleration mechanism in the CNF targets is direct laser acceleration. This process involves the propagation of the laser through near-critical density plasma, leading to the formation of a relativistic plasma channel. Within this channel, electrons experience betatron oscillations in quasi-static electric and magnetic fields. As the betatron frequency resonates with the Doppler-shifted laser frequency, electrons gradually gain energy from the laser

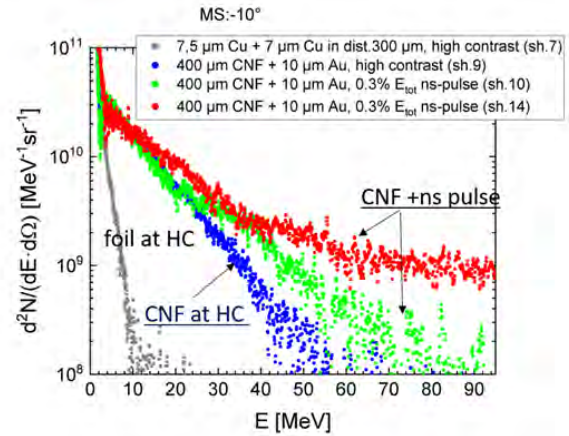


Figure 1: Electron spectra obtained from high contrast shot on $15 \mu\text{m}$ Cu, high contrast shot on $400 \mu\text{m}$ CNF+ $10 \mu\text{m}$ Au and shot on $400 \mu\text{m}$ CNF+ $10 \mu\text{m}$ Au pre ionized.

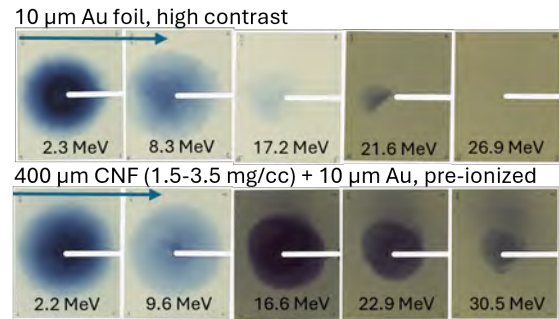


Figure 2: Proton signals on Radiochromic film: Above, a shot on $10 \mu\text{m}$ Au with high contrast; below, a shot on CNF + $10 \mu\text{m}$ Au substrate pre-ionized with ns pulse.

field [2].

The proton signals, measured using radiochromic film, indicated a higher cut-off energy and a notably round, smooth beam with a higher number of protons for shots on pre-ionized CNF targets compared to shots on conventional foils, as depicted in Figure 2. The underlying mechanism contributing to this effect requires further investigation through numerical simulations.

References

- [1] W. Ma *et al.*, Nano Lett. **7**, 2307 (2007).
- [2] A. Pukhov *et al.*, Rep. Prog. Phys. **66**, 4772 (2003).

* p.tavana@uni-jena.de

Nanosecond Lifetime Hot and Dense Plasmas from Relativistic Laser-Nanowire Interaction

E. Eftekhari-Zadeh ^{*1,2}, M. Gyrdymov^{3,4}, P. Tavana^{1,3,4}, R. Loetzsch^{1,2}, I. Uschmann^{1,2}, T. Siefke⁵, T. Käsebieber⁵, U. Zeitner⁵, A. Szeghalmi⁵, D. Serebryakov⁶, E. Nerush⁶, I. Kostyukov⁶, O. Rosmej^{3,4}, D. Kartashov¹, and C. Spielmann^{1,2}

¹IOQ, Friedrich Schiller University Jena; ²HI Jena, Fröbelstieg 3, 07743 Jena; ³GSI, Planckstr. 1, Darmstadt, Germany; ⁴IAP, Goethe University Frankfurt am Main; ⁵IAP, Friedrich Schiller University Jena; ⁶IAP RAS, Nizhny Novgorod, Russia

We have experimentally observed jet-like plasma structures emitting He-like Ti ion radiation on nanosecond time scale when nanowire arrays are irradiated by relativistically intense, ultra-high contrast femtosecond laser pulses. These observations suggest existence of a hot (0.5-1 keV) and dense plasma ($\sim 10^{21} \text{cm}^{-3}$) on nanosecond time scale.

In the experiments, a periodic array of composite nanowires (NW) with a 100 nm Si core and 25 nm TiO cladding and 400 nm period, grown on a 50 μm Si membrane, was irradiated by ultra-high temporal contrast, 40 fs, 0.4 μm wavelength laser pulses with the peak intensity up to $\geq 3 \times 10^{19} \text{W/cm}^2$ ($a_0 \sim 3$). As a reference flat target, a 25 nm TiO film, deposited on the same 50 μm Si membrane, was used. An imaging spectrometer based on the toroidal GaAs crystal was employed to measure the line emission of Ti ions up to H-like Ti^{+21} charge state and for 1D imaging of the emission source. We observe that the source of the emission of He-like Ti^{+20} ions from nanowire arrays consists of an intense spot at the target surface and 200 times less intense, 1 mm long, jet-like region extended from the surface. Estimates based on the ion expansion in the plasma suggest that this length scale corresponds to several nanosecond emission time [1].

To get insight into the plasma parameters that would result in formation and emission of He-like Ti ions, we carried out 3D PIC simulations of relativistic interaction of laser pulses with nanowire array and the reference flat target. The time dependent plasma density and temperature, retrieved from the simulations, were used to simulate the emission of He-like w-line, employing radiative collisional kinetic code FLYCHK. Our simulations predict that the intense He-like emission at the target surface is emitted within < 1 ps time after the laser pulse arrival on the target. Using the experimentally measured intensity ratio between the He-like emission on the surface and in the "jet", and including the factor 10^3 accounting the difference in the emission duration, we use FLYCHK simulations to determine the plasma parameters in the "jet". The results are shown in Figure 1 by the white contour line. The simulations suggest that near solid density ($\sim 10^{21} \text{cm}^{-3}$) and about 0.5-1 keV temperature plasma is required to generate the He-like emission observed in the experiments.

To understand the physical mechanisms that would re-

sult in formation of such long living hot and dense plasma, we carried out the 3D PIC simulations of plasma dynamics on the time scale up to 2 ps after the laser pulse. Figure 2 shows the spatial structure of the magnetic field, formed in the plasma shortly after the interaction with the laser pulse. We observe formation of the global magnetic field in the plasma volume for the nanowire arrays (Fig.2(b)) that is absent for the flat target (Fig.2(a)). Simulations on longer time scale suggest that such structure of the magnetic field results in anisotropic plasma expansion that might lead to enhancement in the development of Weibel-like instabilities and generation of magnetic fields that would be capable to keep hot and dense plasma on nanosecond time scale.

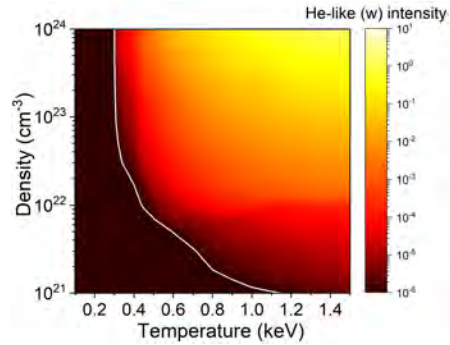


Figure 1: Intensity of He-like (w) line of Ti^{+20} as a function of plasma density and temperature.

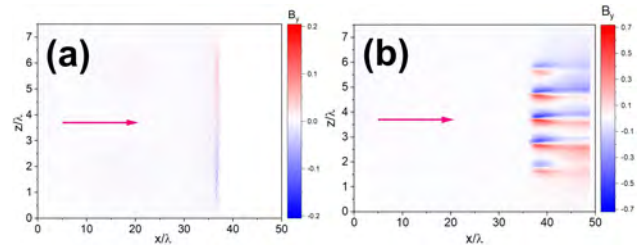


Figure 2: B-field pattern of flat (a) and NWs(b) generated shortly after the interaction with the laser pulse. The arrow shows pulse propagation direction.

References

- [1] E. Eftekhari-Zadeh *et al.*, Compact EUV & X-ray Light Sources. Optica Publishing Group, JTh6A.1 (2022).

* e.eftekhari-zadeh@uni-jena.de

PHOTON AND PARTICLE SPECTROSCOPY

Enabling quantum technologies for the next level of precision

P. Micke*^{1,2,3}

¹HI Jena, Fröbelstieg 3, 07743 Jena, Germany; ²IOQ, University of Jena, Max-Wien-Platz 1, 07743 Jena, Germany;

³GSI Darmstadt, Planckstraße 1, 64291 Darmstadt, Germany

Optical atomic clocks reach record accuracies. Heavy ions in their highest charge states however are not used in those instruments yet. The reason is that they do not have suitable transitions for detecting quantum jumps on the clock transition and that clocks typically lack a source for these exotic atomic species. A new Helmholtz Young Investigator Group has been established at the HI Jena to overcome these obstacles and to free up the excellent sensitivities of heavy highly charged ions for tests of fundamental physics in combination with a precision level that is only known from optical atomic clocks.

In August 2023 the Helmholtz Young Investigator Group (HYIG) led by Peter Micke has been established at the Helmholtz Institute Jena with the goal to set up a universal laser spectroscopy platform in a new state-of-the-art laser laboratory downstream the HITRAP facility at the GSI Helmholtz Center for Heavy Ion Research. This platform is based on the versatile method which is known as quantum logic spectroscopy [1, 2]

Prospectively, heavy highly charged ions (HHCI) of the experimenter's choice can be produced by the accelerator complex of GSI, slowed down by the HITRAP decelerator, and re-captured in a precision-fabricated new cryogenic Paul trap that is located inside the new laser laboratory. There, they co-crystallize within a laser-cooled Coulomb crystal of beryllium ions [3] which not only allow for sympathetic cooling but also provide a high-fidelity detection mechanism. Next, a two-ion crystal composed of one HHCI and one Be^+ ion is prepared, cooled to the quantum-mechanical ground state of motion [4], and probed by a highly stable clock laser to excite the optical clock transition of the HHCI in question. Two red-sideband laser pulses subsequently swap the quantum states of internal and motional degrees of freedom to map the initial clock state onto the Be^+ hyperfine qubit. Eventually, this qubit is read out with a final detection laser pulse.

With this technique, optical ground-state hyperfine-structure splittings of HHCI such as hydrogen-like or lithium-like ions can be measured at an accuracy level that is only in the realm of optical atomic clocks [5]. At the same time HHCI offer excellent sensitivities for tests of fundamental physics and searches for physics beyond the Standard Model of particle physics [6, 7] with a high discovery potential in combination with the cutting-edge accuracy levels that can be achieved. Currently, the construction of the quantum-logic laser laboratory is well-advanced and the HYIG focuses with the group leader and two PhD

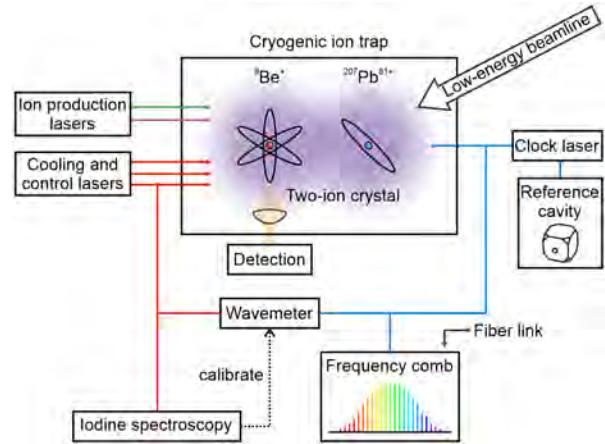


Figure 1: Concept of the new laser spectroscopy platform that is based on quantum logic spectroscopy.

students on a rapid development of the experimental setup, supported by scientists of the HI Jena as well as the atomic physics and the decelerator operation departments of GSI.

The author acknowledges funding from the Initiative and Networking Fund (IVF) of the Helmholtz Association.

References

- [1] P. O. Schmidt *et al.*, Science **309**, 749 (2005).
- [2] P. Micke, T. Leopold, S. A. King *et al.*, Nature **578**, 60 (2020).
- [3] L. Schmöger *et al.*, Science **347**, 1233 (2015).
- [4] S. A. King *et al.*, Phys. Rev. X **11**, 041049 (2021).
- [5] S. A. King *et al.*, Nature **611**, 7934 (2022).
- [6] M. S. Safronova *et al.* Rev. Mod. Phys. **90**, 025008 (2018).
- [7] M. G. Kozlov *et al.* Rev. Mod. Phys. **90**, 045005 (2018).

* p.micke@gsi.de

A Binary Occulter Design for creating Ultra-High Contrast Shadow

H. Iyer^{*1,2}, F. Salgado^{1,2}, D. Seipt^{1,2}, and M. Zepf^{1,2}

¹HI Jena, Fröbelstieg 3, 07743 Jena, Germany; ²IOQ, FSU Jena

We optimized serrated-occulter designs for suppressing the intensity of the incident laser background within a 3 cm wide, axial, circular section on the near-field (NF). Our designs effectively eliminate the Arago's patch produced by standard disc-shaped beam blocks planned for our future light-by-light scattering experiment [1]. To this end, Z-Scans (15 m – 200 m in 0.5 m steps) to analyze the NF of the laser (800 nm, cw) with respect to variations of the serration geometry was performed. Uniform suppression of up to six orders of magnitude was achieved across the axial region of interest.

Tailoring edges of *flat-top* beam profiles at large laser installations by using serrated apertures (SA) applied in combination with a low-pass spatial filter (SF) has been prevalent since its invention in 1978. Its working principle was provided by [2], wherein with an appropriately sized SF-pinhole the relation: $\frac{I(\rho)}{I_0} \simeq \frac{W_{Serr}(\rho)}{W_{Serr,0}}$, which connects the radial intensity $I(\rho)$ with the radial profile of the open serration's circumferential width $W_{Serr}(\rho)$; this holds best with a large number of serrations (N_{Serr}).

By simply replacing the SA with a serrated occulter (SO), we find that the same principle applies for designing an axial *flat-bottom* (FB) intensity profile nested within a wider *flat-top* background (supergaussian of order 9 and e^{-2} radius R_{Bgd}). The offset-hypergaussian serration shape [3] was chosen because it generates a radially smooth SG shadow profile, transitioning between the FB and the background's plateau, which mitigates diffractive ringing in the NF. Although ideally designed for use in the SO+SF device, we found that the desired suppression quality and levels can be achieved even without a SF.

The schematic of the SO is shown in Fig-1a. It has two parts: a central disc of radius $R_{b,\xi} = \xi R_g$, and the serrations which mount this base disc - like petals on a sunflower. From this base, $W_{Serr}(\rho)$ varies as supergaussian (of the order $P_\xi = (1 - \xi)P_0$, and e^{-2} radius $R_{g,\xi} = (1 - \xi)R_g$) till the serration tip. The ideal output profile (i.e. at $\xi = 0$; $R_{g,\xi} = R_g$, $P_\xi = P_0$) is shown as the black curve in Fig-1b, where the intensity is 86.4% I_0 at $\rho = R_g$, and 13.6% I_0 at $\rho = R_{Bgd}$. However, by making $\xi \rightarrow 0$, the inter-serration gap $L_{Serr}(\rho)$ would remain in the sub-micron scale for a large radial extent thereby complicating occulter fabrication. We overcome this problem by offsetting the serrations to the periphery of the base disc, thus allowing $\partial L_{Serr}/\partial \rho$ to change faster (Fig-1c). Offsetting, i.e. $\xi \rightarrow 1$, is achieved when the intensity profile

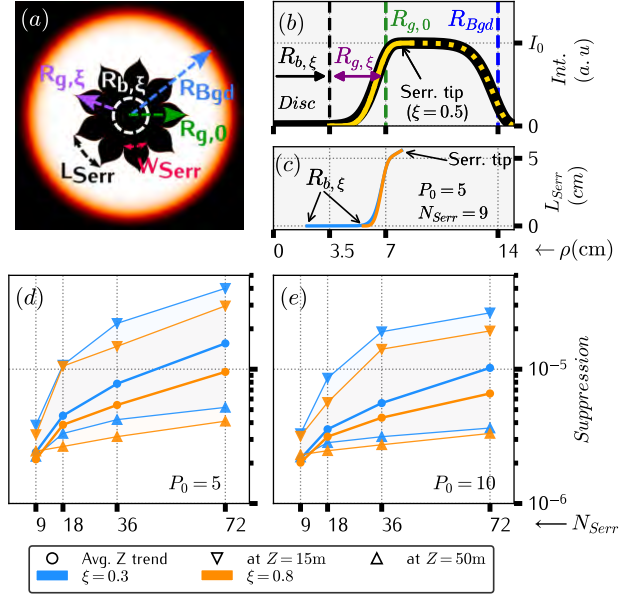


Figure 1: (a) Occulter's schematic, (b) SO+SF radial intensity profile, (c) L_{Serr} -vs- ρ , and (d,e) Suppression-vs- N_{Serr} with respect to varying P_0 and ξ .

for $\rho > R_g$ remains the same as the ideal case despite the change in the occulter's shape (yellow curves in Fig-1b).

With $R_g = 0.5 R_{Bgd} = 7$ cm fixed, the occulter's performance was evaluated for different design parameters: $P_0 \in \{5, 10\}$, $\xi \in \{0.3, 0.5, 0.8\}$, and $N_{Serr} \in \{9, 18, 36, 72\}$. The Z-Scan revealed that increasing the distance to the NF enhances the suppression of Arago's patch and the smoothness of the suppression profile. From the simulation results shown in Fig-1d-1e the best background noise suppression of about six orders of magnitude is found at $N_{Serr} = 9$, $\xi = 0.8$, and $P_0 = 10$.

In summary, our simulations show that employing only the SO with offset-hypergaussian serrations, rather than the originally proposed SO+SF setup, can achieve a smooth shadow with a suppression of $\sim 10^{-6}$ on the NF. In a direct comparison with a disc-block of radius R_g , our axial suppression level is comparable to that of the broader region of interest, highlighting the elimination of the Arago's patch. Such a NF profile aids our detector development efforts for the upcoming light-by-light scattering experiment as seen in [1].

References

- [1] F. Schütze *et al.*, Phys. Rev. D **109**, 096009 (2024).
- [2] J. M. Auerbach and V. P. Karpenko, Appl. Opt. **33**, 15 (1994).
- [3] W. Cash, Nature **442**, 51–53 (2006).

*haritejas.iyer@uni-jena.de

Second CCC of Small and Smart Series

V. Tympel^{*1,2} and F. Machalett¹

¹HI Jena, Fröbelstieg 3, 07743 Jena, Germany; ²GSI, Planckstraße 1, Darmstadt

Cryogenic Current Comparator (CCC) is a non-destructive and easy to calibrate DC beam current measuring system for the nA range. The new series called CCC-Sm stands for small and smart systems designed for beamline diameters of up to 63 mm. The second implemented sensor (Pb-DCCC-Sm-300) has two core-based pickup coils with extreme high inductance (2x 150 μ H at 4.2 K). During construction, basic investigations on noise behaviour and fluctuation-dissipation theorem) were undertaken and compared to results from the previous Sm-200 DCCC.

SQUID-electronics, magnetic field shielding and pickup coil (PUC) are essential components of a CCC [1]. For one with a flux concentrator, the PUC is also the dominant source of current noise. Ultimately, this noise will also limit the possible current resolution of the CCC-system. Increasing inductance can improve noise characteristics. This is possible through more or special core material optimized for low temperatures (Figure 1). Both strategies were pursued for the Pb-DCCC-Sm-300, whereby the total inductance could be increased by another 50% compared to the previous Sm-200 DCCC from 2022. In total, the Pb-DCCC-Sm-300 uses 8 single cores, 4 in each of the two PUCs.

The Using Fluctuation Dissipation Theorem (FDT) and inductance (L_s) and resistance (R_s) measurements [2], an expected current noise density of less than 2 pA/sqrt(Hz) could be predicted for the white noise (between 1 kHz and 100 kHz). These expected values were confirmed by later measurements on the finished CCC sensor (Figure 2). The targeted current resolution of less than 2 nA can therefore be achieved (Figure 3).

A more detailed presentation of the preparation and the results of the Pb-DCCC-Sm-300 will be published in May 2024 in the journal IEEE Transactions on Applied Superconductivity Vol.: 34, Issue: 3.

Grant-aided by the BMBF, project number 05P121SJRBI.

References

- [1] W. Vodel, R. Geithner and P. Seidel, Appl. Supercon. Handbook on Devices and Appl. Vol. 2, 1096 (2015).
- [2] R. Geithner, Ph.D. thesis, Phys. Dept., Uni. Jena, Jena, Germany (2013).

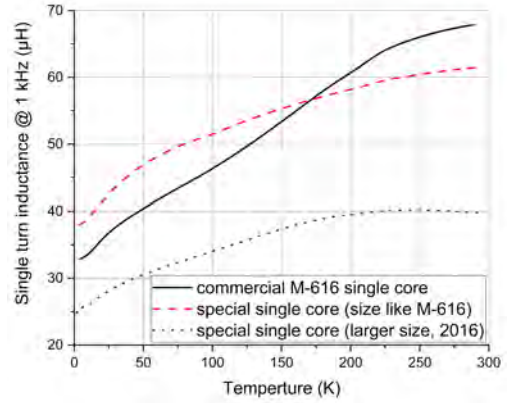


Figure 1: Comparison of achievable inductances of commercial and special low-temperature core materials.

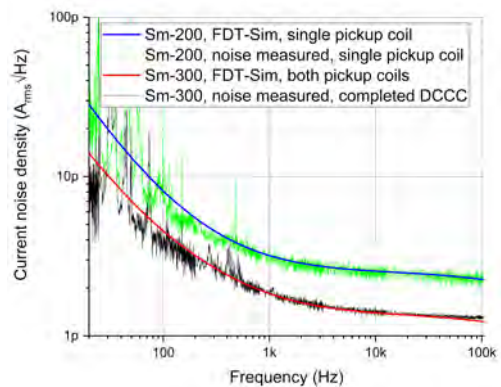


Figure 2: Comparison of noise measurements (noisy lines with disturbance peaks) at the end of CCC completion and simulations via $L_s R_s$ measurements and FDT calculations (smooth lines) at the beginning of CCC construction.

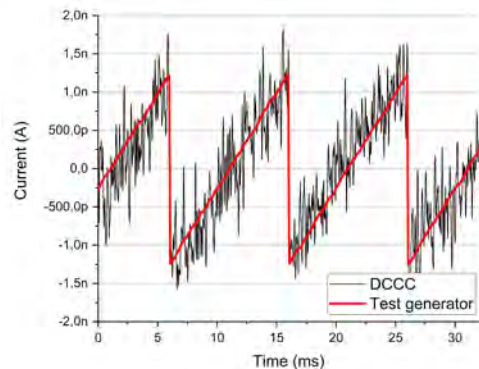


Figure 3: Current resolution of the Pb-DCCC-Sm-300.

* v.tympel@hi-jena.gsi.de

Characterization and correction of ADC artefacts in spectral data obtained with microcalorimeter detectors

D. A. Müller^{*1,2,3}, M.O. Herdrich^{1,2,3}, F. M. Kröger^{1,2,3}, B. Löher¹, Ph. Pfäfflein^{1,2,3}, G. Weber^{1,2}, and Th. Stöhlker^{1,2,3}

¹GSI, Darmstadt, Germany; ²HI Jena, Germany; ³IOQ, FSU Jena, Germany

Precision spectroscopy of hard X-rays at GSI/FAIR will profit significantly from the development and application of metallic magnetic calorimeters (MMC). Such detector systems combine a high spectral resolution, similar to crystal spectrometers, with a broad bandwidth acceptance that is comparable to semiconductor detectors. However, the advantages of these novel detectors can only be fully utilized if their spectral performance is matched by the one of the accompanying data acquisition (DAQ) system. To this purpose, the nonlinearity as well as temperature dependence of our digitizer modules were characterized and corresponding correction algorithms have been developed.

Within the SPARC collaboration, MMC detectors are being developed for precision X-ray spectroscopy of heavy, highly-charged ions. This resulted in the maXs detector design (Micro-Calorimeter Arrays for High Resolution X-ray Spectroscopy) citeref1. Detectors of this design have already been used in several test experiments on the campus of GSI/FAIR [2, 3, 4]. Recently, two maXs detector were fully integrated for the first time into the DAQ infrastructure of GSI to perform a measurement of X-ray transitions in U^{90+} [4]. The complex signal analysis requires digitisation of the entire detector response, for which several digitizer modules of the type SIS3316-125-16 from STRUCK Innovative Systems were used, which in total featured 64 individual readout channels.

To characterize our of the digitizers modules in terms of nonlinearities as well as of temperature-dependent drifts, we scanned the input voltage range (-2.5 V to 2.5 V) of each channel using a high-precision voltage source of the type HP 3245A from Agilent. An exemplary result for the integrated nonlinearity (INL) is shown in 1a), where we found a sizable deviation of up to almost ± 10 ADCs steps compared to the 'correct' ADC reading expected from the input voltage. Similarly, we also found a significant drift as a function of ambient temperature, amounting to 20 ADC steps at the edges of the input range for a change of 2° C. Such effects are expected to deteriorate the quality of the spectral data, in particular when events from several readout channels with individual characteristics are added up.

To mitigate the effects of artefacts from the non-ideal ADC characteristics, we developed correction algorithms and applied them to data that were recorded in 2021. The outcome of this procedure is presented in 1b), where the

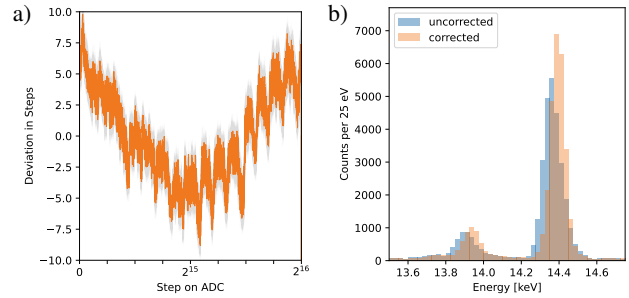


Figure 1: a) Integral nonlinearity of a single channel of the digitizer module SIS3316-125-16, obtained via a scan of over the input voltage range. b) Spectral data from a previous measurement with and without the effect of INL being corrected. A clear improvement of the spectral quality is observed.

spectra from 16 ADC channels were added up without and with application of the INL correction. For the latter case, a clear improvement of the spectral resolution is observed and also the peak position is slightly shifted. This proves that the INL characteristics did not change significantly between recording of the spectral data and characterization of the ADCs in 2023.

It is anticipated that the spectral performance of the MMC detectors will be further improved by stabilising the temperature and correcting the drift. For future measurements with maXs detectors, we will implement an on-the-fly monitoring of the ADC characteristics.

This research was conducted in the framework of the SPARC collaboration, experiment E138 of FAIR Phase-0 supported by GSI. We acknowledge support by the BMBF program ErUM FSP T05 - "Aufbau von APPA bei FAIR" (BMBF grants 05P19SJFAA and 05P19VHFA1).

References

- [1] D. Hengstler *et al.*, Phys. Scr. T166, 014054 (2015).
- [2] M. O. Herdrich *et al.*, Atoms 2023 11(1), 13 (2023).
- [3] M. O. Herdrich *et al.*, Eur. Phys. J. D 77, 125 (2023).
- [4] M. O. Herdrich *et al.*, J. Phys. B 57, 085001 (2024).
- [5] P. Pfäfflein *et al.*, Phys. Scr. 97, 114005 (2022).

* daniel.aaron.mueller@uni-jena.de

Laser-driven high-flux XUV source for coincidence experiments

J. Späthe¹, S. Hell¹, B. Ying^{1,2}, M. Wünsche^{1,2}, R. Klas^{2,3}, J. Rothhardt^{2,3}, J. Limpert^{2,3}, G. G. Paulus^{1,2}, and M. Kübel^{*1,2}

¹Institute of Optics and Quantum Electronics, FSU Jena; ²HI Jena, Fröbelstieg 3, 07743 Jena, Germany; ³Institute of Applied Physics, FSU Jena

High-harmonic generation (HHG) of femtosecond laser pulses represents an attractive method for generating coherent extreme ultraviolet (XUV) radiation. Here, we report on the development, characterization and commissioning of an HHG source of coherent extreme ultraviolet (XUV) radiation. The source has been connected to our Cold Target Recoil Ion Momentum Spectrometer (COLTRIMS) and the coincidence measurement of ions and electrons created by HHG radiation has been demonstrated. The XUV flux at 26.5 eV is estimated to exceed 10^{12} photons per second, and the intensity is evidenced by the observation of two-photon double ionization of argon. This opens novel opportunities towards our overarching goal to track and visualize the motion of electrons and nuclei during photochemical reactions in molecular movies.

Coherent radiation in the XUV spectral range offers a range of exciting applications ranging from attosecond physics to spectroscopy and high-resolution imaging. Importantly, the HHG radiation is perfectly synchronized with the driving laser pulses. However, HHG light has lacked sufficient flux for comprehensive usage in pump-probe experiments. In particular, time-resolved measurements have been largely limited to cross-correlation experiments due to the low probability of interaction with a single particle. Our new source, depicted in figure 1, opens the possibility to carry out true pump-probe experiments using XUV light. Its concept and design follow pioneering work at the HIJ and IAP [1, 2]. The HHG process is driven by 515 nm laser pulses, obtained from the frequency doubled high-power fiber laser at the HIJ and FSU's chair of non-linear optics. Live characterization of the generated XUV pulses is provided by our XUV Photoelectron Time-of-flight Spectrometer (XPETS), which parasitically detects photoelectron without affecting the beam propagation.

The source has been connected to our COLTRIMS, where first experiments show non-linear generation of Ar^{2+} by non-sequential two-photon absorption and saturation of the single-ionization step. This proves that our source is suitable to carry out pump-probe experiments using XUV light. The capability to detect photoelectrons in coincidence with the associated ion is a unique aspect of our experiments, which allows insights into light-induced dynamics [3, 4], which are otherwise inaccessible. In the XUV spectral range, stray light can produce significant background signals, making the coincidence detection of electrons and ions a particular challenge. These difficulties have now been overcome, such that clean electron-

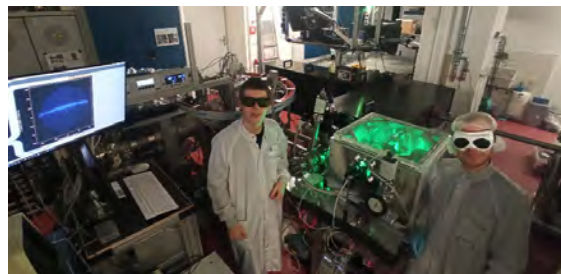


Figure 1: Photo from the lab showing the XUV source, illuminated by the green laser pulses used for HHG. In the background, the COLTRIMS with its Helmholtz coils is visible. The screen displays a position image of the ion detector, imaging the propagation of the XUV beam through the experimental chamber.

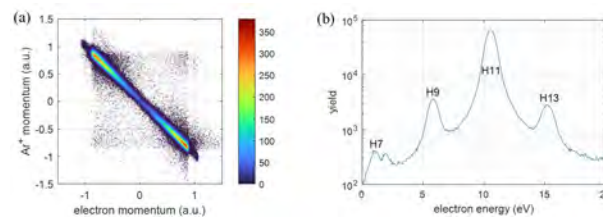


Figure 2: Coincidence measurement of the photoionization of argon (ionization potential: 15.8 eV) using XUV light. The diagonal line corresponds to momentum conservation of Ar^+ ion and photoelectron. (b) Photoelectron energy spectrum dominated by the absorption line of the 11th harmonic at 26.5 eV.

ion coincidences can be measured. This is evidenced by the clear momentum conservation trace displayed in Figure 2(a). Only very few false coincidences outside the diagonal, are observed. In addition, the photoelectron energy distribution shown in Figure 2(b) demonstrates that more than 90% of the photoelectron signal is due to the absorption of the 11th harmonic. Through this quasi-monoenergetic excitation, the energy input into the system is well-known, aiding the interpretation of future experiments on ultrafast dynamics in neutral and ionic molecules.

The authors acknowledge funding by the DFG under project No. 437321733.

References

- [1] R. Klas, et al., *Optica* 3, 1167 (2016).
- [2] R. Klas, et al., *Photonix* 2, 4 (2021).
- [3] A. Platz, et al. *Phys. Rev. A* 108, 053106
- [4] M. Kübel, et al., *Nat. Commun.* 10, 1 (2019).

*matthias.kuebel@uni-jena.de.de

Non-destructive depth reconstruction of Al-Al₂Cu layer structure with nanometer resolution using extreme ultraviolet coherence tomography

J. J. Abel^{*1}, J. Apell², F. Wiesner¹, J. Reinhard^{1,3}, M. Wünsche^{1,3}, G. G. Paulus^{1,3}, S. Lippmann², and S. Fuchs³

¹IOQ, FSU Jena, Germany; ²OSIM, FSU Jena, Germany; ³HI Jena, Germany

We report on an interferometric measurement method, extreme ultraviolet coherence tomography (XCT). Broadband XUV radiation from high harmonic generation is used for spectral reflectivity characterization of the metallic material system Al-Al₂Cu. An algorithm has been developed that allows to determine not only the depth profile of a sample, but also physical properties such as material composition and interface roughness.

Non-destructive characterization of nanoscale materials systems with the ability to allow for time-resolved in-situ studies is of great importance in materials science. This includes, e.g., the investigation of rapid phase transformations of metals and alloys, that require the measurement of interface velocity of off-equilibrium interfaces. Until now, established methods are not sufficient due to the short time scales and small length scales of the relevant processes as well as the influence of specimen damage during preparation and measurement.

Extreme ultraviolet coherence tomography (XCT) allows for the non-destructive characterization of layer structure with nanometer resolution [1]. The method uses laser-generated radiation in the extreme ultraviolet spectral range, avoiding unwanted specimen damage. We developed an advanced reconstruction algorithm [2], that allows to reconstruct the layer thicknesses (depth structure) as well as roughness of surface and buried layers. We demonstrated the method by analyzing the microstructure of a metallic Al-Al₂Cu layer system including native oxide layers (see fig. 1 (a)).

Structural properties such as layer thicknesses d_i and roughnesses $S_{q,i}$ of the sample are determined sequentially from top to bottom in the optimization process. This means that initially only the properties of the first layer are determined. Subsequently, the reconstructed parameters ($d_1, S_{q,1}$) of the first layer are used to improve the sample model for further reconstruction. On this basis, the next layer beneath is optimized. Since dispersion, absorption, and scattering losses due to the thickness and roughness of the layer above are already known from the first optimization step, only the parameters of the lower layer need to be further optimized. The procedure is repeated until the lowest layer has been addressed. In this way the sample is reconstructed step by step from top to bottom.

A complete reconstruction of the Al-Al₂Cu layer system including thickness and roughness values has been demonstrated [2]. The results were compared to TEM and AFM measurements (see table 1) and show excellent agreement.

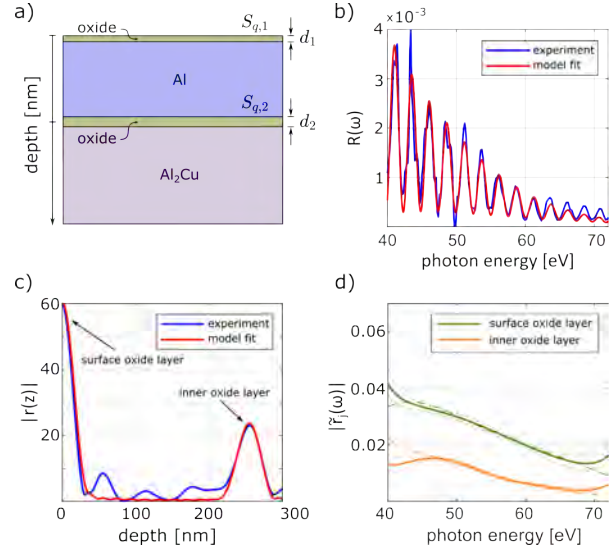


Figure 1: (a) Depth profile of sample. (b) Measured (blue) and simulated reflectivity curve from the reconstructed sample model (red). (c) Reconstructed depth profiles $r(z)$ of measured and modelled data. (d) Reconstructed reflectivity of the surface (green) and the buried oxide layers (orange).

XCT combines nano-scale resolution with the potential for ultra-fast time-resolved measurements and can be applied to a wide range of materials, including Al-, Fe-, Cu-, and Ni-base alloys, semiconductors, and oxide layers.

parameter	XCT [nm]	TEM [nm]	AFM [nm]
Al thickness	230.5 ^{+0.7} _{-0.9}	233 ± 2.0	-
d_1	2.1 ± 0.3	4.1 ± 0.3	-
d_2	3.7 ^{+1.4} _{-1.0}	6.0 ± 0.7	-
$S_{q,1}$	2.4 ± 0.2	-	2.5
$S_{q,2}$	3.5 ^{+0.1} _{-0.2}	-	0.9

Table 1: Layer thickness and roughness values attained by XCT, TEM, and AFM.

The authors acknowledge funding from German Research Foundation, European Social Fund with Thüringer Aufbaubank and Bundesministerium für Bildung und Forschung.

References

- [1] F. Wiesner *et al.*, *Optica* **8**, 230-238 (2021)
- [2] J. J. Abel, J. Apell *et al.*, *Mater. Charact.* **211**, 113894 (2024)

* johann-jakob.abel@uni-jena.de

Resonant X-ray excitation of the nuclear clock isomer ^{45}Sc

Yuri Shvyd'ko^{1,*}, Ralf Röhlsberger^{2,3,4,*}, Olga Kocharovskaya^{5,*}, and Jörg Evers^{6,*}

¹Argonne National Laboratory, Argonne, USA; ²Helmholtz Institute Jena, Jena, Germany; ³Friedrich-Schiller-Universität Jena, Germany; ⁴DESY, Hamburg, Germany; ⁵Texas A&M University, College Station, USA; ⁶Max-Planck Institut für Kernphysik, Heidelberg, Germany; *for the Scandium-45 collaboration

Using the European XFEL, an international team of researchers succeeded in exciting the sharpest atomic transition in the hard X-ray range, which is the 12.4 keV nuclear resonance of the stable isotope ^{45}Sc [1]. With its extremely narrow natural linewidth of 1.4 feV, it has the potential to become the most accurate nuclear clock ever. This has immediate applications for extreme metrology, in particular for research linked to the foundations of physics, such as time variations of the fundamental constants, the search for dark matter, as well as probing the foundations of relativity theory.

Currently, the primary timekeeping standard, used to define the SI unit of time, is based on an atomic transition in the ^{133}Cs atomic clock, providing a relative uncertainty of 10^{-16} , corresponding to one second in 300 million years. High accuracy in atomic clocks is crucial for precise time and distance measurements, which are essential for global positioning and other precision metrology applications. Future advancements in precision may come from clocks using an excited level of an atomic nucleus instead of an atomic shell transition. The atomic nucleus, being much smaller than the electron shell, is less affected by electromagnetic perturbations. The 8.3 eV level in the ^{229}Th nuclear isomer is a leading candidate, potentially allowing for clock accuracy up to 10^{-19} [2, 3].

Finding suitable radiation sources to excite these narrow resonance lines is a challenge. For optical wavelengths, powerful lasers are available, but higher transition energies require more sophisticated sources. Self-seeded X-ray free-electron lasers (XFELs) make narrow-bandwidth nuclear resonances in hard X-rays accessible for nuclear clocks. ^{45}Sc , with a transition energy of 12.4 keV, a 0.47-second excited-state lifetime, and a resonance linewidth of 1.4 feV, promises a temporal accuracy of one second in 30 billion years (10^{-18}). Its stability and 100% natural abundance make it an ideal candidate for a nuclear clock.

The scientific potential of ^{45}Sc was realized already over 30 years ago [4], but remained elusive due to lack of sufficiently intense sources. The European XFEL, operating in hard X-ray self-seeding mode (HXRSS) [5], now can produce 12.4 keV X-ray pulses suitable for exciting ^{45}Sc nuclei. In a groundbreaking experiment at the European XFEL's MID instrument, excitation of the 12.4 keV ^{45}Sc resonance line was eventually observed (Fig. 1), evidenced by detecting 93 delayed fluorescence photons out of 10^{20} X-ray pulses on a 25- μm Sc foil. This efficient detection was achieved by periodically moving the scandium foil and using well-shielded silicon drift detectors, result-

ing in a signal-to-noise ratio of 70. High-resolution crystal optics determined the scandium-45 resonance energy with 250 times higher accuracy than before, at $E_0 = 12,389.59 \pm 0.15$ (stat) ± 0.12 (syst) eV. Precise knowledge of this energy is critical for developing a nuclear clock based on ^{45}Sc . The experiment also provided new estimates for the nuclear resonance cross-section and internal conversion coefficients, enhancing understanding of this nuclear transition.

The successful resonant excitation and precise measurement of ^{45}Sc 's energy open new possibilities for ultrahigh-precision X-ray spectroscopy. Such accuracy could enable studies of gravitational time dilation on sub-millimeter scales, exploring relativistic effects previously inaccessible. This experiment showcases the potential of high repetition-rate narrow-band XFELs for studying extremely narrow nuclear resonances. Further improvements in resonant spectral flux using enhanced narrow-band 12.4-keV X-ray sources and frequency combs will be necessary to develop a nuclear clock based on ^{45}Sc .

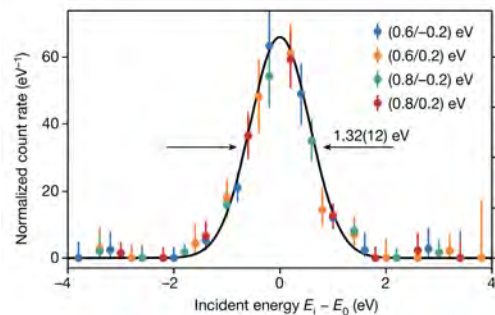


Figure 1: Resonance curve as function of the detuning of the incident energy E_i from the resonance energy E_0 . It was recorded with delayed 4 keV K-fluorescence photons of ^{45}Sc , witnessing the deexcitation of its 12.4 keV nuclear level after excitation by X-ray pulses from the European XFEL. The width of the curve reflects the bandwidth of the incident radiation.

References

- [1] Y. Shvyd'ko *et al.*, *Nature* **633**, 471 – 475 (2023).
- [2] K. Beeks *et al.*, *Nature Rev. Phys.* **3**, 238 – 248 (2021).
- [3] S. Kraemer *et al.*, *Nature* **617**, 706–710 (2023).
- [4] Yu. V. Shvyd'ko and G. V. Smirnov, *Nucl. Instrum. Methods Phys. Res. B* **51**, 452 (1990).
- [5] S. Liu *et al.*, *Nature Photonics* **17**, 984 - 991 (2023).

Imaging via Correlation of X-Ray Fluorescence Photons

Fabian Trost¹, Ralf Röhlsberger^{2,3,1}, Henry Chapman¹, and Joachim von Zanthier⁴

¹DESY, Hamburg, Germany; ²Helmholtz Institute Jena, Jena, Germany; ³Friedrich-Schiller-Universität Jena, Germany; ⁴Friedrich-Alexander Universität Erlangen-Nürnberg, Erlangen, Germany

To determine the structure of condensed matter, coherent X-ray diffraction has been an indispensable method for more than a hundred years. Today, accelerator-based X-ray sources such as synchrotron radiation sources and X-ray lasers are used for a plethora of imaging applications employing coherent light. In contrast, an experiment at the European XFEL has recently succeeded in using incoherent X-ray fluorescence photons for imaging [1] - an approach that dates back to Max von Laue and the beginnings of X-ray crystallography in 1912.

In their search for interference phenomena in atomic lattices, Walter Friedrich, Paul Knipping, and Max von Laue initially used photographic plates positioned sideways to copper sulphate crystals to detect fluorescence radiation excited by X-rays. These attempts failed until Arnold Sommerfeld pointed out that fluorescence radiation could not produce an interference pattern because the spontaneous emissions from atoms in a crystal lack a well-defined phase relationship [2]. The breakthrough occurred when the researchers placed the photographic plates behind the crystals, revealing characteristic patterns explainable by coherent X-ray wave superposition scattered by the atoms, marking the birth of X-ray crystallography and earning von Laue the 1914 Nobel Prize in Physics.

Fluorescence radiation has since been deemed unsuitable for coherent imaging, a belief valid only if detector integration times are much longer than atomic fluorescence emission times, averaging many independent emissions. If detection times are significantly shorter, emission processes within that time can be phase-coherent, creating an interference pattern. This insight led British astronomers Robert Hanbury Brown and Richard Q. Twiss (HBT) in the 1950s to apply the principle to starlight, enabling them to derive structural information such as star diameters and distances by evaluating spatial correlations of intensities recorded by separate detectors [3].

HBT's intensity interferometry, a two-photon interference phenomenon, involves indistinguishable photons from different source positions reaching separate detectors simultaneously. Extending this to atomic fluorescence radiation in the X-ray domain was previously unfeasible due to the extremely short coherence time dictated by the brief lifetime of atomic fluorescence states. For instance, a copper atom's electronic state with a K shell vacancy lasts less than 1 femtosecond (fs). However, with the advent of X-ray lasers capable of producing femtosecond or shorter pulses, such rapid excitation and subsequent intensity interferome-

try have become possible, opening new avenues in diffractive imaging with X-ray fluorescence photons [4]

A significant experimental milestone was achieved at the European XFEL, where a phase grating focused an X-ray beam with 10^9 photons per pulse at 9 keV energy and 6.2 fs pulse length onto two points of a thin copper foil, inducing K-fluorescence at 8.9 keV. The Adaptive Gain Integrating Pixel detector recorded this radiation, enabling up to 10^{12} pixel pair correlations per laser pulse. The resultant correlation signal demonstrated two-photon interference, with maxima up to the third order. Using iterative algorithms, the obtained fringe pattern was analyzed to determine the phase of the field, reconstructing the image through Fourier synthesis. This allowed the direct measurement of the size and spacing of the two fluorescent spots on the copper foil [1].

This experiment revisits von Laue's original approach, confirming that fluorescence radiation can indeed be utilized for diffractive imaging, thanks to modern femtosecond X-ray sources and advanced pixel detectors. With further advancements, this method could potentially achieve atomic resolution imaging. The European XFEL's shorter future pulses will reduce the number of required fluorescence images, potentially enabling the imaging of single molecules combined with coherent X-ray diffraction. This could facilitate element-specific and time-resolved reaction processes with atomic precision.

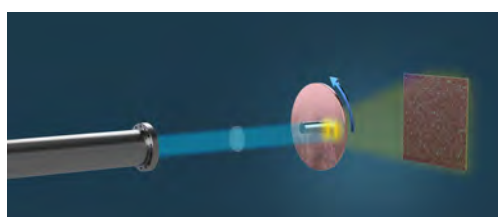


Figure 1: In the experimental setup at the European XFEL, a phase grating focuses the X-ray beam on two points (yellow) on a thin copper foil. The resulting fluorescence radiation produces a speckle pattern in the far field

References

- [1] F. Trost *et al.*, Phys. Rev. Lett. **130**, 173201 (2023).
- [2] M. Eckert, Ann. Phys. **524**, A83 – A85 (2012).
- [3] R. Hanbury Brown, R. Q. Twiss, Nature **177**, 27 – 29 (1956); Nature **178**, 1046 – 1048 (1956).
- [4] A. Classen, K. Ayyer, H. N. Chapman, R. Röhlsberger, J. von Zanthier, Phys. Rev. Lett. **119**, 053401 (2017).

Laboratory-based Correlative Fluorescence and Water-Window Microscopy

S. Kaleta^{*1,2}, J. Reinhard^{1,2}, J. Abel², F. Wiesner², M. Wünsche^{1,2}, E. Seemann³, C. Eggeling⁴, S. Fuchs^{1,2}, and G. G. Paulus^{1,2}

¹HI Jena, Faunhoferstr. 8, 07743 Jena, Germany; ²IOQ, FSU Jena; ³University Hospital Jena; ⁴Institute for Applied Optics and Biophotonics Jena

We present a correlative laboratory-based fluorescence and soft X-ray (SXR) microscope. The SXR microscope is driven by a laser produced plasma operating in the water window (WW) at 2.88 nm. A resolution of 50 nm is achieved. As an additional imaging modality a fluorescence microscope was integrated. First demonstration experiments were performed with fluorescent nanobeads and biological samples like cyanobacteria and labelled fibroblast cells.

Employing complementary imaging methods to collect data from a sample can provide a more comprehensive understanding of its properties. The WW spectral region is defined by the absorption edges of carbon and oxygen (280-530 eV/2.3-4.4 nm). This region offers a natural structural contrast based on the high absorption of the radiation in carbon compared to the high transmission in oxygen and thus water. This makes the WW particularly interesting for imaging of biological samples. In addition, the short wavelength SXR radiation enables a high resolution on the nanometer scale. The functional contrast of fluorescence microscopy perfectly complements the structural contrast of SXR microscopy allowing the identification of specifically labeled components.

The SXR microscope is realized in a compact setup (see Fig. 1) based on a laser produced plasma and utilizes a zoneplate for imaging. To generate the plasma a nanosecond laser (1064 nm, 2.5 J, 10 Hz) is focussed into a nitrogen gas stream. This results in a strong line emission at 2.88 nm with 3×10^{11} photons/(sr×pulse). The emitted radiation is focussed onto the sample by an Ni-coated ellipsoidal axisymmetrical condenser. The sample structure is imaged onto a CCD by a zoneplate with an outermost zone width of 33 nm. With this setup we can reach 50 nm half pitch resolution demonstrated with a Siemens star test target. The samples are typically prepared on SiN-membranes with a thickness of 50 nm.

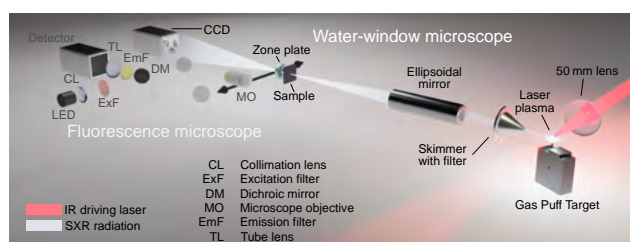


Figure 1: Schematic sketch of the correlative microscope in SXR mode. [1]

A wide-field fluorescence microscope is integrated into the vacuum chamber to complement the SXR microscope. The sample is illuminated through the microscope objective (MO) used for imaging. The MO is placed on a shared stage with the zoneplate to allow subsequent imaging with both modalities without moving the sample. Three different fluorescence filter sets are currently available to enable multi-color imaging. In addition, by exposing the sample to SXR light while taking fluorescence images, it is possible to investigate the radiation resistance of different dyes.

Various samples ranging from fluorescent nanobeads to different cell types were examined to illustrate the capabilities of this microscope. Nanobeads of different sizes and colors were chosen as a simple test sample. The selection of samples and suitable preparation techniques was done in collaboration with biologists from HKI and UKJ. NIH-3t3 and COS7 cells (different types of fibroblasts) served as more sophisticated samples. The COS7 cells shown in Fig. 2 were labeled with two colours: the mitochondria in red and the actin cytoskeleton in green. The dark structures are the nuclei of the cells.

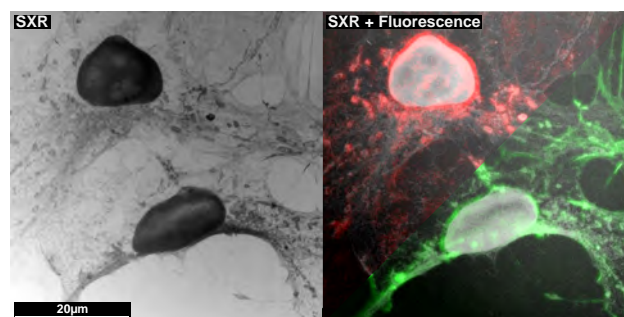


Figure 2: Image of COS7 cells. Left: SXR image of two cells with ≈ 1 h exposure time. Right: Combined SXR and fluorescence image. The mitochondria are labelled in red and the actin skeleton is labelled in green. [1]

In the future this setup will be used to investigate different science cases. Also suitable preparation techniques developed for electron microscopy will be adapted and optimized to allow even more cell types to be used.

References

- [1] J. Reinhard, S. Kaleta *et al.*, *Microsc. Microanal.* **10**, 84 (2023).

* sophia.kaleta@uni-jena.de

Polarization Phenomena of Compton Scattering in the Hard X-Ray Regime Revealed by Compton Polarimetry

T. Over^{*1,2,3}, A. Gumberidze², M. O. Herdrich^{1,2,3}, T. Krings⁴, W. Middents^{1,2,3}, Ph. Pfäfflein^{1,2,3}, U. Spillmann², G. Weber^{1,2}, and Th. Stöhlker^{1,2,3}

¹HI Jena, Fröbelstieg 3, 07743 Jena, Germany; ²GSI, 64291 Darmstadt, Germany; ³IOQ, FSU Jena, 07743 Jena, Germany; ⁴FZ Jülich, 52425 Jülich, Germany

Compton scattering describes the inelastic scattering of an energetic photon off a free electron. Also the scattering off bound electrons is often treated as Compton scattering. This is done within the impulse approximation, where the electron is considered as being free but with a momentum distribution matching that of the bound electron. Here we report on an investigation of the effect of the electron having a three-dimensional momentum on the degree of polarization of the scattered photon.

Compton scattering is an inelastic scattering process where part of the photon energy is transferred to the recoil electron. In the case of scattering from a bound electron, the binding energy as well as the momentum of the electron needs to be considered. Often also this scattering process is treated as Compton scattering if the momentum transfer in the collision is large compared to the initial momentum of the bound electron.

In the hard x-ray regime polarization can be measured with a Compton polarimeter where the anisotropy of the azimuthal scattering distribution to the polarization direction of the incident radiation is employed. The polarimeter used was developed within the SPARC collaboration. A spectral resolution of about 1 keV FWHM at a photon energy of 60 keV can be reached [1]. In more detail, the method is described in [2]. In 2020 the experiment, conducted by Middents *et al.*[3], was performed at the P07 beamline of the third generation synchrotron facility PETRAIII of DESY in Hamburg [4]. The synchrotron with a photon energy of 175 keV was scattered from a thin gold foil target [3].

In this analysis, the focus was on investigating the influence of the electron momentum on the polarization of the Compton scattered photons. Therefore, the polarization was determined in five different energy windows across the so-called Compton profile, which describes the shape of the Compton peak. At the peak center the electron momentum is approximately 0 and increases along the peak tails. As can be seen in Fig. 1, there is the indication that the degree of linear polarization decreases at the tails of the Compton peak. This would mean that a non-vanishing electron momentum has an influence on the polarization. It is worth noting that the statistics drops significantly at the tails, which leads to higher uncertainties. The nature of this effect and also the influence of a possible polarization of the background is subject of ongoing analysis.

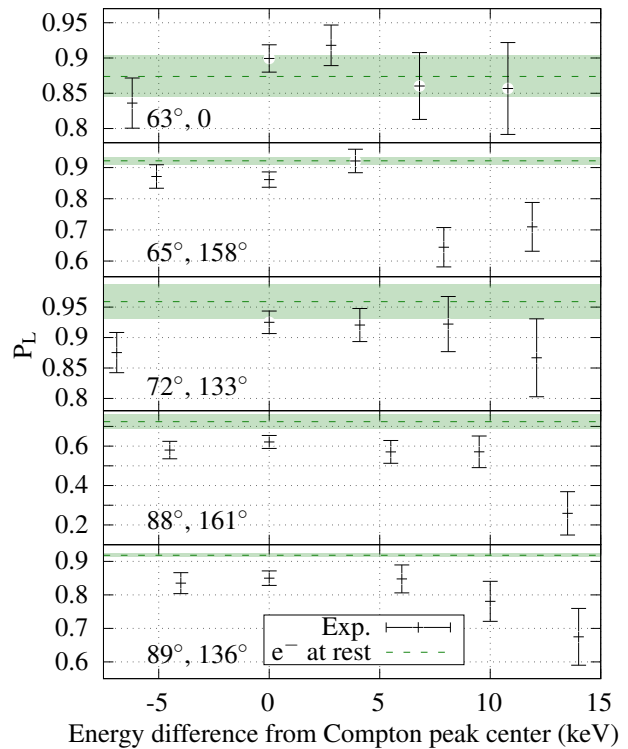


Figure 1: Measured degree of linear polarization (P_L) at five different measurement positions of the Compton polarimeter, see [5] for details. In green, the theoretical prediction for Compton scattering off a free electron at rest. The energy scale is shifted so that the center of the Compton peak is at 0.

The authors acknowledge funding from ErUM-FSP APPA (BMBF n° 05P19SJFAA).

References

- [1] W. Middents *et al.*, *Ann. Phys.* **534**, 2100285 (2022).
- [2] M. Vockert *et al.*, *NIM B* **408**, 313 (2017).
- [3] W. Middents *et al.*, *Phys. Rev. A* **107**, 012805 (2023).
- [4] N. Schell *et al.*, *MSF* **772**, 57 (2013).

*t.over@hi-jena.gsi.de

Towards a three-dimensional reconstruction of Compton scattering events within a Compton polarimeter

H. El-Ammari^{1,2,3}, W. Middents^{1,2,3}, T. Over^{1,2,3}, G. Weber^{1,2}, and Th. Stöhlker^{1,2,3}

¹GSI, Darmstadt, Germany; ²HI Jena, Germany; ³IOQ, FSU Jena, Germany

Over the last two decades, Compton polarimetry of hard x-rays has proven to be a unique tool to study spin-dependent and relativistic effects in the realm of atomic physics at high field strengths. In many of these measurements, detectors based on doubled-sided segmented semiconductor crystals have been used as Compton polarimeters. In the SPARC collaboration, such studies were performed while relying on the two-dimensional sensitivity that is provided by their segmentation. We are now also obtaining information on the penetration depth within the detector crystal to achieve a three-dimensional reconstruction of Compton scattering events.

Compton polarimetry is based on the anisotropy of the azimuthal Compton scattering cross section with respect to the polarization vector of the incident photon. More specifically, scattering of the photon perpendicular to the incident photon polarization is preferred while scattering in the parallel direction is less likely. Thus, the degree and orientation of the linear polarization of an incident X-ray beam can be determined from the emission pattern of a large number of Compton scattered photons [1]. X-ray detectors consisting of large-volume semiconductor crystals that are segmented into strips both on the front and back side can be used as highly efficient Compton polarimeters. Combining the segmentation of both sides results in a pseudo-pixel structure, where each segment of the detector can act as a scatterer for the incident radiation and also as an absorber for the scattered photons, see [2] for details.

The measurement of the incident photon polarization relies on the reconstruction of a large number of Compton scattering events that occurred within the detector. While the recoil electron deposits its energy in close vicinity to the position where the scattering occurred, the scattered photon is detected at a different position within the crystal. Thus, each segment of the detector crystal acts as a scatterer and also as an absorber for the scattered photons. So far, the reconstruction of these events relied on using the two-dimensional position information provided by the segmentation, combined with a measurement of the energy splitting between the scattered photon and the recoil electron.

Additional information, that is also highly relevant for the possible use of such detector systems for Compton imaging [3], could be gained from a measurement of the penetration depth for each energy deposition event. To this purpose we investigated the difference in arrival times of the signals on the segments on the front side and the back side of the detector crystal. We used a detector consisting

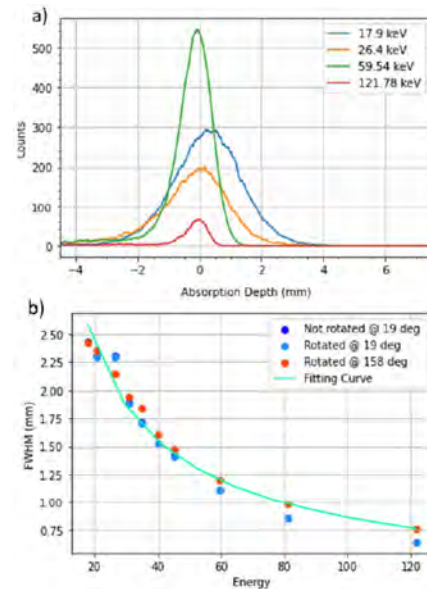


Figure 1: Top: Distribution of penetration depth measurements for various incident photon energies, showing cases where all photons are stopped close to the front surface of the detector crystal. Bottom: Resolution of the penetration depth measurement as a function of incident photon energy for various measurement runs.

of a single Li-drifted planar silicon crystal with a thickness of 7 mm. Each side of the crystal is segmented into 32 strips with a pitch of 2 mm giving an active area of $64 \times 64 \text{ mm}^2$. For more details on the detector see [4].

The arrival times of the detector pulses were determined via the constant fraction discrimination (CFD) function of MSCF-16-LN modules. The difference in arrival times on both sides of the detector crystal is determined by the different drift time of holes and electrons as well as the penetration depth. By doing a scan of different penetration depths, we established the relation between the depth of the energy deposition to the difference in CFD times.

The results of this procedure are presented in Fig. 1. As the signal-to-noise ratio improves with larger signals, the jitter of the CFD timing information decreases for larger photon energies. This results in an improved resolution for the obtained penetration depth.

References

- [1] F. Lei et al., Space Sci. Rev. **82**, 309 (1997).
- [2] G. Weber et al., J. Phys. B **48**, 144031 (2015).
- [3] R.K. Parajuli et al., Sensors **22**(19), 7374 (2022).
- [4] G. Weber et al., 2010 JINST **5**, C07010 (2010).

*hajar.el-ammari@uni-jena.de

First X-ray Spectroscopy Measurements with S-EBIT II

R. Simon^{*1,2,3}, T. Morgenroth^{1,2,3}, and S. Bernitt^{1,2}

¹Helmholtz Institute Jena, Fröbelstieg 3, 07743 Jena, Germany; ²GSI Helmholtzzentrum für Schwerionenforschung GmbH, Planckstraße 1, 64291 Darmstadt, Germany; ³IOQ, Friedrich Schiller University Jena, 07743 Jena, Germany

S-EBIT II is an electron beam ion trap (EBIT) installed at the slow-ion facility HITRAP at GSI [1]. It will serve as a local ion source for HITRAP and could support local experiments like the ARTEMIS g-factor experiment [2] or the upcoming cryogenic Paul trap for quantum logic spectroscopy. Furthermore, it can be used as a standalone experiment for spectroscopy measurements on highly charged ions. The ongoing commissioning of S-EBIT II has entered its final stage, establishment of an electron beam and detection of trapped highly charged ions.

Along the way, some technical difficulties had to be overcome. It was found that the so-called bucking coil of the electron gun did not adequately compensate the magnetic field of the trap's superconducting magnet, which is necessary for emission and propagation of the electron beam. Subsequent investigations revealed that parts of the electron gun assembly were manufactured from incompatible ferromagnetic materials. This led to the redesign of large parts of the electron gun, including an increase in the number of bucking coil windings, as well as measures to improve cooling, both with the aim to support higher currents, resulting in a higher magnitude of the compensation field.

After implementation of these changes, a first stable electron beam was established. This was a major milestone. Furthermore, the production and storage of highly charged argon ions in the trap could be validated by taking the first X-ray emission spectrum, shown in figure 1.

This enabled first experiments on dielectronic recombination (DR) with argon ions in S-EBIT II. These first measurements focused on DR of Ar^{12+} to Ar^{16+} . X-ray fluorescence following resonant electron capture was recorded as a function of the electron beam energy, covering KLL, KLM, and higher- n resonances.

Subsequent measurements focused on KLL resonances. The Jena Atomic Calculator (JAC) [3] was used to calculate theoretical resonance energies and strengths, which were then used to estimate relative populations of ions in different charge states (see figure 2), demonstrating the feasibility of this approach for trap diagnostics.

During these experiments, the maximum stable electron current was limited to approximately 0.75 mA, due to technical limitations of the electron gun, persistent even after considerable effort put into possible improvements by introducing passive magnetic shielding. Work on a complete replacement of the electron gun has started.

First electrostatic ion beam optics elements for extrac-

tion of ions into the HITRAP beamline have been installed. Other parts of the connection of S-EBIT II to HITRAP have been prepared for installation.

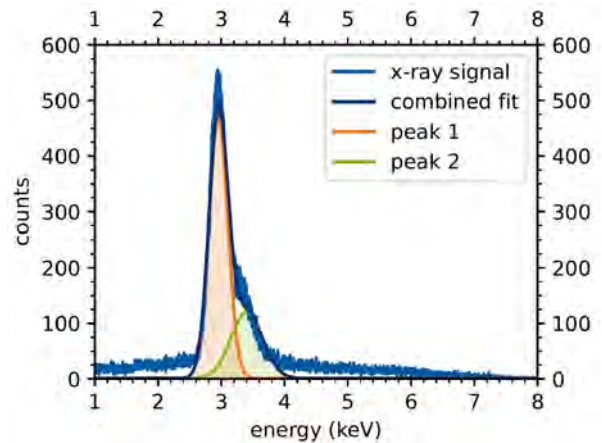


Figure 1: The first X-ray spectrum obtained with S-EBIT II at GSI, using an electron beam energy of 8.4 keV. Peak 1 corresponds to the K_{α} emission of Ar L-shell ions, and peak 2 corresponds to the K_{β} emission of Ar L-shell ions and K_{α} emission of Ar K-shell ions.

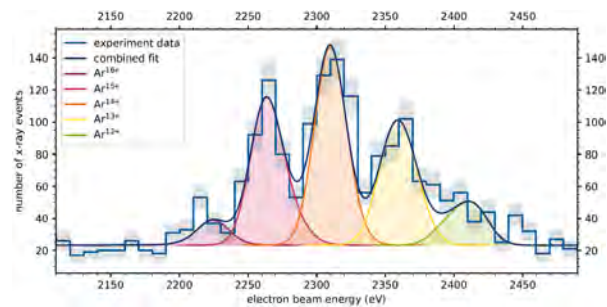


Figure 2: One-dimensional histogram of fluorescence photons registered around the KLL DR resonances of Argon, together with the fitted theoretical DR resonances for Ar^{12+} to Ar^{16+} , calculated with JAC.

References

- [1] H. J. Kluge *et al.*, *Adv. Quantum Chem.* **53**, 83 (2007).
- [2] M. Vogel *et al.*, *Ann. Phys.* **531**, 1800211 (2018).
- [3] S. Fritzsche *et al.*, *Comput. Phys. Commun.* **240**, 1–14 (2019).

*re.simon@gsi.de

High-Precision X-ray Spectroscopy for Astrophysics with PolarX-EBIT

S. Bernitt^{*1,2}, C. Shah^{3,5}, M. Togawa^{4,5}, M. Botz⁵, R. Steinbrügge⁶, M. A. Leutenegger³, and J. R. Crespo López-Urrutia⁵

¹GSI Helmholtzzentrum für Schwerionenforschung GmbH, Planckstraße 1, 64291 Darmstadt, Germany; ²HI Jena, Fröbelstieg 3, 07743 Jena, Germany; ³NASA/Goddard Space Flight Center, 8800 Greenbelt Rd., Greenbelt, MD 20771, USA; ⁴European XFEL, Holzkoppel 4, 22869 Schenefeld, Germany; ⁵MPI für Kernphysik, Saupfercheckweg 1, 69117 Heidelberg, Germany; ⁶DESY, Notzkestraße 85, 22607 Hamburg, Germany

The imaging X-ray calorimeter detector onboard the XRISM satellite observatory will provide high-resolution X-ray spectra of the active galaxy M87, which is host to a supermassive black hole (SMBH). This will provide a sensitive test of our understanding of how accretion onto a SMBH couples to its galaxy-scale environment, influencing star formation. The interpretation of these observations critically depends on the availability of precise rest wavelengths of strong L-shell transitions in highly charged iron ions. To provide this data, we performed resonant photoexcitation experiments with the portable compact electron beam ion trap PolarX-EBIT [1] at the synchrotron light source PETRA III.

PolarX-EBIT provided a target of trapped iron ions in various charge states of interest, which were illuminated by a monochromatized photon beam at beamline P04 of the PETRA III synchrotron light source. Resonantly excited X-ray fluorescence was recored while scanning the energy of incoming photons. Simultaneously, the ASPHERE electron spectrometer [2] was used to measure kinetic energies of photoelectrons released from a gold foil illuminated by the photon beam. This was possible due to the unique off-axis electron gun of PolarX-EBIT, allowing transmission of the beam through the trap, and it enabled tracking changes

in the photon energy, overcoming limitations in achievable absolute resonance-energy accuracy encountered during previous experiments [3]. Data analysis is currently ongoing.

These measurements expand on previous successful efforts to use PolarX-EBIT to provide valuable atomic data for the interpretation of astrophysical observations, as well as for benchmarking latest atomic structure calculations [4, 5, 6].

The authors acknowledge funding from BMBF through Project 05K13SJ2, MPG, the NASA Postdoctoral Program, and the NASA Astrophysics Program. Experimental facilities were provided by DESY.

References

- [1] P. Mücke *et al.*, Rev. Sci. Instrum. **89**, 063109 (2018).
- [2] K. Rossnagel *et al.*, Nucl. Instrum. Methods Phys. Res. A **467–468**, 1485–1488 (2001).
- [3] C. Shah *et al.*, <https://arxiv.org/pdf/2401.08395v2> (2024).
- [4] R. Steinbrügge *et al.*, ApJ **941**, 188 (2022).
- [5] S. Kühn *et al.*, Phys. Rev. Lett. **129**, 245001 (2022).
- [6] C. Shah *et al.*, Phys. Rev. A **109**, 063108 (2024).

*s.bernitt@hi-jena.gsi.de

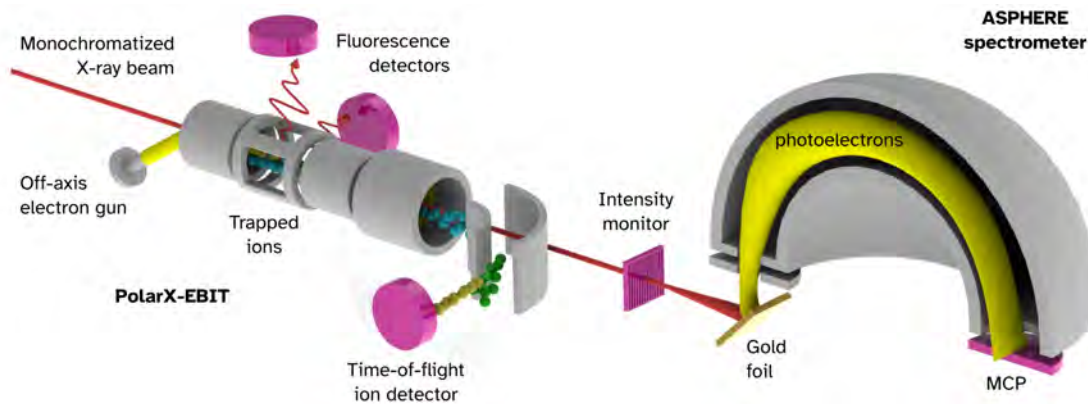


Figure 1: Highly charged ions trapped in PolarX-EBIT [1] are illuminated with monochromatized X-radiation provided at beamline P04 of PETRA III. Resonantly excited fluorescence and ion charge state populations are measured as functions of the X-ray photon energy. The ASPHERE electron spectrometer [2] allows to track changes in the photon energy. (Adapted from [3].)

Background measurements of the Darkfield technique for Quantum Vacuum Birefringence at the European XFEL

P. Khademi^{*1,2}, A. Sävert^{1,2}, W. Hippler^{1,2}, R. Löttsch^{1,2}, G. G. Paulus^{1,2}, and M. Zepf^{1,2}

¹HI Jena, Fröbelstieg 3, 07743 Jena, Germany; ²IOQ, FSU Jena

Free electron laser facilities, such as the European XFEL, offer a unique opportunity to explore quantum vacuum nonlinearities, including vacuum birefringence. Detecting these phenomena requires extremely strong electromagnetic fields, posing a significant challenge. One approach to address the high background-to-signal ratio involves creating a shadow (darkfield) on the beam axis to detect the signal in this low-background region. To validate this technique, initial measurements of this background in the shadow were conducted at the HED instrument at the EuXFEL.

Theoretical predictions show that in the interaction of extreme macroscopic electromagnetic fields with the quantum vacuum, namely light-by-light scattering ($\gamma\gamma \rightarrow \gamma\gamma$), the vacuum exhibits birefringence, i.e., changing the field polarization state. The first-order cross section for this elastic scattering process scale with the center-of-mass frequency ω_{cms}^6 . This scaling condition encourages the use of higher photon energies, such as X-rays. The final experiment is envisioned at HED-HiBEF, with the optimal opportunity of combining an XFEL probe beam with an intense optical laser pump beam [1].

The darkfield two-beam scheme creates a shadow by inserting a well-defined obstacle into the incident beam, within the converging and expanding beam, while maintaining a central intensity peak at the focus [1], see Fig. 1. The main focus of this experiment was to quantify the quality of the shadow, specifically the background level in the probe beam.

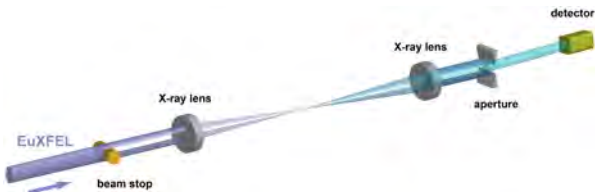


Figure 1: Layout illustration the darkfield technique [1].

For this campaign, the XFEL photon energy was 8766 eV, with a beam diameter of 400 μm . We created the shadow using chemically polished tungsten wires with diameters of 180 μm and 160 μm as obstacles. The beam was then focused using CRL X-ray lenses, and this focused beam was subsequently imaged with a second CRL on the X-ray single-photon camera called Jungfrau, which has a pixel size of 75 μm . To suppress diffraction and scattering within the region of interest (ROI), a 80 μm PtIr-pinhole and tungsten slits were inserted. The slits were opened and

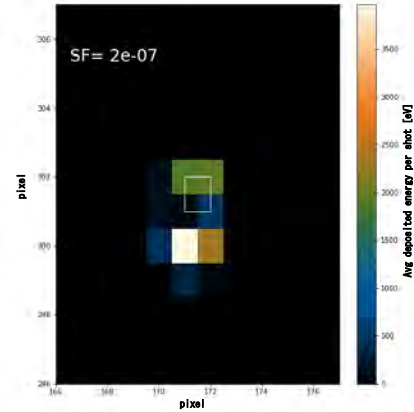


Figure 2: Darkfield on Jungfrau in one of the runs. This shows the ROI defined based on the position of the obstacle for the shadow. The shadow factor (SF) in the white square as ROI is calculated. The color bar is the eVs deposited in each pixel.

fine-tuned to the size of the shadow in the incident beam to ensure optimal conditions.

Preliminary results, depicted in Fig. 2, illustrate an example from a run using a 160 μm polished tungsten wire to create the shadow. Inserting the obstacles resulted in a transmission of 23% to the focus. The shadow factor (SF), defined as the difference in single pixel values with and without obstacles. The color bar indicates the average energy deposited per pixel in electron volts. The shadow factor (SF) measured within the white square, representing the ROI, yielded 2×10^{-7} .

The darkfield technique has shown substantial capabilities in suppressing background noise. During this campaign, further improvement in the shadow factor (SF) was achieved through techniques like channel cuts to suppress polarized background photons. Achieving a shadow factor of approximately ($\text{SF} = 10^{-13}$) is crucial for detecting photons with flipped polarization induced by quantum vacuum birefringence. This goal can be reached by enhancing setup components such as obstacles, slits, and detectors. Initial results are promising for achieving these advancements.

The authors wish to acknowledge the close collaboration and support received from the Helmholtz International Beamline for Extreme Fields (HiBEF) consortium.

References

- [1] F. Karbstein *et al.*, arXiv:2405.18063 (2024).

* p.khademi@hi-jena.gsi.de

Progress Report of the Negative Ions Laser Photodetachment Project

Oliver Forstner*^{1,2}, Shiva Prasad Pulipati², and Klaus Wendt³

¹HI Jena, Fröbelstieg 3, 07743 Jena, Germany; ²IQO, FSU Jena; ³Institut für Physik, Johannes Gutenberg–Universität Mainz

The negative ions laser photodetachment project aims to use the element selectivity of photodetachment to suppress isobars in high sensitive mass spectrometry. A dedicated ion beam cooler will be used to efficiently deplete the unwanted isobars via interaction with tunable lasers. In 2023 the main focus was on the installation of a sputter ion source for the production of negative ions.

In the LISEL setup photodetachment of negative ions will be used to improve the sensitivity of mass spectrometry [1]. The negative ions will be produced by a sputter ion source, where cesium vapour is ionized on a hot ionizer. The resulting positive cesium ions will be accelerated towards a solid target where atoms will be released by the bombardment with the keV cesium ions. Some of the atoms pick up an electron from the surrounding cesium vapour and subsequently accelerated towards an extraction electrode [2]. The resulting beam with a maximum kinetic energy of 30 keV will be focussed by an Einzel lens. After mass separation by a 90° double focusing sector magnet the ions will enter the ion beam cooler where they are slowed down and overlapped with the laser beam. A sketch of the sputter ions source with extraction and Einzel lens is shown in Fig. 1.

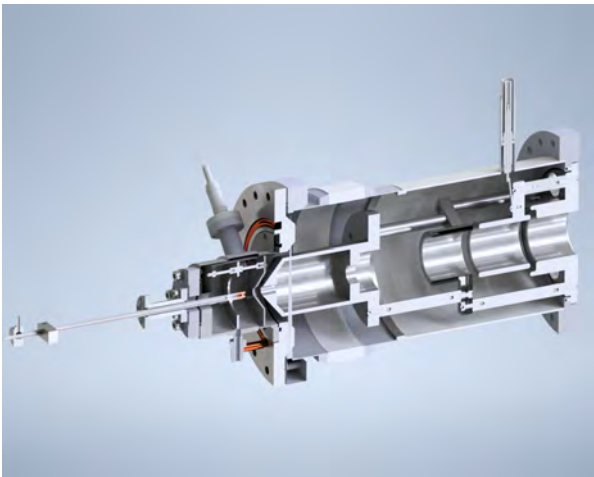


Figure 1: CAD sketch of the sputter ion source with the extraction electrode and the Einzel lens. The cooled target is mounted in front of the hot ionizer. The sample is pressed into the hole in the front of the target holder where it is exposed to the cesium ions from the ionizer. The sputtered atoms pick up electrons from the cesium vapour and are accelerated towards the extraction electrode.



Figure 2: The sputter ion source mounted on the beamline. The electronics and power supplies reside in a high voltage cage below the ion source. The cooling of the target and the flange is realised from ground potential by a dedicated dielectric fluid.

The sputter ion source is installed on a high voltage deck together with the required power supplies for the ionizer, the cesium oven and the cathode voltage. The control of the devices is integrated in the Beckhoff control system of the LISEL setup. The ionizer is heated to about 1400 K which requires cooling of the target and the support flange of the ion source. A dedicated cooling system has been developed which uses a special cooling liquid with a high dielectric strength of more than 30 keV (Thermasafe R from DCX, Poland).

This project is supported by funding from the German Ministry of Science BMBF, joint project 05K2019 – LISELatDREAMS and joint project 05K2022 – ELISEatIBC.

References

- [1] O. Forstner *et al.*, The ILIAS project for selective isobar suppression by laser photodetachment, *Nucl. Instr. and Meth. B* **361**, 217-221 (2015).
- [2] D. Koll *et al.*, Search for Recent Fe-60 Deposition in Antarctica with AMS, Master's thesis, Tu Munich, 2018.

* o.forstner@hi-jena.gsi.de

Fast ion cooling and ion cloud preparation with the HILITE Penning trap

S. Ringleb^{*1}, M. Kiffer¹, M. Vogel², and Th. Stöhlker^{1,2,3}

¹Institut für Optik und Quantenelektronik, FSU Jena, 07743 Jena; ²GSI Helmholtzzentrum für Schwerionenforschung GmbH, 64291 Darmstadt; ³Helmholtz-Institut Jena, 07743, Jena

We have developed a method to deduce the energy evolution of a captured ion ensemble in a Penning trap. By careful control of the ion capture process we could achieve fast cooling of the ions' centre-of-mass energy and have reduced the residual energy to a minimum.

Experiments with ensembles of highly charged ions in Penning traps typically have the demand for externally produced ions which are then captured in the trap. The ions are typically produced in an Electron-beam Ion Trap (EBIT) providing high energetic ions which have to be decelerated and cooled to conduct precision experiments with the ions. An established technique to cool ions is resistive cooling. Using this technique, typically the axial ion motion is coupled to a resonant circuit where the energy is dissipated by the real part of the resonator's impedance. Unfortunately, only the centre-of-mass motion of the ions can be addressed by the resonator, while the uncorellated motion of the ions with respect to each other can be cooled only indirectly by energy transfer to the centre-of-mass motion. The whole ion ensemble can be described by three different energies: the centre-of-mass energy (E_{cm}), the uncorellated axial energy (E_{ax}) and the radial energy (E_r). Between the three energies there is a persistant energy exchange described by following set of rate equations:

$$\begin{aligned} \frac{dE_{cm}}{dt} &= -\gamma_{cool}(E_{cm} - k_B T_0) + \gamma_{ax} \left(\frac{1}{N-1} E_{ax} - E_{cm} \right) \\ \frac{dE_{ax}}{dt} &= -\gamma_{ax} \left(\frac{1}{N-1} E_{ax} - E_{cm} \right) - \gamma_r \left(E_{ax} - \frac{N-1}{2N} E_r \right) \\ \frac{dE_r}{dt} &= \gamma_r \left(E_{ax} - \frac{N-1}{2N} E_r \right), \end{aligned} \quad (1)$$

where the prefactors γ_{cool} , γ_{ax} , and γ_r are the energy transfer coefficients of the system. The parameter γ_{cool} is the cooling factor of the centre-of-mass motion and is directly connected to power dissipation of the system. The evolution of the centre-of-mass energy is monitored using a normal-conducting resonator which is connected to two electrodes places symmetrically to the trap centre. The detailed setup is described in [1].

Initially, the centre-of-mass motion is cooled fast which is represented by the fast descending ion signal in figure 1a). After 200 ms, the ion signal is almost constant. The level of the ion signal is proportional to the energy in the axial uncorellated motion. From these so-called cooling curves we can characterise the ion bunch upon capture and determine the number of stored ions, the initial centre-of-mass energy as well as the final axial energy. The coefficients given in equation 1 are deduced by fitting the three rate equations to the acquired ion signal. Measuring the ions

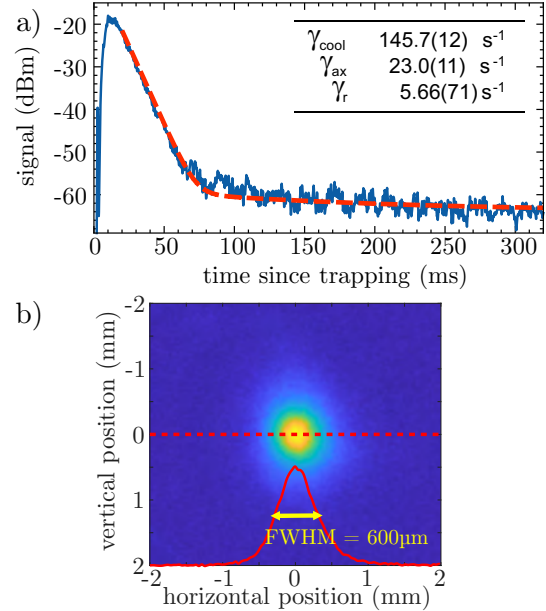


Figure 1: a) Time-dependence of the signal of trapped ions. The power level is proportional to the centre-of-mass energy. The fit function corresponds to the rate equations in equation 1. b) Radial ion distribution acquired with a spatial sensitive MCP detector. [1]

off resonance one can also determine the energy transfer to the uncorellated motion, exclusively [2]. As the final axial energy is a measure for the spatial distribution in the axial direction we can deduce the ion density in the trap centre from this energy in combination with the knowledge of the radial profile of the ion cloud (figure 1b) measured with a spatial sensitive micro-channel plate with phosphorus detection anode. Finally, we have been able to store 20.000 Ne^{8+} ions in the trap and confined then to a density of $1 \times 10^5 \text{ mm}^{-3}$. This value is sufficiently high to perform experiments with high intensity laser systems with ion production rates of several hundreds per minute.

Beside our experimental setup, this technique can be used in any other Penning trap experimental setups to obtain ion ensembles with low centre-of-mass energy. We will combine the dense ion plasma with the strong laser Jeti200 to perform laser ionisation experiments with hydrogen-like ions up to neon. From the acquired data we will be able to reconstruct the intensity in the laser focus.

References

- [1] M. Kiffer *et al.*, Phys. Rev. A **109**, 033102 (2024).
- [2] S. Ringleb *et al.*, Eur. Phys. J. Plus **139**, 401 (2024).

* stefan.ringleb@uni-jena.de

First experimental determination of the branching ratio of an intra-shell transition in a He-like heavy ion system

F.M. Kröger^{*1,2,3}, S. Allgeier⁴, Z. Andelkovic¹, S. Bernitt^{3,2,1}, A. Borovik⁶, L. Duval⁷, A. Fleischmann⁴, O. Forstner^{1,2,3}, M. Friedrich⁴, J. Glorius¹, A. Gumberidze¹, Ch. Hahn^{1,2}, F. Herfurth¹, D. Hengstler⁴, M.O. Herdrich^{1,2,3}, P.-M. Hillenbrand¹, A. Kalinin¹, M. Kiffer^{1,2,3}, T. Köhler³, M. Kubullek³, P. Kuntz⁴, M. Lestinsky¹, B. Löher¹, E.B. Menz^{1,2,3}, T. Over^{1,2,3}, N. Petridis¹, Ph. Pfäfflein^{1,2,3}, S. Ringleb^{1,2,3}, R.S. Sidhu⁴, U. Spillmann¹, S. Trotsenko^{1,2}, A. Warczak⁵, G. Weber^{1,2}, B. Zhu^{1,2,3}, C. Enss⁴, and Th. Stöhlker^{1,2,3}

¹GSI, Darmstadt, Germany; ²HI Jena, Germany; ³IOQ, FSU Jena, Germany; ⁴KIP, Heidelberg Univ., Germany;

⁵Jagiellonian Univ., Krakow, Poland; ⁶I.PI, Gießen Univ., Germany; ⁷LKB, Univ. Paris Sorbonne, Paris, France

The investigation of the atomic structure of heavy ions allows to probe the interplay of the effects of QED, relativity as well as electron-electron interactions in strong fields. He-like uranium poses the heaviest naturally occurring, simplest multi-electron system, and is therefore an ideal study subject to put theoretical predictions on the test. However, in contrast to low- Z systems, experimental data on high- Z systems is very scarce due to the technical challenges posed by heavy systems. In this context, we present data from an experiment where novel microcalorimeter detectors were employed at the CRYRING@ESR electron cooler to investigate the spectral emission of U^{90+} . This allowed us to extract for the first time experimentally the E1/M2 branching ratio of transition from the excited $2p_{3/2}^3P_2$ state of a heavy He-like system.

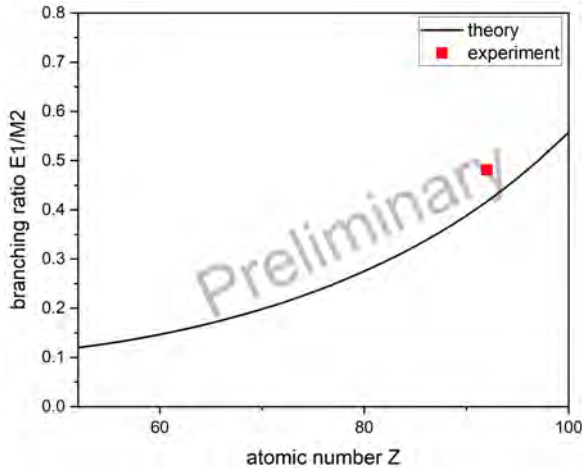


Figure 1: Experiment-based branching ratio, showing the relation of the E1 and M2 transition rates from the $3P_2$ state, compared to theory of [5].

The experiment was conducted at the electron cooler of the CRYRING@ESR, see [1] for details. There excited U^{90+} ions were formed via radiative recombination of cooler electrons with a stored U^{91+} beam. The photons emitted during the radiative decay of the excited ions were

then detected under 0° and 180° , using two novel metallic magnetic calorimeter (MMC) detector systems [2]. Detection of the U^{90+} ions by a particle counter behind the first dipole magnet downstream from the electron cooler enabled suppression of background radiation via setting of a coincidence conditions between photons and ions [3].

The $2p_{3/2}^3P_2$ state in He-like systems mostly decays via the $\Delta n = 0$ E1 transition into the $2s_{1/2}^3S_1$ or via M2 transition into the ground state. For light systems, the E1 transition is dominant, with the relative importance of the M2 transition increasing as the atomic number Z increases. After M2 overtaking the E1 rate at $Z = 19$, however, at $Z = 38$ the behaviour reverses, so that the E1 transition is becoming more relevant again with further increasing Z [4].

Due to the excellent spectral resolution of the MMC detectors (< 100 eV FWHM), we were able to disentangle the x (from $2p_{3/2}^3P_2$) and z (from $2s_{1/2}^3S_1$) transitions into the ground state. From their relative intensities we performed an indirect determination of the aforementioned E1/M2 transition rate ratio. This is the first experimental determination of this quantity in a heavy He-like system. In Figure 1, a preliminary value of the E1/M2 ratio is presented in comparison to calculations by Johnson *et al.* [5]. Reasonable agreement is found. The final result, containing also an uncertainty estimation, will be subject of an upcoming publication.

This research was conducted in the framework of the SPARC collaboration, experiment E138 of FAIR Phase-0 supported by GSI. We acknowledge support by the ERC under the European Union's Horizon 2020 research, by the innovation program (grants 824109 'EMP') as well as by ErUM FSP T05 - "Aufbau von APPA bei FAIR" (BMBF grants 05P19SJFAA and 05P19VHFA1).

References

- [1] P. Pfäfflein *et al.*, Phys. Scr. **97**, 114005 (2022).
- [2] D. Hengstler *et al.*, Phys. Scr. **T166**, 014054 (2015).
- [3] P. Pfäfflein *et al.*, Atoms 2023, **11**, 5 (2022).
- [4] T. Stöhlker, habilitation treatise, Frankfurt university (1999).
- [5] W. R. Johnson *et al.*, Adv. At. Mol. Opt. Phys. **35**, 255 (1995).

*felix.kroeger@uni-jena.de

Low-energy Dielectronic Recombination of Ne^{3+} Measured at CRYRING@ESR

E. B. Menz^{*1,2,3}, E.-O. Hanu^{1,3}, M. Lestinsky³, M. Looshorn⁴, W. Biela-Nowaczyk³, C. Brandau^{3,4}, M. Fogle⁵, P.-M. Hillenbrand^{3,4}, R. Schuch⁶, K. Ueberholz⁸, G. Vorobyev³, S. Wang⁴, A. Warczak⁷, S. Schippers⁴, and Th. Stöhlker^{1,2,3}

¹Helmholtz Institute Jena, 07743 Jena; ²Institute of Optics and Quantum Electronics, University of Jena, 07743 Jena; ³GSI Helmholtzzentrum für Schwerionenforschung, 64291 Darmstadt; ⁴I. Physikalisches Institut, Justus Liebig University, 35390 Gießen; ⁵Department of Physics, Auburn University, AL 36832, USA; ⁶Department of Physics, Stockholm University, 106 91 Stockholm, Sweden; ⁷Institute of Physics, Jagiellonian University, 30-348 Krakow, Poland; ⁸Institut für Kernphysik, University Münster, 48149 Münster

In November and December 2023 an experiment on dielectronic recombination on Ne^{3+} was performed at CRYRING@ESR. We used the unique experimental conditions of the electron cooler to measure low-energy resonances of this astrophysically relevant ion species in merged-beam configuration. The experiment is part of an ongoing programme of astrophysically motivated DR measurements on light ion species.

Dielectronic recombination (DR) is a resonant electron capture process in which one electron is captured from the continuum into an atomic bound state while a second, already bound, electron is raised to a higher energy level. As a resonant process it is an important factor in determining the charge-state balance in plasmas. Theoretical prediction of DR rates is quite reliable for higher energies but has been shown to be unreliable for lower energies in the region of a few eV and below [1]. Accurate recombination rates for a light ion species in low charge states can provide valuable data for modelling cold plasma environments like planetary nebulae. Recombination experiments at the electron coolers of ion storage rings are an established and highly useful method to obtain recombination data for different energy regimes [2]. Since neon is one of the most abundant elements in the universe we proposed a measurement of low-energy DR on Ne^{3+} .

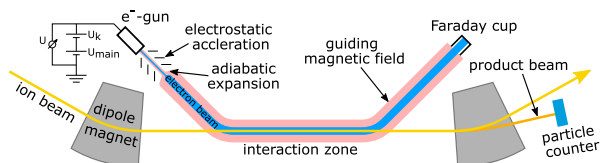


Figure 1: DR measurement setup at the electron cooler.

The experiment was carried out at the CRYRING@ESR ion storage ring at GSI in Darmstadt. At the ring's electron cooler, an ultra-cold electron beam can be merged with the circulating ion beam and recombination observed in merged-beam configuration. The low temperature of the electron beam enables high-precision measurements of DR using a dedicated setup to change the electron energy in discrete steps. The down-charged ions are detected by a scintillation particle detector placed behind the ring dipole

* e.menz@hi-jena.gsi.de

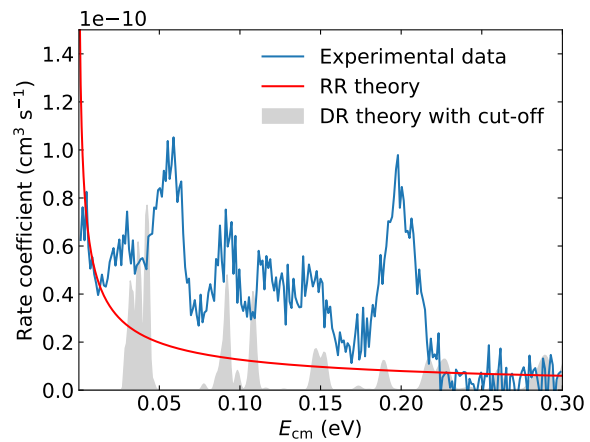


Figure 2: $\Delta n=0$ DR spectrum for $\text{Ne}^{3+} + e^- \rightarrow \text{Ne}^{2+}$.

directly following the electron cooler section. In this position the product beam – owing to the altered charge state – is well separated from the stored beam. Figure 1 shows the measurement setup.

We were granted 10 days of beamtime in November/December 2023 and were able to measure DR resonances in the low-energy. Some of the results are shown in Figure 2. Ne^{3+} is an ion in a N-like configuration and recombines into O-like Ne^{2+} . We note that Ne^{3+} shows some very strong, low-lying DR resonances at energies below 0.5 eV with expected merged-beam recombination rate coefficient almost as strong as near the series limit. This group originates from a $2s^2 2p^3 \ ^2D_J$ 5l transition set. The light grey area shows the AUTOSTRUCTURE theoretical calculations taking modelled field ionisation effects into account.

Detailed analysis of the data is currently ongoing and we have since been able to complete another measurement – on S^{3+} – which also falls within our programme of astrophysically motivated DR experiments.

References

- [1] N. R. Badnell *et al.*, *Astrophys. J.* **804**, 100 (2015).
- [2] D. W. Savin, *J. Phys.: Conf. Ser.* **88**, 012071 (2007).

High brightness ion sources for strong-field laser and other applications

F. Machalett^{*1,2,3}, B. Ying^{1,2}, A. Sommerfeld², S. Lippmann⁴, Th. Stöhlker^{1,2,3}, and G. G. Paulus^{1,2}

¹Helmholtz Institute Jena, Fröbelstieg 3, 07743 Jena, Germany; ²Institute of Optics and Quantum Electronics, Friedrich Schiller University Jena, 07743 Jena, Germany; ³GSI Helmholtz-Zentrum für Schwerionenforschung, 64291 Darmstadt, Germany; ⁴Otto Schott Institute of Materials Research, Friedrich Schiller University Jena, 07743 Jena, Germany

Based on our previous studies in strong-field laser physics, we continued with improving the liquid metal ion sources (LMIS) and their source substances, with a view to further studies of laser-ion interaction. The dissociation of molecular ions and the generation of higher charge states are of special interest. We began application research for these brilliant ion sources. This includes the development of flexible ion emitters and a better adaption to other ion optics.

We have improved the preparation of the ion emitters for LMIS [1] and the accuracy of their mounting and microscopic fine adjustment in the source housing relative to the ion optical axis of the further optical elements. For the preparation of the source feed materials we used a vacuum induction furnace to melt the components and to form a eutectic system, in this case $\text{Au}_{82}\text{Si}_{18}$.

For the strong-field laser experiments, we used the high-brightness LMIS to the ion laser system for 3D coincidence momentum spectroscopy (Fig.1). With a Wien filter in the beamline, different ion species could be selected: Si^+ , Si^{2+} , Au^+ , Au^{2+} , Au_2^+ , Au_3^+ and Au_3^{2+} . Monoatomic and noble metal molecular ions can be used to carry out studies on the ultrafast laser-induced fragmentation and ionization.[2]

Fig.2(a) shows the emitter needle wetted with a molten Au-Si alloy. In Fig.2(b) are shown the different ionization processes in the plasma in front of the Taylor cone. In consideration of these processes with different charge states, masses and molecules, it is remarkable that such steps with high stability can occur (Fig.3). This result could open up the possibility of a controlled and defined pulsating field emission of the brilliant LMIS.

Our results show that LMIS makes accessible a broad range of ion species for experiments in strong-field physics. Further possible applications of LMIS will be, for example, the provision of ions for EBIT.

The authors acknowledge funding from the Deutsche Forschungsgemeinschaft (Priority program 1840). We thank the IBC at HZ Dresden-Rossendorf e.V. for support at the earlier experiments.

References

[1] F. Machalett, P. Seidel, Focused Ion Beams and Some Selected Applications, EAP, Wiley (2019)

*f.machalett@gsi.de

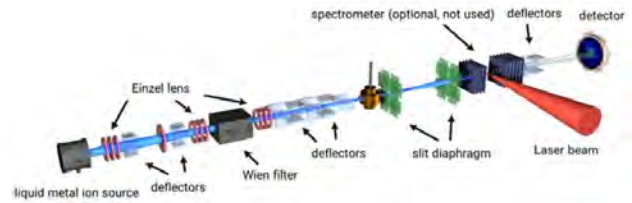


Figure 1: Femtosecond laser pulses are focused onto a 8 keV ion beam of the LMIS. The dissociation fragments are detected by a time-and position-sensitive detector.[2]

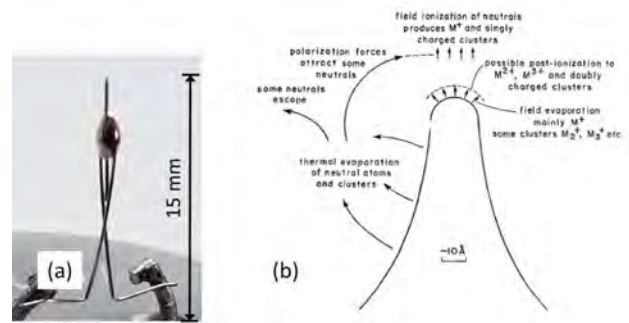


Figure 2: (a) Ion emitter wetted with a liquid alloy and the tungsten needle tip. (b) Liquid protrusion on top of the needle tip, formed by the electric field in nm-dimensions and with different ionization processes. [3].

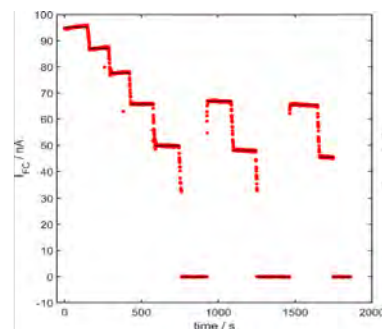


Figure 3: Adjustable stable ion current emitted from the LMIS by stepwise variation of the extraction voltage, without any additional stabilizing or suppressor electrode or electronics. Extr. volt.: 7 kV-6.5 kV. Heater curr.: 6.4 A.

[2] B. Ying, *et al.*, J. Phys. B: At. Mol. Opt. Phys. **54** (2021)

[3] D. R. Kingham, L. W. Swanson, (1984). J. de Physique, C9 Suppl. 12, C9-133.

THEORY

Two-beam laser photon merging

Chantal Sundqvist^{1,2} and Felix Karbstein^{*1,2}

¹Helmholtz Institute Jena, Germany; ²Theoretisch-Physikalisches Institut, FSU Jena, Germany

Quasi-elastic scattering processes have long been thought of providing the most promising signal for a first experimental detection of quantum vacuum non-linearity. A prominent example of such a process is vacuum birefringence. However, these signals are typically strongly background dominated. This problem can be circumvented by inelastic scattering processes. In this study, we investigate the inelastic process of laser photon merging in the collision of just two laser pulses under a finite angle, which provides signal photons of a distinct frequency outside the frequency spectrum of the background. As a key result, for the example of two laser beams of the same oscillation frequency we demonstrate that by using high-intensity optical lasers and choosing an optimal collision angle, photon merging should become accessible in experiment with state-of-the-art technology. In this case three frequency ω laser photons are merged to a single 3ω photon.

The nature of the quantum vacuum is governed by quantum fluctuations allowing electromagnetic fields to interact nonlinearly by the coupling to virtual electron-positron pairs [1]. However, these effective couplings are parametrically suppressed by powers of $|\vec{E}|/E_{\text{cr}}$ and $|\vec{B}|/B_{\text{cr}}$ with the critical electric (magnetic) field strength $E_{\text{cr}} \simeq 1.3 \times 10^{18}$ V/m ($B_{\text{cr}} \simeq 4 \times 10^9$ T). This has so far prevented the direct observation of quantum vacuum signatures under controlled laboratory conditions. With ongoing advances in laser technology and the building of new dedicated high-intensity laser facilities, a particularly promising route to an experimental verification of quantum vacuum nonlinearity is provided by all-optical pump-probe type setups. The attainable photonic signatures in this type of experiment can be divided in two main classes, namely *quasi-elastic* and manifestly *inelastic* processes.

Quasi-elastic processes depend only on the oscillation frequency of one of the driving beams. This results in signal photons with kinematic properties very similar to the probe photons. Generically, quasi-elastic processes provide satisfactory large signal photon numbers which however contend with the large background of the driving lasers. Typically, *inelastic* processes are suppressed relatively to elastic ones. On the upside, the emission direction and energy of the signal photons arising from these processes often differ significantly from those constituting the driving laser beams.

So far, the great potential of inelastic quantum vacuum signatures for all-optical experiments has mainly been exemplified in scenarios involving more than two laser

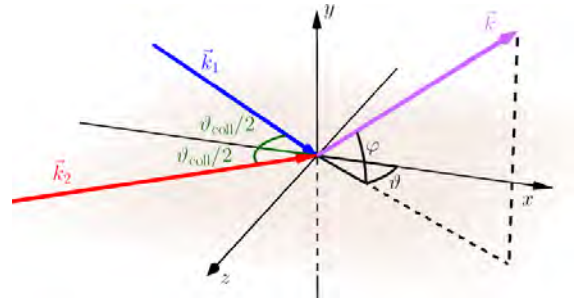


Figure 1: Sketch of the collision geometry. The wave vectors of the two colliding laser pulses are \vec{k}_1 , \vec{k}_2 . The collision takes place in the xz -plane under a collision angle ϑ_{coll} . The wave vector of the signal photons is \vec{k} and parameterized by the angles φ , ϑ .

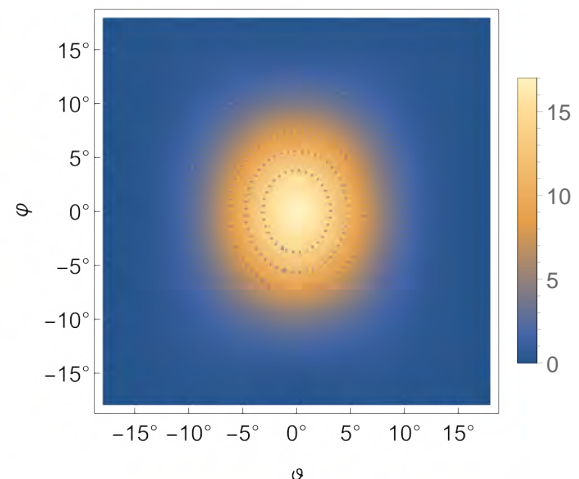


Figure 2: Angular distribution of the 3ω signal for the collision of two HPLS pulses at $\vartheta_{\text{coll}} \approx 50.2^\circ$.

beams. In Ref. [2], we provide a thorough analysis of the effect of laser photon merging in the collision of just two laser pulses at zero impact parameter. To this end, we analyze the emission characteristics of the merged signal photons in a scenario envisioning the collision of two laser beams under a finite angle; see Figs. 1 and 2.

This work has been funded by the DFG under Grant No. 416607684 within the Research Unit FOR2783/2.

References

- [1] W. Heisenberg and H. Euler, Z. Phys. **98**, 714 (1936).
- [2] C. Sundqvist and F. Karbstein, Phys. Rev. D **108**, 056028 (2023).

*f.karbstein@hi-jena.gsi.de

Bayesian optimization of quantum vacuum signals

M. A. Valialshchikov^{*1}, F. Karbstein¹, D. Seipt¹, and M. Zepf¹

¹HI Jena, Fröbelstieg 3, 07743 Jena, Germany

Modern high-intensity laser facilities allow to plan and perform first light-by-light scattering experiments which require higher accuracy theoretical predictions and investigation of high-dimensional parameter spaces. To meet those requirements, we use numerical simulations and Bayesian optimization to maximize the quantum vacuum signal. We find the optimal waist sizes for beams with elliptic cross sections and determine the origin of discernible signature in a coherent harmonic focusing scenario.

According to strong-field QED, a high-intensity electromagnetic field in vacuum acts as a nonlinear medium which might alter frequency, wavevector and polarization of incoming photons. For currently available laser technology the total signal is weak (only a few photons) compared to huge laser background. This motivates the search for optimal collision configurations resulting in promising discernible signatures that could be potentially detected in the experiment. Theoretical studies provided many insights but they are limited by the use of simplified beam profiles. Using numerical Maxwell solvers helps to overcome this limitation but requires a lot of computational resources.

In the vacuum emission picture [1], the zero-to-single photon (with wavevector \mathbf{k} , energy $\omega = |\mathbf{k}|$ and polarization vector $\epsilon_{(p)}^\mu$) transition amplitude is given by

$$S_{(p)}(\mathbf{k}) = \frac{\epsilon_{(p)}^{*\mu}(k)}{\sqrt{2k^0}} \int d^4x e^{ik_\nu x^\nu} j_\mu(x) \Big|_{k^0=\omega}, \quad (1)$$

where

$$j_\mu(x) = 2\partial^\nu \frac{\partial \mathcal{L}_{\text{HE}}}{\partial F^{\nu\mu}} \quad (2)$$

is the signal-photon current generated by the external macroscopic electromagnetic fields $F^{\mu\nu}$ and \mathcal{L}_{HE} is the Heisenberg-Euler Lagrangian.

To calculate the quantum vacuum signal, we use the numerical code ‘‘VacEm’’ [2] that employs 1) a linear Maxwell solver describing the dynamics of the external electromagnetic field and 2) the vacuum emission picture defining the transition amplitude in Eq. (1). By comparing the signal photon spectrum with the laser background we calculate the total discernible signal and maximize it with the help of Bayesian optimization.

Figure 1 shows grid simulation and optimization results for the collision of two optical pulses. The probe has variable elliptic waist sizes $(\mu_{x,y})$ defining the 2-dimensional parameter space. In general, one has to study the full parameter space to find the true optimum (cf. white dashed

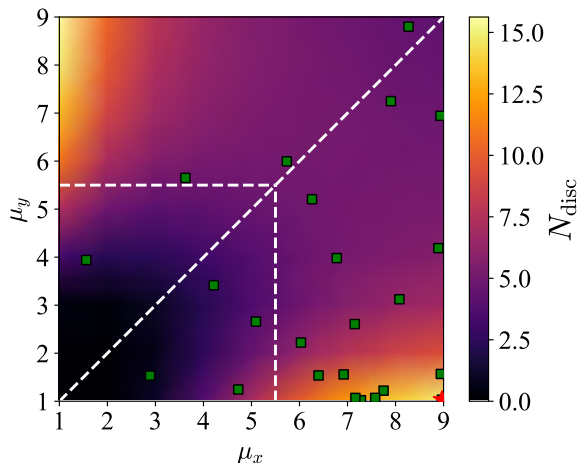


Figure 1: Number of discernible signal photons as a function of the two independent waist sizes for a probe with elliptic cross section. The results presented here are for two beams (energy $W = 25$ J, duration $\tau = 25$ fs each) of frequency ω_0 colliding at an angle of $\vartheta_{\text{col}} = 160^\circ$. Pump (probe) has circular (elliptic) waist with constant (variable) value. The dashed white lines mark the one-dimensional parameter regions studied in [3], green squares correspond to optimization trials, and the red star highlights the optimal waist size found from optimization. Figure is adapted from Ref. [4].

lines in Fig. 1). However, already for two free parameters the grid scan requires a lot of computational resources: 9x9 parameter grid resulting in 81 simulations compared to only 24 simulations with optimization.

In [4] we study the collision of beams with elliptic cross sections in more detail, benchmarking the optimization procedure and demonstrating its advantage over the grid scan simulations. Additionally, we showcase how optimization could be used to efficiently test hypotheses in the coherent harmonic focusing scenario.

We developed the package [5] to obtain the results presented in the article.

References

- [1] F. Karbstein *et al.*, Phys. Rev. D **91**, 113002 (2015).
- [2] A. Blinne *et al.*, Phys. Rev. D **99**, 016006 (2019).
- [3] H. Gies *et al.*, Phys. Rev. D **106**, 116005 (2022).
- [4] M. Valialshchikov *et al.*, arXiv:2405.03317
- [5] <https://github.com/maxbalrog/light-by-light>

^{*}maksim.valialshchikov@uni-jena.de

Exploring new states of matter with a photonic emulator

Felix Karbstein^{*1,2}, Simon Stützer³, Holger Gies^{1,2}, and Alexander Szameit³

¹Helmholtz Institute Jena, Germany; ²Theoretisch-Physikalisches Institut, FSU Jena, Germany; ³Institute of Applied Physics, FSU Jena, Germany; ⁴Institute of Physics, University of Rostock, Germany

We implement the equation of motion of the large- N Gross-Neveu model from strong interaction physics in photonic waveguide arrays and study one of its paradigmatic multi-fermion bound state solutions in an optical experiment. The present study constitutes an important first step towards waveguide-based simulations of phenomena relevant for high-energy physics.

In recent years, earlier speculations about the existence of new states of fermionic matter in the form of inhomogeneous phases where translational invariance is spontaneously broken have turned into a firm theoretical prediction for certain low-dimensional, exactly solvable field theories such as the Gross-Neveu model [1]. Similar phenomena have been predicted and extensively studied in a wide variety of research fields, ranging from condensed-matter systems, via ultracold atomic gases and nuclear physics to quark matter at highest densities.

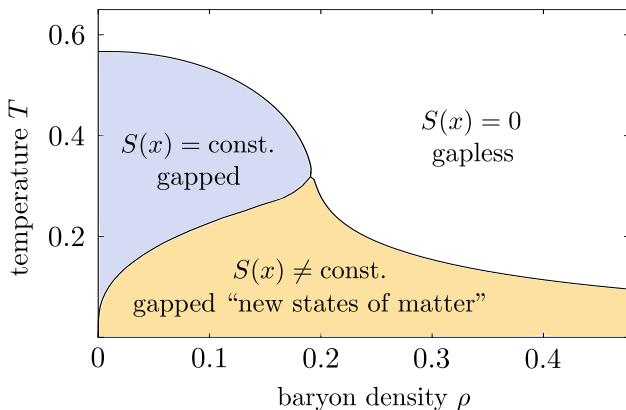


Figure 1: Phase diagram of the theory. New states of matter characterized by $S(x) \neq \text{const.}$ arise for small temperatures [4].

Modern optics and photonics is driven by the fact that photons can be coherently controlled in space and time at the highest precision level. This goes hand in hand with recent developments in precision fabrication and design of optical systems. A prominent example is given by waveguide arrays [2] that can be designed as photonic analogues of systems governed by complex wave equations, including even quantum mechanical equations such as the relativistic Dirac equation. Appropriately designed photonic waveguide arrays with alternating refractive indices of adjacent lattice sites have already proved their capability to emulate a variety of relativistic phenomena. Since the Dirac equation governs the dynamics of almost all known matter

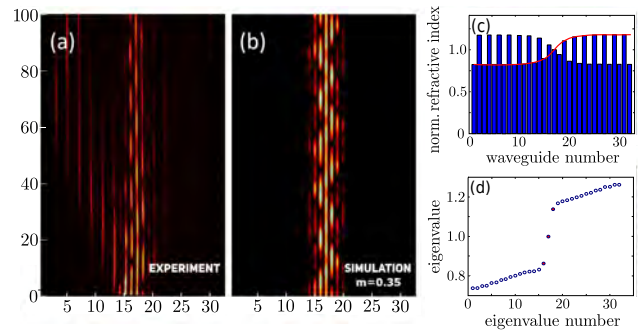


Figure 2: (a) Experimental light dynamics in the photonic structure. Clearly, the beam is localized, which emulates the valence state in the GN model. (b) Numerical confirmation of the experimental results. (c) Normalized refractive index of the individual waveguides (blue) and corresponding scalar potential (red). (d) Eigenvalue diagram of the implemented photonic structure. Clearly, the GN valence state at the kink is visible in the middle of the gap (in red). Besides, the photonic structure supports two additional localized states at the edge of the band gap (also in red).

particles in the universe at the microscopic level, photonics has the potential to explore states of fermionic matter in an unprecedented way.

In Ref. [3], we present a photonic emulator for the physics of relativistic fermion systems and apply it to the massless Gross-Neveu model in the large- N limit [1]. Remarkably, at low temperatures T the latter favors a ground state where translational symmetry is spontaneously broken. This manifests itself in a spatially inhomogeneous scalar condensate, or equivalently a coordinate dependent fermion mass; see Fig. 1. As exact solutions are available for both the condensate shape and the full Dirac spectrum [4], one of those can be used as a paradigmatic example for mapping the Dirac equation in an inhomogeneous condensate onto photonic waveguide arrays; see Fig. 2.

This work has been carried out within the framework of the ACP Explore project “Enlightening New States of Matter” of the Abbe Center of Photonics (ACP).

References

- [1] D. J. Gross and A. Neveu, Phys. Rev. D **10**, 3235 (1974).
- [2] S. Longhi, Laser Photon. Rev. **3**, 243 (2009).
- [3] F. Karbstein, S. Stützer, H. Gies and A. Szameit, Phys. Rev. Res. **5**, L042036 (2023).
- [4] M. Thies and K. Urlichs, Phys. Rev. D **67**, 125015 (2003).

*f.karbstein@hi-jena.gsi.de

Laser Resonance Chromatography of $^{229}\text{Th}^{3+}$ in He: an ab initio investigation

G. Visentin^{*1,2}, A. Borschevsky³, L.A. Viehland⁴, S. Fritzsche^{1,2,5}, and M. Laatiaoui^{6,7}

¹HI Jena, Fröbelstieg 3, 07743 Jena, Germany; ²GSI Helmholtzzentrum für Schwerionenforschung, 64291 Darmstadt, Germany; ³Van Swinderen Institute for Particle Physics and Gravity, University of Groningen, Nijenborgh 4, 9747 Groningen, The Netherlands; ⁴Science Department, Chatham University, Pittsburgh, Pennsylvania 15232, USA; ⁵Theoretisch-Physikalisches Institut, Friedrich-Schiller-Universität Jena, D-07743 Jena, Germany; ⁶HI Mainz, Staudingerweg 18, 55128 Mainz, Germany; ⁷Department Chemie, Johannes Gutenberg-Universität, Fritz-Strassmann Weg 2, 55128 Mainz, Germany,

We propose a laser resonance chromatography (LRC) experiment on $^{229}\text{Th}^{3+}$, with the goal of detecting the ion's electronic ground $5f\ ^2F_{5/2}$ state and metastable $7s\ ^2S_{1/2}$ state by means of their ion mobilities in He. To this end, we first accurately model the ion-neutral interaction potentials for the two electronic states. The interaction potentials are used to simulate the state-specific reduced ion mobilities in terms of the operating temperature and the external electric field. The ion mobilities differ by more than 7% at 300 K and moderate field strengths; thus, separation of the $^{229}\text{Th}^{3+}$ metastable state lies within the reach of LRC experiments targeting optical probing and monitoring of the nuclear clock transition in this isotope.

$^{229}\text{Th}^{3+}$ is nowadays considered the most promising candidate for a nuclear clock of unprecedented accuracy based on a low-lying and relatively long-lived nuclear transition from the nuclear isomer state at about 8.338(24) eV. This charge state features a relatively simple electronic structure that enables closed two- and three-level systems for laser-probing and cooling at the same time, and exhibits a laser-accessible $7s\ ^2S_{1/2}$ metastable state and with 1s lifetime immune to field-induced frequency shifts. Due to these features, laser-pumping schemes were proposed to populate the $7s\ ^2S_{1/2}$ electronic state and exploit it to monitor the nuclear clock transition [1].

Here, we theoretically explore the application of Laser Resonance Chromatography (LRC) [2] for fast laser probing of a single isolated $^{229}\text{Th}^{3+}$ ion in the $7s\ ^2S_{1/2}$ electronic state without the need for fluorescence detection. LRC specifically targets the investigation of heavy and superheavy ions, and characterizes them by means of their transport properties in buffer gases. A LRC experiment consists of a spectroscopic step, where the ions are laser-excited to a dark long-living metastable state, and a chromatographic step, where the ions in the ground and metastable states are driven through a drift tube filled with a He buffer gas and separated by means of their different transport properties (drift times). In particular, we propose to use LRC to separate the electronic $7s\ ^2S_{1/2}$ state of $^{229}\text{Th}^{3+}$, by simulating the chromatographic step of the experiment. To this end, accurate ion-atom interaction potentials for the two aforementioned electronic states were computed and used

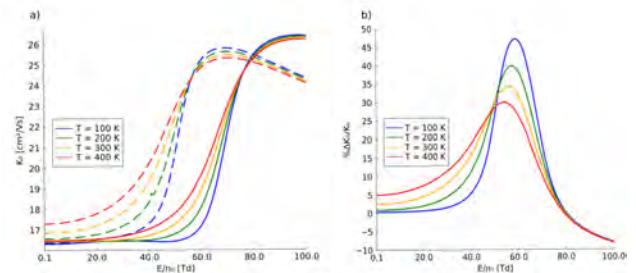


Figure 1: a) Reduced mobilities of the $^{229}\text{Th}^{3+}$ -He dimer in the ground $5f\ ^2F_{5/2}$ state (full lines) and metastable $7s\ ^2S_{1/2}$ state (dashed lines) as a function of the reduced electric field; b) relative difference between the reduced zero-field mobilities of the ground and metastable states as a function of the reduced electric field. The reduced ion mobilities are reported for four operating temperatures: 100 K (blue lines), 200 K (green lines), 300 K (orange lines) and 400 K (red lines).

to calculate the state-specific reduced (standard) ion mobilities over a wide range of gas temperatures and external electric field strengths, to determine the operating temperatures and field strengths that ensure state-separation. The state-specific reduced ion mobilities differ by more than 7% in a temperature and reduced electric field ranges between 300 and 400 K, and 18 and 28 Td (1 Td = 10^{-17} Vcm²), respectively, as shown in Figure 1. These boundary conditions suit the operability of LRC and should enable effective state-separation, albeit further experimental investigations are needed to quantify collisional quenching rates of the metastable state. Our investigation shows that LRC is a suitable technique to characterize the $7s\ ^2S_{1/2}$ electronic state that is needed for the interrogation of the ^{229}Th nuclear clock transition, and, thus, may be integrated with experimental facilities devoted to the investigation of Th-based nuclear frequency standards.

References

- [1] E. Peik and C. Tamm, *Europhysics Letters* **61**, 181 (2003).
- [2] M. Laatiaoui, A. A. Buchachenko, and L. A. Viehland, *Phys. Rev. Lett.* **125**, 023002 (2020).

*g.visentin@hi-jena.gsi.de

Comparison of theory and experiment for radiative characteristics in Tm I

A. Bondarev^{*1,2}, M. Tamanis³, R. Ferber³, G. Başar⁴, S. Kröger⁵, M. Kozlov, and S. Fritzsche^{1,2,6}

¹Helmholtz Institute Jena, Germany; ²GSI Helmholtzzentrum für Schwerionenforschung, Darmstadt, Germany; ³University of Latvia, Riga, Latvia; ⁴Istanbul University, Türkiye; ⁵Hochschule für Technik und Wirtschaft Berlin, Germany; ⁶Friedrich Schiller University, Jena, Germany

Intensities in the neutral thulium emission series originating from a common upper level are measured using a Fourier transform spectrometer. The derived relative transition probabilities within each series are compared to the theoretical predictions obtained from large-scale calculations that combine configuration interaction with many-body perturbation theory. Our theoretical results well describe the current measurements and show no more than a two-fold difference from previous experimental data on absolute transition probabilities. Additionally, Landé g factors, hyperfine structure constants, and atomic electric quadrupole moments for several levels of interest are computed and compared to experimental observations, where available.

In this study, we analyze the FT spectrum of neutral thulium within the visible spectral range. From this spectrum we determine the relative intensity distributions in branches that originate from a common upper level. In our current investigation we identify new branches that were not reported in Refs. [1, 2]. Our experimental findings are compared to theoretical outcomes derived using a method that combines the configuration interaction with many-body perturbation theory [3, 4]. As a result of these large-scale calculations, we obtain predictions for level energies, Landé g factors, hyperfine structure constants, probabilities of electric dipole transitions, and atomic electric quadrupole moments. To check the predictive power of the theory, we compared the respective characteristics with their experimental values available from previously published sources. Such comparisons are very important for further developing theoretical approaches for ions with complex electronic structure, in particular those with an open f -shell. Accurate predictions of the transition probabilities in elements with complex electronic structure are of current interest in astrophysics [5].

In Fig. 1 relative intensity distributions in two series of lines originating from common upper levels are presented. The experimental and theoretical results are reasonably consistent with each other and align with the expectations of a simplified one-electron model. For example, consider the series with the upper level $(4f^{13}(^2F_{7/2}^o)6s7s(^3S_1))_{9/2}^o$ at $32\,217.195\text{ cm}^{-1}$ (panel (a)). The strongest transition corresponds to an effectively one-electron $7s \rightarrow 6p$ transition, while conserving the total angular momentum J . Following that, the second strongest transition is also the same one-electron transition but with a change in J from $9/2$ to $7/2$. The weaker transitions involve effectively two-

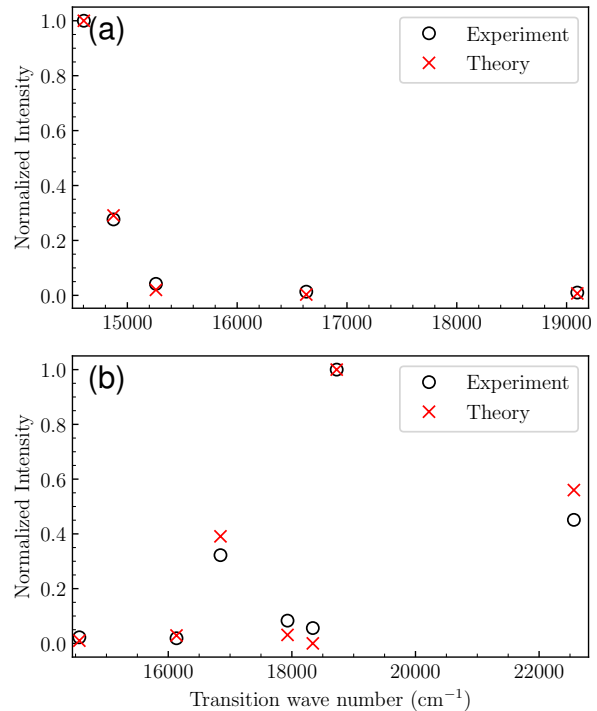


Figure 1: Comparison of experimental and theoretical intensity distributions of emission lines originating from a common upper level at energies: (a) $32\,217.195\text{ cm}^{-1}$, and (b) $35\,682.251\text{ cm}^{-1}$.

electron processes: $(7s, 4f) \rightarrow (6s, 5d)$ transitions. The full set of experimental and theoretical data can be found in [6].

References

- [1] M. E. Wickliffe and J. E. Lawler, *J. Opt. Soc. Am. B* **14**, 737 (1997).
- [2] X. Wang *et al.*, *Journal of Quantitative Spectroscopy and Radiative Transfer* **280**, 108091 (2022).
- [3] V. A. Dzuba, V. V. Flambaum, and M. G. Kozlov, *Phys. Rev. A* **54**, 3948 (1996).
- [4] M. G. Kozlov, I. I. Tupitsyn, A. I. Bondarev, and D. V. Mironova, *Phys. Rev. A* **105**, 052805 (2022).
- [5] A. Bondarev, J. Gillanders, C. Cheung, M. Safronova, and S. Fritzsche, *The European Physical Journal D* **77**, 126 (2023).
- [6] A. I. Bondarev, M. Tamanis, R. Ferber, G. Başar, S. Kröger, M. G. Kozlov, and S. Fritzsche, *Phys. Rev. A* **109**, 012815 (2024).

* a.bondarev@hi-jena.gsi.de

Coulomb excitation of hydrogen atoms by vortex ion beams

Anna V. Maiorova^{1,2}, Dmitry Karlovets, Stephan Fritzsche^{1,2,3}, Andrey Surzhykov^{4,5,6}, and Thomas Stöhlker^{1,2,7}

¹HI Jena, Jena, Germany; ²GSI, Darmstadt; ³TPI, FSU Jena; ⁴PTB, Braunschweig; ⁵TU Braunschweig; ⁶Laboratory for Emerging Nanometrology Braunschweig; ⁷IOQ, FSU Jena

The Coulomb excitation of target atoms by Laguerre–Gaussian ionic wave packets has been theoretically studied. The general expressions for the total excitation probability and the alignment parameter of an excited atom were derived in the framework of the non–relativistic first–Born approximation. Special attention is paid to the effect of an orbital angular momentum (OAM) projection of projectile ions on the population of magnetic sublevels of an excited atom and, consequently, on the angular distribution of fluorescence radiation. It was shown that both of these characteristics are very sensitive to the OAM projection carried by the projectile ions.

Investigations of vortex states of light and matter have a rich history of more than thirty years. Particles, prepared in such states, can carry a non–zero projection l_{OAM} onto their propagation direction. A number of studies have been done during last few decades on vortex states of photons [1], electrons [2], neutrons [3], atoms and even molecules [4]. A natural extension of the above–mentioned research is positively–charged *ions* in accelerators and storage rings. The OAM projection of vortex ions will provide an additional degree of freedom for collision studies in atomic physics. However, the realization of such experiments requires the development of techniques for production and diagnostics of vortex ions. The analysis of fundamental atomic processes, induced in collisions with vortex ions can give us a promising approach for the OAM–diagnostics. For this reason we present theoretical studies of the Coulomb excitation of a hydrogen atomic target by Laguerre–Gaussian [5] protons to demonstrate the sensitivity of the characteristics of this process to the OAM projection and, as a consequence, the possibility of its application to verify ion beam vorticity.

In our study, we focus on the $1s \rightarrow 2p$ excitation of hydrogen atoms due to the Coulomb interaction with Laguerre–Gaussian projectile protons, $H(1s) + H_{LG}^+ \rightarrow H(2p) + H^+$. We showed that in this process the anisotropy of the $2p \rightarrow 1s$ emission is rather sensitive to the l_{OAM} of projectile ions. This sensitivity is reflected by the OAM–dependence of the effective excitation cross section $\tilde{\sigma}_{tot}$ and the effective alignment parameter \tilde{A}_{20} , that is displayed in Fig. 1. The most pronounced anisotropy of fluorescence emission can be observed for Coulomb excitation of the hydrogen target by protons, carrying the OAM projection $l_{OAM} = 4$, for which $\tilde{A}_{20} = -0.9240$. In contrast, the excitation of the macroscopic hydrogen target by the Gaussian beam with $l_{OAM} = 0$ leads to the effective alignment $\tilde{A}_{20} = -0.6229$ and, hence,

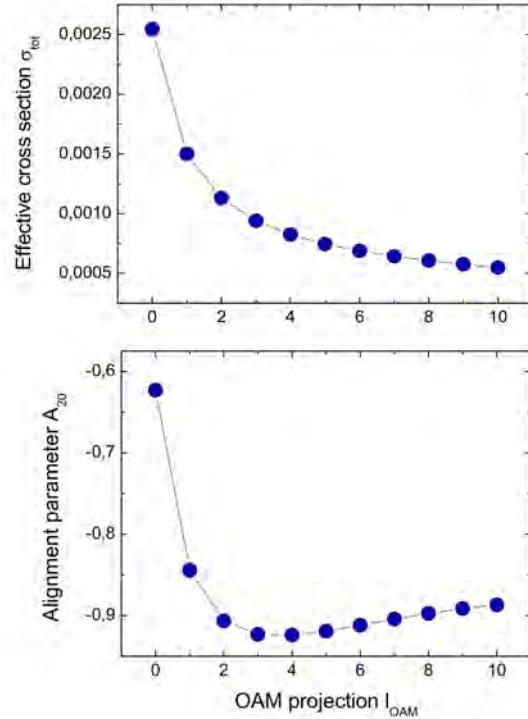


Figure 1: Effective excitation cross section $\tilde{\sigma}_{tot}$ (top panel) and alignment parameter \tilde{A}_{20} (bottom panel) for the macroscopic hydrogen target, bombarded by the LG proton wave packet with the energy $T_p = 5$ MeV/u and transverse width $\sigma_{\perp} = 100$ a.u. Results are presented for various OAM projections.

to a weaker anisotropy of the radiation pattern. This variation of the $2p \rightarrow 1s$ angular distribution for different OAM projections can easily be observed with the modern detectors and can open a very promising avenue for the diagnostics of vortex ion beams in accelerator and storage ring experiments

References

- [1] L. Allen *et al.*, Phys. Rev. A **45**, 8185 (1992).
- [2] M. Uchida and A. Tonomura, Nature **464**, 737 (2010).
- [3] Ch.W. Clark *et al.*, Nature **525**, 504 (2015).
- [4] A. Luski *et al.*, Science **373**, 1105 (2021).
- [5] D. Karlovets, Phys. Rev. A **98**, 012137 (2018).

Tracing the effects of fundamental frequencies in laser pulses on electron momentum and ionization

Danish Furekh Dar * and Stephan Fritzsche

Helmholtz-Institut Jena, Fröbelstieg 3, D-07743 Jena, Germany

Strong-field ionization is fundamental for studying the complex dynamics in atoms, molecules, and solids under intense optical fields [1]. Progress in laser technology has enabled the generation of few-cycle pulses, vital for examining ultra-short scale dynamics. These pulses affect the photoelectron momentum distribution (PMD), which varies with pulse shape and carrier-envelope phase (CEP). By applying the strong field approximation (SFA) or Keldysh-Faisal-Reiss (KFR) theory [2, 3, 4], we analyze the interference in PMD and ionization spectra caused by the short few cycle intense pulses.

The Volkov state, denoted by $\chi_{\mathbf{p}}(\mathbf{r}, \tau)$, provides an approximation for the quantum state of a charged particle under the influence of an external laser field. The expression for the Volkov state is given by $\chi_{\mathbf{p}}(\mathbf{r}, \tau) = (2\pi)^{-3/2} e^{-iS_v(\tau)} e^{i\mathbf{p}\cdot\mathbf{r}}$, where \mathbf{p} represents the momentum of the particle, \mathbf{r} is the position vector, and τ is the time variable. Here, $S_v(\tau)$ represents the Volkov phase, which accounts for the interaction between the particle and the laser field, and is defined as $S_v(\tau) = \frac{1}{2} \int^{\tau} dt' [\mathbf{p} + \mathbf{A}(t')]^2$, with $\mathbf{A}(t')$ being the vector potential of the laser field at time t' . This phase factor incorporates the effects of the electromagnetic field on the particle's dynamics. The Volkov phase $S_v(\tau)$ for a circularly polarized pulse with \sin^2 envelope can be succinctly expressed as [5]:

$$S_v(\tau) = \epsilon_p \tau + \frac{A_0^2}{4} \int^{\tau} dt' f^2(t') + \sum_{j=-1}^1 \frac{A_j p \sin \theta_p}{\sqrt{2}} \int^{\tau} dt' \cos(\omega_j t' + \beta), \quad (1)$$

where $\beta = \phi_{\text{cep}} - \Lambda \varphi_p$ and $\epsilon_p = \frac{p^2}{2}$. The terms represent contributions from the asymptotic energy, the electron's ponderomotive energy within the laser pulse, and the momentum due to interaction with the laser's frequency components (ω_j), referred to as the envelope energy and nonlinear response, respectively.

As shown in Figure 1, the energy and momentum distributions for laser pulses of 2, 4, and 8 optical cycles are presented. This visualization includes the ionization spectra, characterized by peaks corresponding to concentric rings at $p_z = 0$ within the PMD. Notably, the spectrum's extremities, represented by the innermost and outermost rings, show photoelectrons at their minimum and maximum kinetic energies, typically appearing with lower probabilities.

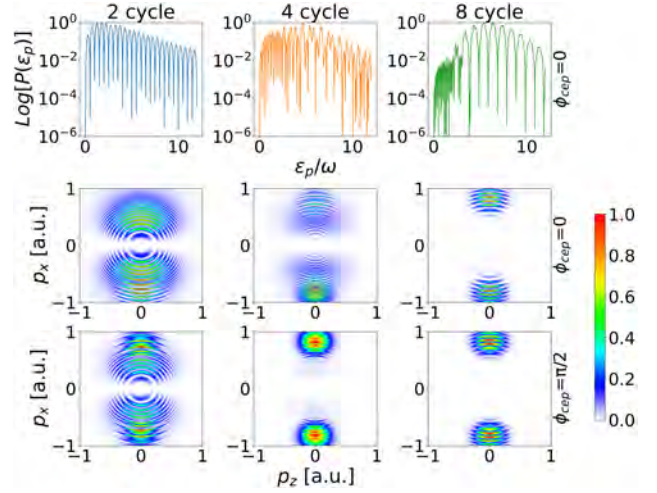


Figure 1: Ionization spectra and PMD for \sin^2 driving laser pulses across 2, 4, and 8 optical cycles (left to right columns).

The most prevalent features in these distributions are photoelectrons with kinetic energies that are neither minimal nor maximal.

Subsequent examination of the PMD in Figure 1 indicates a trend where increasing the number of optical cycles leads to a fading of the inner rings and an expansion of the outer rings. This behavior is mirrored in the ionization spectra, where the rings not only broaden but also develop subtle oscillations at higher photoelectron energies as the pulse cycle count rises. This phenomenon can be elucidated using Eq. 1, which explains that increased photoelectron momentum (p) enhances the nonlinear effects due to electron interactions with fundamental frequencies, while these interactions are negligible at lower momenta. This results in peak broadening in the ionization spectra, attributed to electron interference with the fundamental frequencies.

This research has received funding from the Research School of Advanced Photon Science (RS-APS) at the Helmholtz Institute Jena, Germany.

References

- [1] P. B. Corkum and F. Krausz, *Nature Physics* **3**, 381 (2007).
- [2] L. V. Keldysh, *Sov. Phys. JETP* **20**, 1307 (1964).
- [3] F. H. M. Faisal, *J. Phys. B* **6**, L89 (1973).
- [4] H. R. Reiss, *Phys. Rev. A* **22**, 1786 (1980).
- [5] D. F. Dar and S. Fritzsche, *Phys. Rev. A* **109**, L041101 (2024).

* danish.dar@uni-jena.de

Partial-wave representation of the strong-field approximation — length versus velocity gauge

F. Liu^{*1,2,3}, S. Fritzsche^{1,2,3}, and M. Kübel^{1,2,4}

¹Helmholtz Institute Jena, Fröbelstieg 3, 07743 Jena, Germany; ²Theoretisch-Physikalisches Institut, Friedrich-Schiller-Universität Jena, 07743 Jena, Germany; ³GSI Helmholtzzentrum für Schwerionenforschung GmbH, 64291 Darmstadt, Germany; ⁴Institute of Optics and Quantum Electronics, 07743 Jena, Germany

Here, we report a joint theory-experiment investigation using laser-induced electron diffraction to explore their interplay arising from interaction with the potentials of two-hole states of the xenon cation. With the constructed electron-hole potential, we apply the quantitative rescattering model to calculate the photoelectron momentum distributions (PMD) for high-order above-threshold ionization of xenon using 40-fs laser pulses with a central wavelength of 3100 nm and a peak laser intensity of $6 \times 10^{13} \text{ W/cm}^2$. The simulated PMDs describe well the features of the measured angular distributions of photoelectrons. Moreover, we identify the contributions of these time-evolving hole states to the angular distribution of the rescattered electrons, particularly noting a distinct change along the backward scattering angles.

Laser-induced electron diffraction (LIED) has been established as a powerful alternative to conventional electron diffraction for recent reviews. The technique relies on the laser-driven elastic rescattering of a photoelectron emitted by strong-field ionization, which gives rise to high-order above threshold ionization (HATI), the basic strong-field phenomenon underlying LIED. The rescattering process provides LIED with two interesting properties: first, an ultrahigh current density, allowing imaging on the single molecule level; second, perfect synchronization between ionization and scattering events, allowing (attosecond) time-resolved experiments.

In this work, we consider the Xe atom. The ground state of the Xe cation has two fine-structure components: the $^2P_{3/2}$ and $^2P_{1/2}$ that are separated by $\Delta E_{\text{SO}} = 1.3 \text{ eV}$ due to the spin-orbit interaction. Both ion states are coherently populated by tunnel ionization, thus creating a wave packet. As the spin-orbit wave packet evolves, the $5p^5$ electron-hole (vacancy) in the valence shell oscillates between the $m = 0$ state and the $|m| = 1$ states of the valence shell of the Xe^+ ion with the period $T_{\text{SO}} = h/\Delta E_{\text{SO}} (3.2 \text{ fs})$, where m is the magnetic quantum number[1]. The spatial hole density in the valence shell is described by the orbitals for $m = 0$ (“peanut shape”) and $|m| = 1$ (“donut shape”). At integer and half-integer multiples of the spin-orbit period, the hole alternately populates the $m = 0$ and $|m| = 1$ orbitals, respectively. Here, we employ elastic rescattering in a mid-infrared field ($\lambda = 3100 \text{ nm}$) with an optical period of $T = 10.5 \text{ fs}$. Owing to the relatively long optical period, the returning electron wave packet spans several femtoseconds, allowing us, in principle, to probe the evo-

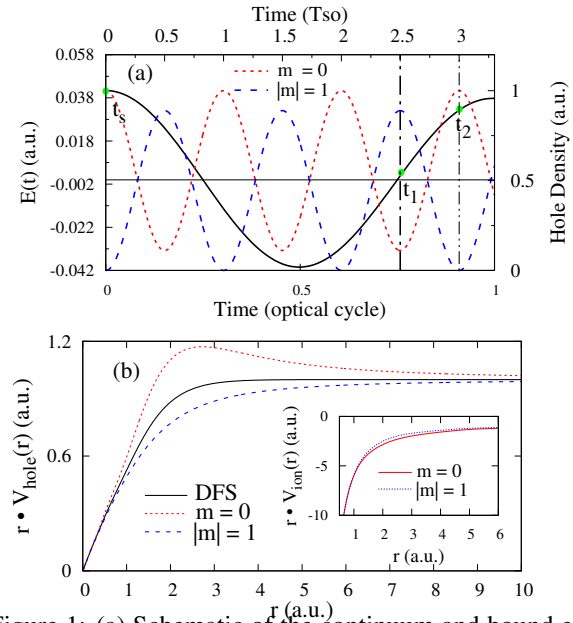


Figure 1: (a) Schematic of the continuum and bound electron dynamics induced by tunnel ionization. The oscillation of the laser electric field (solid black curve) is compared to the hole population for the $m = 0$ (dotted red curve) and $|m| = 1$ (dotted blue curve) vacancy states. The times $t_1 = 2.5 T_{\text{SO}}$ and $t_2 = 3.0 T_{\text{SO}}$ mark times at which the hole populates dominantly the $|m| = 1$ and $m = 0$ states, respectively. (b) Electron-hole potentials (V_{10} and V_{11}) for the $m = 0$ and $|m| = 1$ vacancy states of Xe^+ , and the Dirac-Fock-Slater potential. The inset shows the full scattering potential of the ion.

lution of the spin-orbit wave packet in xenon.

In conclusion, our study reveals that the numerical results allow for the theoretical distinction of electron signals resulting from rescattering off the $m = 0$ and $|m| = 1$ hole states, particularly noting a distinct change along the backward scattering angles. In the future, in order to identify the contributions of the hole states, a more accurate agreement between theory and experiment needs to be obtained.

This work was supported by the Deutsche Forschungsgemeinschaft (DFG, German Research Foundation) under Project No. 440556973 and the Emmy Noether program, project No. 437321733.

References

- [1] H. J. Wörner *et al.*, J. Phys. B **44**, 041001 (2011).

*fang.liu@uni-jena.de

Comparison between velocity and length gauge in strong-field approximation under partial-wave representation

Kefei Zou ^{*1,2,3}, Fang Liu^{1,2,3}, and S. Fritzsche^{1,2,3}

¹HI Jena, Fröbelstieg 3, 07743 Jena, Germany; ²GSI, Darmstadt; ³TPI, FSU Jena

We study the above-threshold ionization (ATI) of noble gases in length and velocity gauge analytically. For this purpose, we implement the partial-wave representation under strong field approximation (SFA). This representation enables us to calculate the differential ionization probability taking into account the electronic orbits easily of the target. Moreover, we derive the gauge transformation and the direct amplitude in both gauges rigorously and analyze the dependence of gauges from equations and from the ATI spectra of the targets. Our results show agreement on both gauges in the hydrogenic-like 1s-state, and gauge dependence at high kinetic energy regime of the electron if the atomic structure of the target is considered.

Analytical theories are necessary for explaining phenomena of strong laser-matter interactions. Compared to ab initio methods and phenomenology studies, analytical approach provides more probabilities to reveal the physics hidden behind the initiate circumstances and phenomena. One of an analytical theories, so-called the strong field approximation (SFA), has been developed and widely used when the field strength of the laser field is reasonably comparable to the atomic binding potential. The perturbation theory therefore cannot describe relatively accurate ionization process while a systematic (perturbative) method has been used to expand the process according to the behavior of the ionized electron. The ATI process thus can be described by the zeroth order where the electron is directly ionized without rescattering with the atomic core. For a review on the SFA development and its history, see [1].

Gauge invariance is a basic requirements of the electromagnetism and quantum theory. This means that the Schrödinger equation of the process should be gauge invariant, and naturally, any physical quantity is gauge independent. In ATI under the SFA, we consider the "ground states-Volkov states" transition where the Volkov state represents a quasi-free state with plane wave and Volkov phase that depends on the electromagnetic field. The ground states and the Volkov states are the eigenstates of the pure atomic Hamiltonian and the laser-electron Hamiltonian (without the atomic potential), respectively. These two incomplete sets of eigenstates does not satisfy the orthogonality $\langle \mathbf{p}|0\rangle \neq 0$ which leads to non-physical results including the gauge dependence of the direct amplitude $T_0(\mathbf{p}) = -i \int_{-\infty}^{\infty} d\tau \langle \chi_{\mathbf{p}}(\tau) | V_{ie}(\mathbf{r}, t) | \Psi_i(\tau) \rangle$.

In this work, we explicitly derive the direct amplitude in velocity and length gauge applying partial-wave expansion to the initial and final states following a recent work done

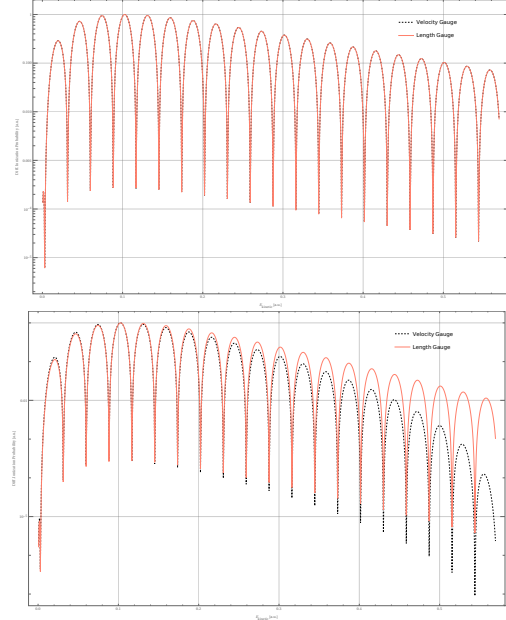


Figure 1: Normalized ATI spectra of Argon. From the upper to lower plots, the hydrogenic-like 1s-state and 3p-state are using respectively. Laser parameters: circular polarized \sin^2 -pulse with 2-cycles, 800nm wavelength, and constant intensity $1 \times 10^{14} \text{W/cm}^2$. The CEP phase $\phi_{\text{CEP}} = 0$. The Keldysh parameter $\gamma = 1.15$.

by B.Böning in 2023 [2]. We analyze the gauge dependence of the analytical expression of both gauges. We also compare the direct ATI spectrum of Argon in both gauges considering the initial state as the hydrogenic-like 1s-state or as the hydrogenic-like 3p-state. In figure 1, the ATI spectra of two gauges show agreement when considering the 1s-state, while the spectra in the high kinetic energy regime are sensitive to the choice of gauge when considering the 3p-state. Therefore, we propose a hypothesis as the conclusion: when considering the gauge dependent SFA, the length gauge can be used for solving targets with larger radial scales, such as Xe or even molecules, while the velocity gauge is more appropriate for studying the dynamics of the ionized electrons.

The authors acknowledge funding from Helmholtzzentrum für Schwerionenforschung GmbH, Darmstadt, Germany.

References

- [1] Kasra Amini *et al.*, Rep. Prog. Phys. **82**, 116001 (2019).
- [2] B.Böning and S. Fritzsche, Phys. Rev. A. **107**, 023108 (2023).

* k.zou@hi-jena.gsi.de

Towards enhanced efficiency of spontaneous parametric down-conversion with varying focal planes of interacting beams

R. Bernecker^{*1,2}, B. Baghdasaryan³, and S. Fritzsche^{1,2}

¹Helmholtz-Institut Jena; ²TPI, FSU Jena; ³IAP, FSU Jena

Spontaneous parametric down-conversion (SPDC) is a popular process to prepare bipartite entangled photonic systems. In SPDC, a coherent laser beam pumps a second-order nonlinear crystal to generate correlated photon pairs. In high-dimensional information processing applications, the spatial part of the photons is usually projected into Laguerre-Gaussian (LG) modes by Spatial Light Modulators (SLMs) and detected by Single-Mode Fibers (SMFs), which only collect photons in the Fundamental Gaussian Mode (FGM). The detection modes possess typical Gaussian parameters like a beam waist w and a focal plane at position z . We show that the collection efficiency in SPDC highly depends on the choice of both parameters.

A generated photon pair consists of *signal* and *idler*, that fulfill the energy conservation $\omega_p = \omega_s + \omega_i$ and the phase-matching condition $\mathbf{k}_p = \mathbf{k}_s + \mathbf{k}_i$. Phase-matching and the pump beam properties, including the beam waist size w_p and the focal plane position z_p relative to the crystal, inherently specify the properties of the photons and generation efficiency. In the detection process, when signal and idler are projected into LG modes, the beam parameters $w_{s,i}$ and $z_{s,i}$ are determined by the *back-projection* of the SLM and SMF in the set-up [1], see Figure 1.

In our study, we first decomposed the state for collinear set-ups into the (frequency-dependent) LG basis

$$|\Psi\rangle = \int d\omega_s d\omega_i \sum_{p_s, \ell_s} \sum_{p_i, \ell_i} C_{p_s, p_i}^{\ell_s, \ell_i}(\omega_s, \omega_i) |p_s, \ell_s\rangle \otimes |p_i, \ell_i\rangle,$$

where p is the radial and ℓ the orbital angular momentum index. Within the paraxial regime, we express the longitudinal momentum component $k_z \approx k(\omega) - \frac{|q|^2}{k(\omega)}$ in terms of

*richard.bernecker@uni-jena.de

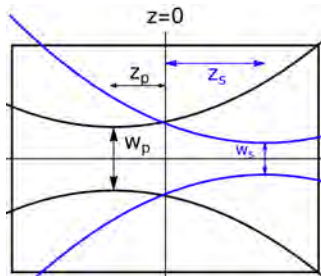


Figure 1: Sketch of pump and signal beam in the crystal with variable beam waist $w_{p,s}$ and focal plane position $z_{p,s}$. The idler beam focusing can be similarly imagined. Focal planes are usually assumed at the crystal center $z = 0$.

the transverse momentum \mathbf{q} . The expansion amplitude for a pump in mode $\text{LG}_{p_p}^{\ell_p}$ reads

$$C_{p_s, p_i}^{\ell_s, \ell_i} \propto \int dz d\mathbf{q}_s d\mathbf{q}_i e^{i(k_{z,p}(\omega_s + \omega_i) - k_{z,s}(\omega_s) - k_{z,i}(\omega_i))z} \times \text{LG}_p^{\ell_p}(\mathbf{q}, w_p, z_p) \left[\text{LG}_{p_s}^{\ell_s}(\mathbf{q}_s, w_s, z_s) \right]^* \left[\text{LG}_{p_i}^{\ell_i}(\mathbf{q}_i, w_i, z_i) \right]^*.$$

The angular spectra of the beams are given by $\text{LG}_p^{\ell_p}(\mathbf{q}, w, z') = \text{LG}_p^{\ell_p}(\mathbf{q}, w, 0) e^{\pm i k_z z'}$. The coupling efficiency $P_{p_s, p_i}^{\ell_s, \ell_i}(\omega_s, \omega_i) = |C_{p_s, p_i}^{\ell_s, \ell_i}(\omega_s, \omega_i)|^2$, whose maximum over all possible frequencies $\omega_{s,i}$ is called the *spectral brightness*, is to be investigated in terms of focal plane positions.

In general, we found that the spectral brightness always peaks if all three beams are positioned in the crystal center. Conversely, when considering monochromatic (i.e. experimentally filtered) frequencies $\omega_{s,i}$, all focal planes in the crystal center would not always attain the highest coupling efficiency. Small shifts of the focal plane positions from the center could strongly affect the coupling efficiency, see Figure 2. In line with the advanced-wave picture [2], focal plane shifts of pump, signal, and idler must compensate each other in opposite z -direction. However, in Ref. [3] we show that equal positioning of signal and idler focal planes is sufficient in most setups when $w_s = w_i$ is fulfilled. Furthermore, we investigate the spatial and temporal characteristics of photon pairs for varying $z_{s,i}$.

References

- [1] A. M. Yao, New J. Phys. **13**, 053048 (2011).
- [2] D. Belinskii, D. N. Klyshko. JETP **78**, 259 (1994).
- [3] R. Bernecker *et al.*, Eur. Phys. J. D **77**, 172 (2023).

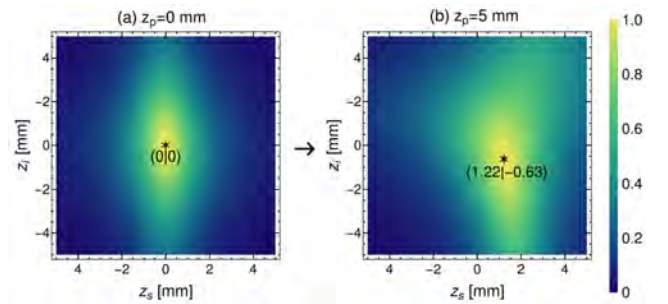


Figure 2: The coupling efficiency of the FGM in dependence of signal and idler focal plane shifts and different pump focal plane positions. The setup parameters are $w_p = w_s = 10 \mu\text{m}$, $w_i = 20 \mu\text{m}$ and $\lambda_s = 810 \text{ nm}$ for an crystal of length 1 mm.

Interaction of Hermite-Gaussian modes with a macroscopic atomic target

S. Ramakrishna ^{*1,2,3}, Z. W. Wu^{1,2}, A. V. Maiorova^{1,2}, and S. Fritzsche^{1,2,3}

¹HI Jena, Fröbelstieg 3, 07743 Jena, Germany; ²GSI, Darmstadt; ³TPI, FSU Jena

We present a theoretical analysis of the photoexcitation of a macroscopic atomic target by a Hermite-Gaussian (HG) beam within the framework of density matrix theory. Special emphasis is paid to the influence of the incoming HG mode on the population of an excited state and the emitted fluorescence radiation. In particular, we derive a general expression for the alignment parameter of the excited state, which depends on the beam parameters of the HG mode. Although the developed theory can be applied to any atomic system, here we investigate the electric dipole transition $3s\ ^2S_{1/2} \rightarrow 3p\ ^2P_{3/2}$ in neutral sodium atoms, when driven by three HG_{10} , HG_{01} and HG_{11} modes. For this optical (valence-shell) excitation, we demonstrate that the population of the excited state is sensitive to the beam waist and the mode index of the HG beam. Furthermore, we discuss the influence of beam parameters on the angular distribution and linear polarization of the emitted fluorescence radiation.

Structured light beams have spatially varying transverse intensity, phase, and polarization texture [1]. These unique properties have led to various applications in fields, such as high harmonic generation, optical tweezers, and quantum cryptography. Two well-known structured light fields are Hermite-Gaussian (HG) and Laguerre-Gaussian (LG) beams. HG and LG modes are solutions of the paraxial Helmholtz equation in Cartesian and cylindrical coordinates, respectively. In recent years, the interaction of these light modes with atomic targets has gained increased attention. However, the interaction of HG light beams with macroscopic atomic targets has been explored less. Hence in this work, we consider photoexcitation of neutral Sodium atoms by three different HG modes.

To achieve our goal, we start by expressing the HG modes as a linear combination of paraxial circularly polarized LG beams with an equal and opposite projection of orbital angular momentum $m_\ell = \pm 1, \pm 2$ [2]. As a next step, we describe the unpolarized atomic initial and final states with the help of density matrix theory. Then, we arrive at the expression for the statistical tensor [3] which in turn represents the final state of the atom. This statistical tensor is evaluated with the help of the transition matrix elements and by averaging over all the randomly distributed atoms in the beam cross-section. To study the sublevel population of the excited state, angular distribution, and linear polarization of the emitted fluorescence we define the alignment parameter. Due to the symmetry and the chosen values of m_ℓ , we obtain only the second rank tensor for the align-

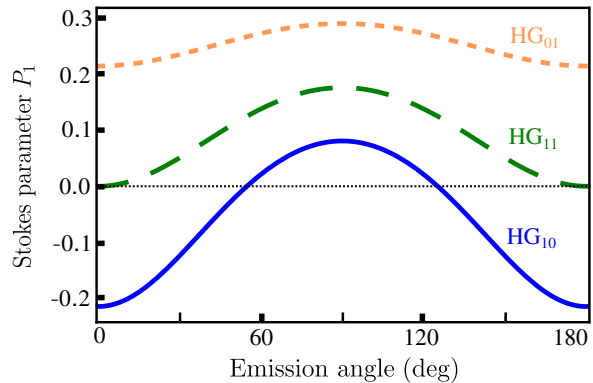


Figure 1: The linear polarization of the emitted fluorescence $3s\ ^2S_{1/2} \rightarrow 3p\ ^2P_{3/2}$ is plotted against the emission angle θ . Here, beam waist of HG mode is $w_o = 5\ \mu\text{m}$.

ment parameter with zero and ± 2 projections, respectively.

Even though we can consider any atom as the target interacting with the chosen HG mode, we here consider neutral Na atoms that undergo electric dipole transition ($3s\ ^2S_{1/2} \rightarrow 3p\ ^2P_{3/2}$). This atomic target is preferred because of the single electron present in its valence shell. For the chosen atomic system, our calculations reveal that only excited state $M_f = 1/2$ is populated and this has a weak dependence over the change in the beam waist of the HG mode. Similarly, we observe that the observables such as the angular distribution and the Stokes parameters show variations for small beam waist rather than larger waist. Following this, we plot the Stokes parameter P_1 for a fixed beam waist against the emission angle θ as shown in Fig. 1. This shows that the three HG modes interact differently and this is reflected in the linear polarization of the emitted fluorescence where HG_{01} mode produces stronger polarized radiation in comparison to HG_{11} and HG_{10} modes. We believe these results could be used for diagnosing the HG modes and will be of importance for future works related to structured light atom interaction.

The authors acknowledge funding from the Research School of Advanced Photon Science (RS-APS) of Helmholtz Institute Jena, Germany.

References

- [1] H. Rubinsztein-Dunlop *et al.*, J. Opt. **19**, 013001 (2016)
- [2] D. L. Andrews *et al.*, The angular momentum of light, Cambridge University Press (2012)
- [3] V. V. Balashov *et al.*, Polarization and correlation phenomena in atomic collisions: a practical theory course, Springer Science (2000)

* shreyas.ramakrishna@uni-jena.de

Quantum electrodynamics of relativistic Luttinger fermions

H. Gies^{*1,2} and M. Picciao²

¹HI Jena, Fröbelstieg 3, 07743 Jena, Germany; ²TPI, FSU Jena

We propose relativistic Luttinger fermions as a new ingredient for the construction of quantum field theories. We construct the corresponding Clifford algebra and the spin metric for relativistic invariance of the action using the spin-base invariant formalism. The corresponding minimal spinor has 32 complex components, matching with the degrees of freedom of a standard-model generation including a right-handed neutrino. As an example for a perturbatively renormalizable theory, we explore quantum electrodynamics (QED) with relativistic Luttinger fermions and compute the beta function of the running gauge coupling. The resulting modified QED theory exhibits a renormalization flow that is governed by the Pauli spin-field coupling, thus exemplifying strong paramagnetic dominance as is familiar from many gauge theories.

One of the remarkable features of quantum field theories is given by the interconnection of fields as representations of the Lorentz group, their powercounting dimensionality and the renormalizability of interacting field theories in $d = 3 + 1$ -dimensional spacetime. These interconnections are particularly obvious in the standard model containing spin $0, \frac{1}{2}, 1$ fields and accommodating all possible renormalizable interactions allowed by the symmetries.

Based on the principle of spin-base invariance [1], we have explored the possibility to construct relativistic versions of Luttinger fermions [2] (so far known as effective degrees of freedom in spin-orbit-coupled solid-state materials). The corresponding relativistic wave equation can be viewed as a generalization of the Dirac equation and yields a second order PDE of the form [3]

$$(-G_{\mu\nu}\partial^\mu\partial^\nu - m^2)\psi = 0, \quad (1)$$

where the Luttinger spin matrices $G_{\mu\nu}$ satisfy the Clifford algebra,

$$\{G_{\mu\nu}, G_{\kappa\lambda}\} = -\frac{2}{d-1}g_{\mu\nu}g_{\kappa\lambda} + \frac{d}{d-1}(g_{\mu\kappa}g_{\nu\lambda} + g_{\mu\lambda}g_{\nu\kappa}), \quad (2)$$

as a generalization of the Dirac algebra for Lorentz tensor-valued spin matrices. In $d = 3 + 1$ spacetime dimensions, the algebra together with a proper spin metric for the construction of the conjugated spinor requires the $G_{\mu\nu}$ to be at least 32-dimensional matrices in spinor space. Hence, a Luttinger fermion consists of a 32-component spinor.

Counting the degrees of freedom, such a 32-component Luttinger spinor contains eight 4-component Dirac spinors. Noteworthy, this covers the number of spinor degrees

of freedom in one standard-model family: up and down quarks with 3 colors each, an electron and a neutrino (including a possible right-handed component). This raises the question as to whether a UV completion of the standard model in terms of a model with Luttinger-fermionic matter can be constructed.

Luttinger fermions can straightforwardly be coupled to gauge fields by minimal coupling. For instance, the action for quantum electrodynamics (QED) with Luttinger fermions reads [3]

$$S = \int_x \left[-\frac{1}{4}F_{\mu\nu}F^{\mu\nu} - \bar{\psi}G_{\mu\nu}D^\mu D^\nu\psi - m^2\bar{\psi}\psi \right], \quad (3)$$

where $D^\mu = \partial^\mu - ieA^\mu$. As an example of a quantum phenomenon, we have studied the running coupling of QED by computing its β function, yielding [3]

$$\beta_{e^2} = \frac{4 \cdot 19}{9\pi^2} e^4 = \frac{4}{9\pi^2} \left(22 \Big|_{\text{para}} - 3 \Big|_{\text{dia}} \right) e^4. \quad (4)$$

In the last expression, we have decomposed the result into a “diamagnetic” contribution from the Klein-Gordon operator and a “paramagnetic” contribution arising from the remaining terms including the spin-field coupling. Obviously, we observe *paramagnetic dominance*, i.e. the paramagnetic contributions dominate the final result and are also responsible for the sign of the β function, as is known for many theories including nonabelian gauge theories and even gravity [4].

The new kind of relativistic fermion degrees of freedom pave the way to unprecedented explorations of new particle physics models in four spacetime dimensions. Owing to their powercounting properties, models with quartic self-interactions of relativistic Luttinger fermions can be asymptotically free in $d = 3 + 1$ dimensional spacetime and thus have a chance to exist as fundamental quantum field theories on all scales. The construction and investigation of such models is subject to ongoing work.

This work has been funded by the DFG under Grant No. 406116891 within the Research Training Group RTG 2522/1 and under 392856280, 416607684, and 416611371 within the Research Unit FOR2783/2. .

References

- [1] H. Gies and S. Lippoldt, Phys. Rev. D **89**, 064040 (2014). [arXiv:1310.2509 [hep-th]].
- [2] J. M. Luttinger, Phys. Rev. **102**, 1030 (1956).
- [3] H. Gies, P. Heinzl, J. Lauffkötter and M. Picciao, [arXiv:2312.12058 [hep-th]].
- [4] A. Nink and M. Reuter, JHEP **01**, 062 (2013).

*holger.gies@uni-jena.de

3D simulations of angular deflection as novel signatures of radiation reaction in electron-beam laser sidescattering

P. Sikorski^{*1}, A. G. R. Thomas², S. S. Bulanov³, M. Zepf¹, and D. Seipt¹

¹HI Jena, Fröbelstieg 3, 07743 Jena, Germany; ²G erard Mourou Center for Ultrafast Optical Science, University of Michigan, Ann Arbor, Michigan 48109, USA; ³Lawrence Berkeley National Laboratory, California 94720, USA

We investigated the angular deflection of an electron beam colliding at 90 degrees with an intense laser pulse as a novel signature of radiation reaction (RR). According to analytical theory based on the Landau-Lifshitz equation in a 1 dimensional geometry the deflection angle must vanish identically in the absence of RR. Here, the analytically derived deflection is contrasted with the full-scale 3D Monte Carlo PIC simulations. Our results show that the deflection should be observable with present-day laser technology.

Using the classical Landau-Lifshitz (LL) theory [1] we found an expression for the electron deflection angle after the interaction with the laser [2, 3],

$$\theta \approx -\frac{2}{3} \frac{a_0^3 \omega_0 \alpha}{m} \mathcal{H}_1(\phi). \quad (1)$$

We consider the 90-degree scattering of the electrons and laser beam, where the electron beam initially propagates along the x -axis and the laser beam propagates along the z -axis. The laser is linearly polarized along the x -axis, with pulse shape function $f_1(\phi)$. The deflection angle is proportional $\mathcal{H}_1(\phi) = \int_{-\infty}^{\phi} f_1'(\psi) \mathcal{I}(\psi) d\psi$ is related to the temporal asymmetry of the laser pulse, with the integrated laser intensity $\mathcal{I}(\phi) = \int_{-\infty}^{\phi} f_1'(\psi)^2 d\psi$. Moreover, ω_0 is the central laser frequency and a_0 is the normalized vector potential.

Eq. (1) illustrates that (i) the scattering angle scales as a_0^3 but is independent of the electron beam energy and (ii) a temporal asymmetry of the laser vector potential is crucial to achieve nonzero deflection angles. Criterion (i) gives us some leeway to chose an interaction regime where the quantum nonlinearity parameter χ remains small [2]. We choose $a_0 = 30$ and electron energy 100 MeV. To fulfill criterion (ii) we employ two-color pulses where a $2\omega_0$ component is superimposed on the fundamental light [2].

The theoretical analysis is based on an idealized 1D geometry. To asses the impact of non-ideal 3D effects, such as ponderomotive scattering and the geometric overlap of the beams, as well as the impact of quantum stochasticity, we have performed full-scale 3D simulations. They were performed with the PIC code SMILEI [4] with the radiation reaction simulated via its Monte Carlo Strong-Field QED module. Fig. 1 exhibits the results of the 3D simulation campaign, where we permute over the electron beam sizes and laser spot size w_0 . The laser intensity parameter $a_0 = 30$ and laser pulse duration were kept fixed. Our simulations show that 3D effects reduce the analytically pre-

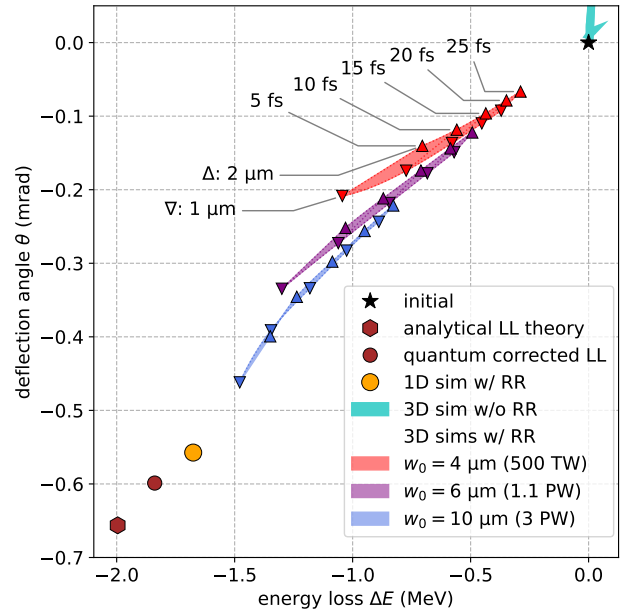


Figure 1: Survey of expected signals of radiation reaction in 90 degree sidescattering over simulations with various parameters. The brown hexagon and orange circle symbols are for the analytical LL theory and 1D simulations, respectively. The shaded areas represent two-dimensional parameter scans using 3D simulations across transverse electron beam size $\sigma_{y,z}$ and beam duration L_{ebeam} . Each of the shaded areas corresponds to a different laser power. All simulations with RR considered show a deflection angle and energy loss significantly different from the null-result (black star and cyan shaded areas in upper right).

dicted deflection angles. Nonetheless, the values of the RR signals remain clearly distinct from the null result.

In summary, our 3D QED-PIC Monte Carlo simulations confirm that the electron deflection studied in this work could serve as a novel signature of radiation reaction effects with present-day (multi-)PW class lasers and high-quality LWFA electron beams.

References

- [1] L. D. Landau and E. M. Lifschits, Course of Theoretical Physics, vol. 2, (1975).
- [2] P. Sikorski *et al.*, New J. Phys. **26**, 063011 (2024).
- [3] A. Di Piazza, Lett. Math. Phys. **83**, 305 (2008).
- [4] J. Derouillat *et al.*, Comput. Phys. Commun. **222**, 351 (2018).

* philipp.sikorski@uni-jena.de

Phase space structure of nonlinear Compton scattering

N. Larin*¹ and D. Seipt¹

¹HI Jena, Fröbelstieg 3, 07743 Jena, Germany

Considering the nonlinear Compton scattering, we demonstrate how the time-frequency analysis methods can be used to study the phase space structure of the final state particles. We employ the Husimi transform to obtain pseudo-probability distribution, which qualitatively describes how the cycle scale interference leads to the appearance of complicated harmonic structure in the spectrum of emitted radiation.

Electromagnetic field of high intensity drastically alters the behavior of processes that take place within it. Recent progress in generation of short intense laser pulses makes the observation of new phenomena feasible, motivating the further development of advanced theoretical approaches.

Of particular interest is the nonlinear Compton scattering (NCS), which has been extensively studied throughout the several previous decades [1]. Many analytical and numerical methods were employed to understand all peculiarities that stem from the nonlinear interaction between a charged particle and an external field. Namely, the most pronounced signature of nonlinearity is the intricate harmonic structure in the spectrum of emitted radiation. These harmonics originate from the cycle scale interference, but it yet hasn't been studied how they are formed and how different laser pulse configurations and intensities influence the process of their formation.

To answer these questions, we consider a distribution with respect to two canonically conjugate variables: the average laser phase φ and the momentum transferred by the field ℓ . Due to the Heisenberg's uncertainty principle the exact simultaneous values of canonically conjugate variables are not defined, so we use methods of time-frequency analysis to extract information about them with the given precision and obtain the so-called scalogram [2] for NCS (see, Fig.1).

One possible way to do it is to apply Husimi transform to the square of NCS amplitude [3]:

$$\mathcal{R}_H(\varphi, \ell) \sim \iint_{\mathbb{R}^2} d\varphi' d\ell' |\mathcal{M}(\varphi', \ell')|^2 g_{\sigma_\varphi} g_{\sigma_\ell}, \quad (1)$$

where g_{σ_φ} and g_{σ_ℓ} are the normalized Gaussian functions centered at φ and ℓ correspondingly, which dispersions are linked via the condition $(\sigma_\ell \sigma_\varphi = 1/2)$. This constrain allows us to tune the convolution by varying the single parameter $\sigma_0 \equiv \sigma_\ell = 1/(2\sigma_\varphi)$.

Performing the Husimi transform, we smear the square of transition amplitude in both canonically conjugate vari-

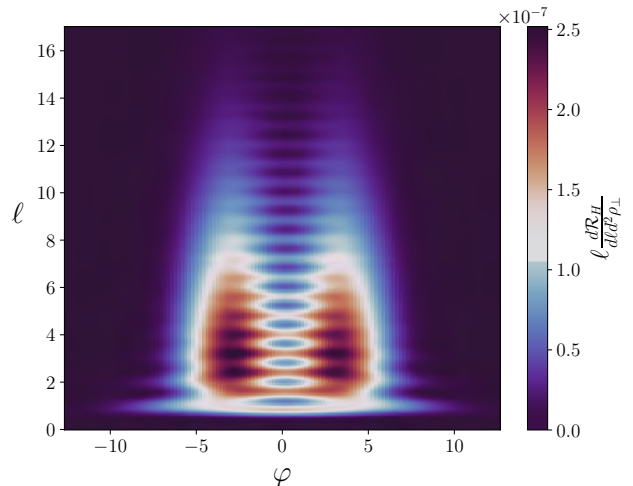


Figure 1: Husimi distribution with $\sigma_0 = 1/\sqrt{4\pi}$ for the angular-resolved power spectrum of NCS. The parameters of circularly polarized pulse are: $a_0 = 20$, $N_{\text{cycles}} = 4$.

ables (1), distorting true probability magnitude. Then, following the standard procedure [1], we construct the quantity $\mathcal{R}_H \geq 0$ that possesses all properties of the probability rate. It contains information about the emitted photon phase space, which allows us to qualitatively answer the question: how different parts of the laser pulse contribute to the emitted photon spectrum? However, \mathcal{R}_H has to be treated not as a standard probability distribution, but rather as a pseudo-probability distribution [4].

On the Fig. 1 we present the angular-resolved distribution for the large angles $\rho_\perp \approx \gamma(\theta_x, \theta_y) = (2, 40)$. From this, we can see where in the pulse the particular harmonic is emitted, and how significant is its contribution to the spectrum, which can be obtained by integrating over the average phase φ .

Our approach is applicable for arbitrary laser intensities and pulse durations. Therefore, we are able to investigate parameter regimes, which lay beyond any standard approximation. Moreover, we can study different effects associated with various tailored pulse configurations.

References

- [1] A. Fedotov *et al.*, Phys. Reports **1010**, 1-138 (2023).
- [2] O. Rioul and P. Flandrin, IEEE Transactions on Signal Processing, **40**, 1746-1757 (1992).
- [3] E. Colomés *et al.*, J. Comput. Electron **14**, 894-906 (2015).
- [4] P. Goncalves and R. G. Baraniuk, IEEE Transactions on Signal Processing, **46**, 1505-1516 (1998).

*nikita.larin@uni-jena.de

Laser polarization control of ionization-injected electron beams and x-ray radiation in LWFA

A. Mukherjee^{*1,2} and D. Seipt^{1,2}

¹HI Jena, Fröbelstieg 3, 07743 Jena, Germany; ²GSI, Darmstadt, Germany

We have studied the influence of laser polarization on the dynamics of the ionization-injected electron beams, and subsequently, the properties of the emitted betatron radiation in LWFA. It has been found that the polarization-dependent transverse momentum, gained by the ionized electrons via above threshold ionization (ATI) process, greatly affects the dynamics of the accelerated electron beam. It has been demonstrated that a precise steering of the ionization-injected electrons by the laser polarization also serves to control the properties of the emitted betatron radiation.

In LWFA, a relativistically intense laser pulse is focused into an undercritical plasma medium, where it excites a nonlinear wakefield with a strong longitudinal electrical field of up to 100 GV/m. By trapping electrons in this wakefield the longitudinal fields are used to accelerate electrons to GeV energies on centimeter scales, which allows for very compact accelerators compared to conventional RF technology [1].

Current LWFA research focuses mostly on improving the electron beam quality and operating LWFA's at higher repetition rates. Precise control of the electron beam properties is naturally difficult due to the transient nature of the plasma in which the LWFA process takes place. This puts demanding requirements on the laser and plasma targets to achieve the desired beam parameters, especially for controlling the beam's phase-space properties. However, the primary opportunity to control the beam properties can be found in the electron injection processes [2].

Our present work primarily aims to demonstrate that the dynamics of the electron beams, and betatron radiation properties can be controlled by tuning the laser polarization by utilizing ionization injection scheme. The phenomenology of the strong field ionization process via ATI mechanism can be understood as a two-step process. In the first step, the electron tunnel ionizes instantaneously from a deeply bound state to the continuum, where it is assumed to have zero velocity initially. In the second step, in the continuum, the electron's transverse canonical momentum is conserved, $\mathbf{p}_\perp - e\mathbf{A} = \text{const}$. In ionization injection, electrons ionized from the K-shell of a mid-Z injector gas slip backward relative to the wake and get trapped inside the wake potential. At this point, the residual ATI momentum gained by the electrons (p_\perp) during the ionization process serves as the initial condition for the acceleration. These initial conditions of the trapped electrons can be precisely controlled by laser polarization in terms of ATI momentum.

In Fig. 1, we have shown the trajectories of a few elec-

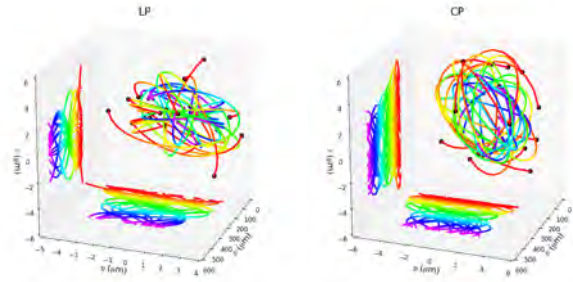


Figure 1: Trajectories of few trapped electrons for LP (left) and CP cases (right). Here color represents the time.

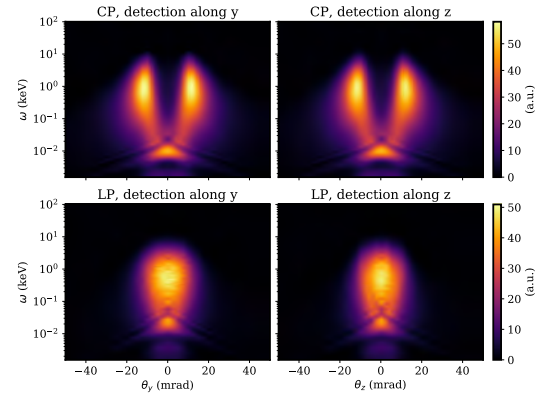


Figure 2: 2D colormaps of radiation for CP and LP case, measured along the transverse directions (y and z) of the acceleration.

trons during their acceleration for linear polarization (LP, left) and circular polarization cases (CP, right). We see that for the LP case (where a large fraction of electrons have zero ATI momentum), different electron trajectories have different ellipticities and orientation angles. But, in the CP case, we see that electrons move in a three-dimensional helical trajectory and electron transverse trajectories are more circular, which is a manifestation of nonzero ATI momentum during ionization [3].

Fig. 2 shows the 2D colormaps of the radiation spectra, showing that the spatial distribution of the emitted radiation in the above two cases is substantially different, and thus, depends on the laser polarization [3].

References

- [1] E. Esarey *et al.*, Rev. Mod. Phys. **81**, 1229 (2009).
- [2] Y. Ma *et al.*, Phys. Rev. Lett. **124**, 114801 (2020).
- [3] A. Mukherjee *et al.*, PPCF **66**, 085001 (2024).

* a.mukherjee@hi-jena.gsi.de

PUBLICATIONS

S. Ringleb, M. Kiffer, J. K. C. Ballentin, Th. Stöhlker, and M. Vogel

Position-sensitive non-destructive detection of charged-particle bunches in low-energy beamlines

Scientific Reports **13**, 22669 (2023)

10.1038/s41598-023-45798-6

F. Karbstein, S. Stuetzer, H. Gies, and A. Szameit

Exploring new states of matter with a photonic emulator

Physical Review Research **5**, L042036 (2023)

10.1103/PhysRevResearch.5.L042036

A. Magunia, M. Rebholz, E. Appi, C. C. Papadopoulou, H. Lindenblatt, F. Trost, S. Meister, T. Ding, M. Straub, G. D. Borisova, J. Lee, R. Jin, A. von der Dellen, C. Kaiser, M. Braune, S. Duesterer, S. Alisauskas, T. Lang, C. Heyl, B. Manschwetus, S. Grunewald, U. Fruehling, A. Tajalli, A. Bin Wahid, L. Silletti, F. Calegari, P. Mosel, U. Morgner, M. Kovacev, U. Thumm, I. Hartl, R. Treusch, R. Moshhammer, C. Ott, and T. Pfeifer

Time-resolving state-specific molecular dissociation with XUV broadband absorption spectroscopy

Science Advances **9**, eadk1482 (2023)

10.1126/sciadv.adk1482

R. Heintzmann, L. Loetgering, and F. Wechsler

Scalable angular spectrum propagation

Optica **10**, 1407 (2023)

10.1364/OPTICA.497809

Z. W. Wu, W. Liu, and S. Fritzsche

Angular and polarization properties of characteristic x-ray radiation following inner-shell $2p_{3/2}$ photoionization of high-Z atoms

Physical Review A **108**, 053115 (2023)

10.1103/PhysRevA.108.053115

Z. X. Hu, L. G. Jiao, A. Liu, Y. C. Wang, H. E. Montgomery Jr, Y. K. Ho, and S. Fritzsche

Resonances in the Hulthén potential: benchmark calculations, critical behaviors, and interference effects

Journal Of Physics A-mathematical And Theoretical **56**, 445301 (2023)

10.1088/1751-8121/acfe65

M. Karst, M. Benner, P. Gierschke, H. Stark, and J. Limpert

Dispersion engineering in nonlinear multipass cells for high-quality pulse compression

Optics Letters **48**, 5899 (2023)

10.1364/OL.504014

- A. Platz, S. Hell, Y. Zhang, B. Ying, G. G. Paulus, and M. Kübel
Intensity-resolved measurement of above-threshold ionization of Ar-H₂O
Physical Review A **108**, 053106 (2023)
 10.1103/PhysRevA.108.053106
- E. Eftekhari-Zadeh, R. Löttsch, L. Manganelli, M. S. Bluemcke, A. Tauschwitz, I. Uschmann, A. Pukhov, O. Rosmej, C. Spielmann, and D. Kartashov
Complex diagnostic and numerical study of x-ray and particle emissions under relativistic ultra-short laser-solid interaction
Physica Scripta **98**, 115615 (2023)
 10.1088/1402-4896/acff8c
- R. Zagidullin, S. Tietze, M. Zepf, J. Wang, and S. Rykovanov
Density-dependent carrier-envelope phase shift in attosecond pulse generation from relativistically oscillating mirrors
Matter And Radiation At Extremes **8**, 064004 (2023)
 10.1063/5.0155957
- G. Visentin, S. Schippers, and S. Fritzsche
Dielectronic recombination plasma rate coefficients of Na-, Mg-, and Al-like iron ions: The role of the $2(s + p) \rightarrow 4l, nl'$ and $3(s + p) \rightarrow 5l, nl'$ resonances
Astronomy & Astrophysics **679**, A13 (2023)
 10.1051/0004-6361/202347456
- J. Sommerfeldt, S. Strnat, V. A. Yerokhin, W. Middents, Th. Stöhlker, and A. Surzhykov
Low-energy tests of Delbrück scattering
Physical Review A **108**, 042819 (2023)
 10.1103/PhysRevA.108.042819
- H. Gies, K. K. K. Tam, and J. Ziebell
Pauli-term-induced fixed points in d-dimensional QED
European Physical Journal C **83**, 955 (2023)
 10.1140/epjc/s10052-023-12080-y
- R. N. Soguel and S. Fritzsche
Insight into the prospective evaluation of third-order interelectronic corrections on Li-like ions
Physical Review A **108**, 042807 (2023)
 10.1103/PhysRevA.108.042807
- Y. Schroedel, C. Hartmann, J. Zheng, T. Lang, M. Steudel, M. Rutsch, S. H. Salman, M. Kellert, M. Pergament, T. Hahn-Jose, S. Suppelt, J. H. Doersam, A. Harth, W. P. Leemans, F. X. Kaertner, I. Hartl, M. Kupnik, and C. M. Heyl
Acousto-optic modulation of gigawatt-scale laser pulses in ambient air
Nature Photonics **18**, (2023)
 10.1038/s41566-023-01304-y

Q. Qian, D. Seipt, M. Vranic, T. E. Grismayer, T. G. Blackburn, C. P. Ridgers, and A. G. R. Thomas

Parametric study of the polarization dependence of nonlinear Breit-Wheeler pair creation process using two laser pulses

Physics Of Plasmas **30**, 103107 (2023)

10.1063/5.0165788

Y. Shvyd'ko, R. Röhlsberger, O. Kocharovskaya, J. Evers, G. A. Geloni, P. Liu, D. Shu, A. Miceli, B. Stone, W. Hippler, B. Marx-Glowna, I. Uschmann, R. Löttsch, O. Leupold, H.-C. Wille, I. Sergeev, M. Gerharz, X. Zhang, C. Grech, M. Guetg, V. Kocharyan, N. Kujala, S. Liu, W. Qin, A. Zozulya, J. Hallmann, U. Boesenberg, W. Jo, J. Moeller, A. Rodriguez-Fernandez, M. Youssef, A. Madsen, and T. Kolodziej

Resonant X-ray excitation of the nuclear clock isomer ^{45}Sc

Nature **622**, 471 (2023)

10.1038/s41586-023-06491-w

Z. Tian, Z. Tang, Y. Li, Y. Yang, Z. Wu, and Y. Zou

Hyperfine-induced effects on the linear polarization of the magnetic-quadrupole lines of spin-1/2 Be-like ions excited by electron impact

Journal Of Quantitative Spectroscopy & Radiative Transfer **311**, 108775 (2023)

10.1016/j.jqsrt.2023.108775

S. Rajhans, E. Escoto, N. Khodakovskiy, P. K. Velpula, B. Farace, U. Grosse-Wortmann, R. J. Shalloo, C. L. Arnold, K. Poder, J. Osterhoff, W. P. Leemans, I. Hartl, and C. M. Heyl

Post-compression of multi-millijoule picosecond pulses to few-cycles approaching the terawatt regime

Optics Letters **48**, 4753 (2023)

10.1364/OL.498042

W. H. Xia, Z. L. Zhou, L. G. Jiao, A. Liu, H. E. Montgomery Jr, Y. K. Ho, and S. Fritzsche

Variational perturbation theory for dynamic polarizabilities and dispersion coefficients

Physical Review E **108**, 035305 (2023)

10.1103/PhysRevE.108.035305

L. Xu, L. G. Jiao, A. Liu, Y. C. Wang, H. E. Montgomery, Y. K. Ho, and S. Fritzsche

Critical screening parameters of one-electron systems with screened Coulomb potentials: Circular Rydberg states

Journal Of Physics B-Atomic Molecular And Optical Physics **56**, 175002 (2023)

10.1088/1361-6455/aced2d

M. C. Kaluza

Unveiling the inner structure of electron pulses generated from a laser-wakefield accelerator

Light-science & Applications **12**, 225 (2023)

10.1038/s41377-023-01269-1

K. Koenig, S. Fritzsche, G. Hagen, J. D. Holt, A. Klose, J. Lantis, Y. Liu, K. Minamisono, T. Miyagi, W. Nazarewicz, T. Papenbrock, S. V. Pineda, R. Powel, and P.-G. Reinhard

Surprising Charge-Radius Kink in the Sc Isotopes at N=20

Physical Review Letters **131**, 102501 (2023)

10.1103/PhysRevLett.131.102501

R. Bernecker, B. Baghdasaryan, and S. Fritzsche

Spatial and temporal characteristics of spontaneous parametric down-conversion with varying focal planes of interacting beams

European Physical Journal D **77**, 172 (2023)

10.1140/epjd/s10053-023-00754-x

B. K. Russell, P. T. Campbell, Q. Qian, J. A. Cardarelli, S. S. Bulanov, S. V. Bulanov, G. M. Gritani, D. Seipt, L. Willingale, and A. G. R. Thomas

Ultrafast relativistic electron probing of extreme magnetic fields

Physics Of Plasmas **30**, 093105 (2023)

10.1063/5.0163392

D. Seipt and A. G. R. Thomas

Kinetic theory for spin-polarized relativistic plasmas

Physics Of Plasmas **30**, 093102 (2023)

10.1063/5.0165836

Z. W. Wu, Z. Q. Tian, C. Z. Dong, A. Surzhykov, and S. Fritzsche

Hyperfine-induced effects on K_{α_1} linear polarization following electron-impact excitation of heliumlike Tl^{79+} ions with nuclear spin $I = 1/2$

New Journal Of Physics **25**, 093039 (2023)

10.1088/1367-2630/acf8e9

L. Xu, L. G. Jiao, A. Liu, H. E. Montgomery Jr., Y. K. Ho, and S. Fritzsche

Energy spectra and asymptotic laws of the radial screened Coulomb potential

Physics Letters A **483**, 129064 (2023)

10.1016/j.physleta.2023.129064

B. Baghdasaryan, F. Steinlechner, and S. Fritzsche

Enhancing the purity of single photons in parametric down-conversion through simultaneous pump-beam and crystal-domain engineering

Physical Review A **108**, 023718 (2023)

10.1103/PhysRevA.108.023718

A. Steinkopff, C. Aleshire, A. Klenke, C. Jauregui, and J. Limpert

Analysis of optical core-to-core coupling: challenges and opportunities in multicore fiber amplifiers

Optics Express **31**, 28564 (2023)

10.1364/OE.498460

L. Stoyanov, S. Topuzoski, G. G. Paulus, and A. Dreischuh

Optical vortices in brief: introduction for experimentalists

European Physical Journal Plus **138**, 702 (2023)

10.1140/epjp/s13360-023-04227-3

- J. Sommerfeldt, V. A. Yerokhin, Th. Stöhlker, and A. Surzhykov
All-Order Coulomb Corrections to Delbruck Scattering above the Pair-Production Threshold
Physical Review Letters **131**, 061601 (2023)
10.1103/PhysRevLett.131.061601
- X. Li, Y. Chen, T. Tian, and Z. Sun
Part-based image-loop network for single-pixel imaging
Optics And Laser Technology **168**, 109917 (2023)
10.1016/j.optlastec.2023.109917
- R. Röhlsberger
A delicate balance of phonons and spins
Nature Physics **19**, 1547 (2023)
10.1038/s41567-023-02152-x
- Z. Sun, T. Tian, S. Oh, J. Wang, G. Cheng, and X. Li
Underwater ghost imaging with pseudo-Bessel-ring modulation pattern
Chinese Optics Letters **21**, 081101 (2023)
10.3788/COL202321.081101
- S. Kholaf, C. Jauregui, and J. Limoert
Mitigation of transverse mode instability by heat-load modulation
Optics Express **31**, 26496 (2023)
10.1364/OE.495830
- D. S. P. Molina, L. Loetgering, W. Eschen, J. Limpert, and J. Rothhardt
Broadband ptychography using curved wavefront illumination
Optics Express **31**, 26958 (2023)
10.1364/OE.495197
- J. B. Ohland, D. Posor, U. Eisenbarth, V. Iancu, R. Ungureanu, D. Ursescu, and V. Bagnoud
Zernike-coefficient extraction via helical beam reconstruction for optimization (ZEHBRO) in the far field
High Power Laser Science And Engineering **11**, e86 (2023)
10.1017/hpl.2023.63
- K. V. Grafenstein, F. M. Foerster, F. Haberstroh, D. Campbell, F. Irshad, F. C. Salgado, G. Schilling, E. Travac, N. Weisse, M. Zepf, A. Doepp, and S. Karsch
Laser-accelerated electron beams at 1 GeV using optically-induced shock injection
Scientific Reports **13**, 11680 (2023)
10.1038/s41598-023-38805-3
- A. I. Bondarev, J. H. Gillanders, C. Cheung, M. S. Safronova, and S. Fritzsche
Calculations of multipole transitions in Sn II for kilonova analysis
European Physical Journal D **77**, 126 (2023)
10.1140/epjd/s10053-023-00695-5

- J. Buldt, T. Heuermann, Z. Wang, P. Gierschke, M. Lenski, C. Jauregui, and J. Limpert
High-power two-color plasma-based THz generation driven by a Tm-doped fiber laser
Optics Letters **48**, 3403 (2023)
10.1364/OL.492511
- M. O. Herdrich, D. Hengstler, M. Keller, J. Geist, C. Schoetz, M. Krantz, A. Fleischmann, C. Enss, T. Gassner, P.-M. Hillenbrand, A. Gumberidze, U. Spillmann, S. Trotsenko, P. Indelicato, and Th. Stöhlker
High-resolution X-ray emission study for Xe⁵⁴⁺ collisions on Xe
European Physical Journal D **77**, 125 (2023)
10.1140/epjd/s10053-023-00698-2
- T. Tian, Z. Sun, S. Oh, and C. Spielmann
Image-Enhanced Pseudo-Thermal Ghost Imaging with Hybrid Speckle Pattern
Photonics **10**, 709 (2023)
10.3390/photonics10070709
- S. Nanos, N. J. Esponda, P.-M. Hillenbrand, A. Biniskos, A. Laoutaris, M. A. Quinto, N. Petridis, E. Menz, T. J. M. Zouros, Th. Stöhlker, R. D. Rivarola, J. M. Monti, and E. P. Benis
Cusp-electron production in collisions of open-shell He-like oxygen ions with atomic targets
Physical Review A **107**, 062815 (2023)
10.1103/PhysRevA.107.062815
- D. F. Dar and S. Fritzsche
Pulse Cycle Dependent Nondipole Effects in Above-Threshold Ionization
Atoms **11**, 97 (2023)
10.3390/atoms11060097
- D. Laumer, S. Salman, Y. Ma, K. T. Zawilski, P. G. Schunemann, M. Seidel, C. M. Heyl, and I. Hartl
Sub-Hz relative linewidths from an interferometrically stabilized mid-infrared frequency comb
Optics Letters **48**, 3055 (2023)
10.1364/OL.491684
- X. N. Li, Y. Z. Zhang, L. G. Jiao, Y. C. Wang, H. E. E. Montgomery Jr, Y. K. Ho, and S. Fritzsche
Geometric properties of the ground state of H⁻ and He in dense quantum plasmas
European Physical Journal D **77**, 96 (2023)
10.1140/epjd/s10053-023-00683-9
- S. Oh, Z. Sun, T. Tian, and C. Spielmann
Improvements of Computational Ghost Imaging by Using Sequenced Speckle
Applied Sciences **13**, 6954 (2023)
10.3390/app13126954
- H. Stark, M. Benner, J. Buldt, A. Klenke, and J. Limpert
Pulses of 32 mJ and 158 fs at 20-kHz repetition rate from a spatiotemporally combined fiber laser system
Optics Letters **48**, 3007 (2023)
10.1364/OL.488617

- Z. W. Wu, Z. Q. Tian, and S. Fritzsche
Angular distribution of the characteristic line $1s2p\ ^3P_2 \rightarrow 1s^2\ ^1S_0$ of thallium ions: hyperfine-induced multipole interference
European Physical Journal D **77**, 95 (2023)
 10.1140/epjd/s10053-023-00684-8
- O. Novak, R. Kholodov, A. N. Artemyev, A. Surzhykov, and Th. Stöhlker
Ionization in a laser-assisted ion-ion collision
Physical Review A **107**, 052815 (2023)
 10.1103/PhysRevA.107.052815
- J. Glorius, Y. A. Litvinov, M. Aliotta, F. Amjad, B. Brueckner, C. G. Bruno, R. Chen, T. Davinson, S. F. Dellmann, T. Dickel, I. Dillmann, P. Erbacher, O. Forstner, H. Geissel, C. J. Griffin, R. Grisenti, A. Gumberidze, E. Haettner, R. Hess, P.-M. Hillenbrand, C. Hornung, R. Joseph, B. Jurado, E. Kazanseva, R. Knobel, D. Kostyleva, C. Kozhuharov, N. Kuzminchuk, C. Langer, G. Leckenby, C. Lederer-Woods, M. Lestinsky, S. Litvinov, B. Loeher, B. Lorenz, E. Lorenz, J. Marsh, E. Menz, T. Morgenroth, I. Mukha, N. Petridis, U. Popp, A. Psaltis, S. Purushothaman, R. Reifarth, E. Rocco, P. Roy, M. S. Sanjari, C. Scheidenberger, M. Sguazzin, R. S. Sidhu, U. Spillmann, M. Steck, Th. Stöhlker, J. A. Swartz, Y. K. Tanaka, H. Toernqvist, L. Varga, D. Vescovi, H. Weick, M. Weigand, P. J. Woods, T. Yamaguchi, and J. Zhao
Storage, accumulation and deceleration of secondary beams for nuclear astrophysics
Nuclear Instruments & Methods In Physics Research Section B-Beam Interactions With Materials And Atoms **541**, 190 (2023)
 10.1016/j.nimb.2023.04.059
- Z. Wang, T. Heuermann, M. Gebhardt, M. Lenski, P. Gierschke, R. Klas, J. Rothhardt, C. Jau-regui, and J. Limpert
Nonlinear pulse compression to sub-two-cycle, 1.3 mJ pulses at 1.9 μm wavelength with 132 W average power
Optics Letters **48**, 2647 (2023)
 10.1364/OL.487587
- R. Y. Zheng, L. G. Jiao, A. Liu, J. Ma, H. E. Montgomery Jr, Y. K. Ho, and S. Fritzsche
Stability of the $2p^2\ ^3P^e$ state of two-electron atoms near to critical nuclear charge
Journal Of Physics B-Atomic Molecular And Optical Physics **56**, 095002 (2023)
 10.1088/1361-6455/acc49a
- D. Wanisch, J. D. A. Espinoza, and S. Fritzsche
Information scrambling and the correspondence of entanglement dynamics and operator dynamics in systems with nonlocal interactions
Physical Review B **107**, 205127 (2023)
 10.1103/PhysRevB.107.205127
- Z. Chen, Q. Ding, Q. Chen, S. Li, F. Liu, H. Kang, T. Morishita, and J. Chen
High-order above-threshold ionization in elliptically polarized laser fields: Identifying the recollision time
Physical Review A **107**, 053107 (2023)
 10.1103/PhysRevA.107.053107

- Y. An, X. Shen, P. Yuan, and Z. Wu
Collisional-radiative modeling of the $2p3l(l = p, d)$ spectra of N II and application to lightning
Journal Of Applied Physics **133**, 173301 (2023)
 10.1063/5.0138622
- S. Fritzsche, L.-G. Jiao, Y.-C. Wang, and J. E. Sienkiewicz
Collision Strengths of Astrophysical Interest for Multiply Charged Ions
Atoms **11**, 80 (2023)
 10.3390/atoms11050080
- D. F. Dar, B. Minneker, and S. Fritzsche
Nondipole strong-field approximation for above-threshold ionization in a few-cycle pulse
Physical Review A **107**, 053102 (2023)
 10.1103/PhysRevA.107.053102
- E. Wang, N. G. Kling, A. C. LaForge, R. Obaid, S. Pathak, S. Bhattacharyya, S. Meister, F. Trost, H. Lindenblatt, P. Schoch, M. Kubel, T. Pfeifer, A. Rudenko, S. Diaz-Tendero, F. Martin, R. Moshhammer, D. Rolles, and N. Berrah
Ultrafast Roaming Mechanisms in Ethanol Probed by Intense Extreme Ultraviolet Free-Electron Laser Radiation: Electron Transfer versus Proton Transfer
Journal Of Physical Chemistry Letters **14**, 4372 (2023)
 10.1021/acs.jpcllett.2c03764
- Z. L. Zhou, L. G. Jiao, A. Liu, Y. C. Wang, H. E. E. Montgomery, Y. K. Ho, and S. Fritzsche
Effective pressures on the outer-, inner-, and shell-confined hydrogenic atoms
European Physical Journal D **77**, 78 (2023)
 10.1140/epjd/s10053-023-00663-z
- W. Eschen, C. Liu, D. S. P. Molina, R. Klas, J. Limpert, and J. Rothhardt
High-speed and wide-field nanoscale table-top ptychographic EUV imaging and beam characterization with a sCMOS detector
Optics Express **31**, 14212485779 (2023)
 10.1364/OE.485779
- L. Loetgering, M. Du, D. B. Flaes, T. Aidukas, F. Wechsler, D. S. P. Molina, M. Rose, A. Pelekanidis, W. Eschen, J. Hess, T. Wilhein, R. Heintzmann, J. Rothhardt, and S. Witte
PtyLab.m/py/jl: a cross-platform, open-source inverse modeling toolbox for conventional and Fourier ptychography
Optics Express **31**, 13763485370 (2023)
 10.1364/OE.485370
- L. Stoyanov, A. Stefanov, A. Dreischuh, and G. G. Paulus
Gouy phase of Bessel-Gaussian beams: theory vs. experiment
Optics Express **31**, 13683 (2023)
 10.1364/OE.480761

F. Trost, K. Ayyer, M. Prasciolu, H. Fleckenstein, M. Barthelmess, O. Yefanov, J. L. Dresselhaus, C. Li, S. Bait, J. Carnis, T. Wollweber, A. Mall, Z. Shen, Y. Zhuang, S. Richter, S. Karl, S. Cardoch, K. K. Patra, J. Moeller, A. Zozulya, R. Shayduk, W. Lu, F. Brausse, B. Friedrich, U. Boesenberg, I. Petrov, S. Tomin, M. Guetg, A. Madsen, N. Timneanu, C. Caleman, R. Röhlsberger, J. von Zanthier, and H. N. Chapman

Imaging via Correlation of X-Ray Fluorescence Photons

Physical Review Letters **130**, 173201 (2023)

10.1103/PhysRevLett.130.173201

A. V. Maiorova, S. Fritzsche, A. Surzhykov, and Th. Stöhlker

Radiative recombination of highly charged ions with polarized electrons

Physical Review A **107**, 042814 (2023)

10.1103/PhysRevA.107.042814

Y. Y. He, Z. L. Zhou, L. G. Jiao, A. Liu, H. E. Montgomery, and Y. K. Ho

Hyperpolarizabilities of hydrogenlike atoms in Debye and dense quantum plasmas

Physical Review E **107**, 045201 (2023)

10.1103/PhysRevE.107.045201

C. Aleshire, T. Eichner, A. Steinkopff, A. Klenke, C. Jauregui, G. Palmer, S. Kühn, J. Nold, N. Haarlammert, W. P. Leemans, T. Schreiber, A. R. Maier, and J. Limpert

Frequency-doubled Q-switched 4 × 4 multicore fiber laser system

Optics Letters **48**, 2198 (2023)

10.1364/OL.487334

A. Schoenberg, H. S. Salman, A. Tajalli, S. Kumar, I. Hartl, and C. M. Heyl

Below-threshold harmonic generation in gas-jets for Th-229 nuclear spectroscopy

Optics Express **31**, 12880 (2023)

10.1364/OE.486338

K. Makur, B. Ramakrishna, S. Krishnamurthy, K. F. Kakolee, S. Kar, M. Cerchez, R. Prasad, K. Markey, M. N. Quinn, X. H. Yuan, J. S. Green, R. H. H. Scott, P. McKenna, J. Osterholz, O. Willi, P. A. Norreys, M. Borghesi, and M. Zepf

Probing bulk electron temperature via x-ray emission in a solid density plasma

Plasma Physics And Controlled Fusion **65**, 045005 (2023)

10.1088/1361-6587/acb79c

L. Silletti, A. Wahid, E. Escoto, P. Balla, S. Rajhans, K. Horn, L. Winkelmann, V. Wanie, A. Trabattoni, C. M. Heyl, and F. Calegari

Dispersion-engineered multi-pass cell for single-stage post-compression of an Ytterbium laser

Optics Letters **48**, 1842 (2023)

10.1364/OL.476846

Y. Zobus, C. Brabetz, J. Hornung, J. B. Ohland, D. Reemts, J.-P. Zou, M. Loeser, D. Albach, U. Schramm, and V. Bagnoud

Millijoule ultrafast optical parametric amplification as replacement for high-gain regenerative amplifiers

High Power Laser Science And Engineering **11**, e48 (2023)

10.1017/hpl.2023.30

J. Machado, N. Paul, G. Soum-Sidikov, L. Duval, S. Mace, R. Löttsch, M. Trassinelli, and P. Indelicato

Absolute measurement of the relativistic magnetic dipole transition in He-like sulfur

Physical Review A **107**, 032821 (2023)

10.1103/PhysRevA.107.032821

B. Yang, Z. Wu, D. Yu, C. Shao, Y. Xue, W. Wang, Z. Song, M. Zhang, J. Liu, R. Lu, Y. Wu, F. Ruan, Y. Zhang, S. Fritzsche, and X. Cai

Nearly isotropic Lyman- α_1 radiation $2p_{3/2} \rightarrow 1s_{1/2}$ following nonradiative electron capture in $\text{Xe}^{54+} + \text{Kr}$ collisions at 197 MeV u^{-1}

Journal Of Physics B-Atomic Molecular And Optical Physics **56**, 055203 (2023)

10.1088/1361-6455/acb58f

S. Kholaf, C. Jauregui, Y. Tu, and J. Limpert

Characterization of transverse mode instability with a 4-quadrant photodiode

Optics Express **31**, 10633 (2023)

10.1364/OE.478961

S. Fritzsche, A. V. Maiorova, and Z. Wu

Radiative Recombination Plasma Rate Coefficients for Multiply Charged Ions

Atoms **11**, 50 (2023)

10.3390/atoms11030050

M. Karst, P. Pfaller, R. Klas, Z. Wang, P. Gierschke, J. Rothhardt, and J. Limpert

22-W average power high pulse energy multipass-cell-based post-compression in the green spectral range

Optics Letters **48**, 1300 (2023)

10.1364/OL.482600

S. Kosugi, F. Koike, M. Iizawa, F. Hosseini, J. Martins, T. Marchenko, O. Travnikova, J. D. Bozek, K. Ito, S. Fritzsche, M. N. Piancastelli, M. Simon, and Y. Azuma

Strong configuration-interaction contributions to the angle-resolved 4p photoelectron spectra of atomic xenon

Physical Review A **107**, 022814 (2023)

10.1103/PhysRevA.107.022814

A. Fedotov, A. Ilderton, F. Karbstein, B. King, D. Seipt, H. Taya, and G. Torgrimsson

Advances in QED with intense background fields

Physics Reports **1010**, 1 (2023)

10.1016/j.physrep.2023.01.003

H. Gies and A. S. Salek

Asymptotically safe Hilbert-Palatini gravity in an on-shell reduction scheme

European Physical Journal C **83**, 173 (2023)

10.1140/epjc/s10052-023-11324-1

C. Zepter, A. Seidel, M. Zepf, M. C. Kaluza, and A. Saevart

Role of spatiotemporal couplings in stimulated Raman side scattering

Physical Review Research **5**, L012023 (2023)

10.1103/PhysRevResearch.5.L012023

M. Du, X. Liu, A. Pelekanidis, F. Zhang, L. Loetgering, P. Konold, C. L. Porter, P. Smorenburg, K. S. E. Eikema, and S. Witte

High-resolution wavefront sensing and aberration analysis of multi-spectral extreme ultraviolet beams

Optica **10**, 255 (2023)

10.1364/OPTICA.478346

H. N. Gopalakrishna, R. Baruah, C. Huenecke, V. Korolev, M. Thuemmler, A. Croy, M. Richter, F. Yahyaei, R. Hollinger, V. Shumakova, I. Uschmann, H. Marschner, M. Zuerch, C. Reichardt, A. Undisz, J. Dellith, A. Pugzlys, A. Baltuska, C. Spielmann, U. Peschel, S. Graefe, M. Waechtler, and D. Kartashov

Tracing spatial confinement in semiconductor quantum dots by high-order harmonic generation

Physical Review Research **5**, 013128 (2023)

10.1103/PhysRevResearch.5.013128

B. Böning and S. Fritzsche

Partial-wave representation of the strong-field approximation. II. Coulomb asymmetry in the photoelectron angular distribution of many-electron atoms

Physical Review A **107**, 023108 (2023)

10.1103/PhysRevA.107.023108

A.-L. Viotti, C. Li, G. Arisholm, L. Winkelmann, I. Hartl, C. M. Heyl, and M. Seidel

Few-cycle pulse generation by double-stage hybrid multi-pass multi-plate nonlinear pulse compression

Optics Letters **48**, 984 (2023)

10.1364/OL.478790

M. Benner, M. Karst, C. A. Mendez, H. Stark, and J. Limpert

Concept of enhanced frequency chirping for multi-pass cells to improve the pulse contrast

Journal Of The Optical Society Of America B-optical Physics **40**, 301 (2023)

10.1364/JOSAB.479037

B. Hidding, R. Assmann, M. Bussmann, D. Campbell, Y.-Y. Chang, S. Corde, J. C. Cabadag, A. Debus, A. Doepp, M. Gilljohann, J. Goetzfried, F. M. Foerster, F. Haberstroh, F. Habib, T. Heinemann, D. Hollatz, A. Irman, M. Kaluza, S. Karsch, O. Kononenko, A. Knetsch, T. Kurz, S. Kuschel, A. Koehler, A. M. de la Ossa, A. Nutter, R. Pausch, G. Raj, U. Schramm, S. Schoebel, A. Seidel, K. Steiniger, P. Ufer, M. Yeung, O. Zarini, and M. Zepf

Progress in Hybrid Plasma Wakefield Acceleration

Photonics **10**, 99 (2023)

10.3390/photonics10020099

F. M. Kröger, G. Weber, S. Allgeier, Z. Andelkovic, S. Bernitt, A. Borovik Jr, L. Duval, A. Fleischmann, O. Forstner, M. Friedrich, J. Glorius, A. Gumberidze, C. Hahn, F. Herfurth, D. Hengstler, M. O. Herdrich, P.-M. Hillenbrand, A. Kalinin, M. Kiffer, M. Kubullek, P. Kuntz, M. Lestinsky, B. Loeher, E. B. Menz, T. Over, N. Petridis, P. Pfäfflein, S. Ringleb, R. S. Sidhu, U. Spillmann, S. Trotsenko, A. Warczak, B. Zhu, C. Enss, and Th. Stöhlker

Towards an Intrinsic Doppler Correction for X-ray Spectroscopy of Stored Ions at CRYRING@ESR

Atoms **11**, 22 (2023)

10.3390/atoms11020022

K. Ueberholz, L. Bozyk, M. Bussmann, N. Eizenhoefer, V. Hannen, M. Horst, D. Kiefer, N. Kiefer, S. Klammes, T. Kühl, B. Langfeld, M. Loeser, X. Ma, W. Noertershaeuser, R. Sánchez, U. Schramm, M. Siebold, P. Spiller, M. Steck, Th. Stöhlker, T. Walther, H. Wang, C. Weinheimer, W. Wen, and D. Winters

XUV Fluorescence Detection of Laser-Cooled Stored Relativistic Ions

Atoms **11**, 39 (2023)

10.3390/atoms11020039

G. Yang, V. S. de Oliveira, D. Laumer, C. M. Heyl, A. Yachmenev, I. Hartl, and J. Kuepper
Self-broadening and self-shift in the $3\nu_2$ band of ammonia from mid-infrared-frequency-comb spectroscopy

Journal Of Molecular Spectroscopy **392**, 111744 (2023)

10.1016/j.jms.2023.111744

Y. Zobus, C. Brabetz, M. Loeser, D. Albach, M. Siebold, and V. Bagnoud

Versatile, compact chirped pulse amplifier pump system for ultrafast optical parametric amplifiers

Optics Express **31**, 5002 (2023)

10.1364/OE.477610

C. Liu, W. Eschen, L. Loetgering, D. P. S. Molina, R. Klas, A. Iliou, M. Steinert, S. Herkersdorf, A. Kirsche, T. Pertsch, F. Hillmann, J. Limpert, and J. Rothhardt

Visualizing the ultra-structure of microorganisms using table-top extreme ultraviolet imaging

Photonix **4**, 6 (2023)

10.1186/s43074-023-00084-6

E. Kueny, A.-L. Calendron, S. Velten, L. Bocklage, F. X. Kaertner, and R. Röhlberger

Spin-structured multilayer THz emitters by oblique incidence deposition

Journal Of Applied Physics **133**, 033903 (2023)

10.1063/5.0128437

A. Kirsche, M. Gebhardt, R. Klas, L. Eisenbach, W. Eschen, J. Buldt, H. Stark, J. Rothhardt, and J. Limpert

Continuously tunable high photon flux high harmonic source

Optics Express **31**, 2744 (2023)

10.1364/OE.474668

W. Middents, G. Weber, A. Gumberidze, C. Hahn, T. Krings, N. Kurz, P. Pfäfflein, N. Schell, U. Spillmann, S. Strnat, M. Vockert, A. Volotka, A. Surzhykov, and Th. Stöhlker

Angle-differential cross sections for Rayleigh scattering of highly linearly polarized hard x rays on Au atoms

Physical Review A **107**, 012805 (2023)

10.1103/PhysRevA.107.012805

M. O. Herdrich, D. Hengstler, A. Fleischmann, C. Enss, A. Gumberidze, P.-M. Hillenbrand, P. Indelicato, S. Fritzsche, and Th. Stöhlker

X-ray Spectroscopy Based on Micro-Calorimeters at Internal Targets of Storage Rings

Atoms **11**, 13 (2023)

10.3390/atoms11010013

B. Minneker, R. Klas, J. Rothhardt, and S. Fritzsche

Critical Laser Intensity of Phase-Matched High-Order Harmonic Generation in Noble Gases

Photonics **10**, 24 (2023)

10.3390/photonics10010024

P. Pfäfflein, G. Weber, S. Allgeier, S. Bernitt, A. Fleischmann, M. Friedrich, C. Hahn, D. Hengstler, M. O. Herdrich, A. Kalinin, F. M. Kröger, P. Kuntz, M. Lestinsky, B. Loehner, E. B. Menz, U. Spillmann, B. Zhu, C. Enss, and Th. Stöhlker

Exploitation of the Timing Capabilities of Metallic Magnetic Calorimeters for a Coincidence Measurement Scheme

Atoms **11**, 5 (2023)

10.3390/atoms11010005

B. Zhu and Th. Stöhlker

Radiative Recombination Studies for Bare Lead Ions Interacting with Low-Energy Electrons

Atoms **11**, 2 (2023)

10.3390/atoms11010002

P. Jagodzinski, D. Banaś, M. Pajek, A. Kubala-Kukuś, Ł. Jabłoński, I. Stabrawa, K. Szary, D. Sobota, A. Warczak, A. Gumberidze, H. F. Beyer, M. Lestinsky, G. Weber, Th. Stöhlker, and M. Trassinelli

A high-resolution asymmetric von Hamos spectrometer for low-energy X-ray spectroscopy at the CRYRING@ESR electron cooler

Journal of Instrumentation **18**, P11002 (2023)

10.1088/1748-0221/18/11/P11002

J. Reinhard, S. Kaleta, J. J. Abel, F. Wiesner, M. Wünsche, E. Seemann, M. Westermann, T. Weber, J. Nathanael, A. Iliou, H. Fiedorowicz, F. Hillmann, C. Eggeling, G. G. Paulus, and S. Fuchs

Laboratory-Based Correlative Soft X-ray and Fluorescence Microscopy in an Integrated Setup

Microscopy and microanalysis **29**, 2014 (2023)

10.1093/micmic/ozad123

C. Sundqvist and F. Karbstein

Two-beam laser photon merging

Physical Review D **108**, 056028 (2023)

10.1103/PhysRevD.108.056028

P. Balla, H. Tuennermann, S. Salman, M. Fan, S. Ališauskas, I. and Hartl, and C. Heyl

Ultrafast serrodyne optical frequency translator

Nature Photonics **17**, 187 (2023)

10.1038/s41566-022-01121-9

R. Schuch and Th. Stöhlker

SPARC at FAIR: New Opportunities for Atomic Physics with Highly Charged Ions

Nuclear Physics News **33**, 27 (2023)

10.1080/10619127.2023.2231801

C. G. Bruno, J. J. Marsh, T. Davinson, P. J. Woods, P. Black, A. Bräuning-Demian, J. Glorius, A. Grant, O. Hall, A. Headspith, P. Hindley, I. Lazarus, K. Middleman, N. Petridis, M. Lestinsky, Yu. A. Litvinov, R. S. Sidhu, and Th. Stöhlker

CARME – The CRYRING Array for Reaction MEasurements

Nuclear Instruments & Methods In Physics Research Section A-Accelerators, Spectrometers, Detectors and Associated Equipment **1048**, 168007 (2023)

10.1016/j.nima.2022.168007

B. Zhu and Th. Stöhlker

Calculation of Radiative Recombination Rates for Hydrogen-Like Ions at High-Z

Proceedings of Science FAIRness2022, 065 (2023)

10.22323/1.419.0065

P. Pfäfflein, C. Hahn, M. O. Herdrich, F. M. Kröger, G. Weber, and Th. Stöhlker

Implementation of a constant fraction algorithm for improved time resolution of metallic magnetic calorimeter measurements

Proceedings of Science FAIRness2022, 044 (2023)

10.22323/1.419.0044

THESES

F. Salgado

Design of a single-particle detection system for strong-field QED experiments

Dissertation

Friedrich-Schiller-Universität Jena; Physikalisch-Astronomische Fakultät, (January 2023).

B. Zhu

High resolution for x-ray spectroscopy studies with highly charged heavy ions at the CRYRING@ESR electron cooler

Dissertation

Friedrich-Schiller-Universität Jena; Physikalisch-Astronomische Fakultät, (February 2023).

Y. Zhang

Carrier-envelope phase (CEP)-dependent strong-field ionization at infrared (IR) wavelengths

Dissertation

Friedrich-Schiller-Universität Jena; Physikalisch-Astronomische Fakultät, (February 2023).

T. Over

Probing the Impulse Approximation via Polarization Studies on Inelastically Scattered Hard X-Rays

Masterarbeit

Friedrich-Schiller-Universität Jena; Physikalisch-Astronomische Fakultät, (July 2023).

R. Soguel

On a vacuum state redefinition in QED corrections to energy shifts of heavy highly charged ions

Dissertation

Friedrich-Schiller-Universität Jena; Physikalisch-Astronomische Fakultät, (July 2023).

Björn Minneker

Generation of spatio-temporal structured high-order harmonics

Dissertation

Friedrich-Schiller-Universität Jena; Physikalisch-Astronomische Fakultät, (July 2023).

M. Shi

High-contrast laser-driven monoenergetic proton beams and near-critical density plasma diagnosis

Dissertation

Friedrich-Schiller-Universität Jena; Physikalisch-Astronomische Fakultät, (July 2023).

C. Sundqvist

Signatures of quantum vacuum nonlinearity in two-beam laser collisions

Dissertation

Friedrich-Schiller-Universität Jena; Physikalisch-Astronomische Fakultät, (August 2023).

Darvin Wanisch

Dynamics of quantum information in many-body systems with nonlocal interactions

Dissertation

Friedrich-Schiller-Universität Jena; Physikalisch-Astronomische Fakultät, (September 2023).

Marc Oliver Herdrich

Anwendung kryogener Kalorimeter für hoch aufgelöste Präzisions-Röntgenspektroskopie

Dissertation

Friedrich-Schiller-Universität Jena; Physikalisch-Astronomische Fakultät, (October 2023).

Baghdasar Baghdasaryan

Spatio-spectral engineering of entangled and single photons in parametric down-conversion

Dissertation

Friedrich-Schiller-Universität Jena; Physikalisch-Astronomische Fakultät, (December 2023).

Prannay Balla

Nonlinear optics approach towards precision spectroscopy of highly charged ions and nuclei

Dissertation

Universität Hamburg, (December 2023).